UNIVERSIDAD NACIONAL AUTÓNOMA DE MÉXICO

PROGRAMA DE MAESTRÍA Y DOCTORADO EN INGENIERÍA

CENTRO DE INVESTIGACIÓN EN ENERGÍA

SIMULACIÓN NUMÉRICA DE LA CONVECCIÓN BAJO LA INFLUENCIA DE FUERZAS ELECTROMAGNÉTICAS Y FUERZAS DE ROTACIÓN

TESIS

QUE PARA OBTENER EL GRADO DE

DOCTOR EN INGENIERÍA

ENERGÍA - SISTEMAS ENERGÉTICOS

PRESENTA:

JOSÉ NÚÑEZ GONZÁLEZ

DIRECTOR DE TESIS:

DR. EDUARDO RAMOS MORA

2012

JURADO ASIGNADO

Presidente: Dr. Cuevas García Sergio

Secretario: Dr. Ramos Mora Eduardo

Vocal: Dr. Del Río Portilla Jesús Antonio

1er. Suplente: Dr. De la Cruz Salas Luis Miguel

2do. Suplente: Dr. Juarez Valencia Lorenzo Héctor

Lugar donde se realizó la tesis:

CENTRO DE INVESTIGACIÓN EN ENERGÍA

TUTOR DE TESIS:

Dr. Eduardo Ramos Mora

FIRMA

AGRADECIMIENTOS

A mis amigos del CIE, en especial a: Michel, Alberto y Saul por tantas cosas que he aprendido de ellos.

A la Universidad Nacional Autónoma de México y en especial al Centro de Investigación en Energía por ser mi casa de estudios.

A CONACyT (Consejo Nacional de Ciencia y Tecnología), por brindarme el financiamiento económico para realizar mis estudios de doctorado. Al proyecto de Conacyt "Flujos magnetohidrodinámicos en campos magnéticos inhomogéneos" Proyecto 131399.

A la Dra. Isabel Mercader Calvillo y al Dr. Juan Lopez dos investigadores destacados que tuve la oportunidad de conocer y aprender de ellos lo que llevo a una aportacion muy valiosa para mis estudios.

Al Dr. Sergio Cuevas Garcia uno de los principales guias de mi formacion.

En especial al Dr. Eduardo Ramos Mora por todo su apoyo, tiempo y consejos que no olvidare.

DEDICATORIA

A mi esposa Marbella y a mi hija Liliana Geraldine.

A mis padres Mario y Gregoria.

A mis hermanos, Leonel, Elizabeth y Ever.

Contents

Resumen

El presente trabajo es un estudio numrico de la conveccin natural en contenedores cilndricos esbeltos. Se estudia el caso cuando la flotacin es la nica fuerza de cuerpo que afecta el movimiento del fluido y cuando fuerzas de rotacin o fuerzas electromagnticas modifican el comportamiento del flujo, generando una gran variacin en las inestabilidades hidrodinmicas del flujo.

El propsito de esta tesis es desarrollar modelos computacionales para profundizar en el conocimiento de flujos convectivos. Este estudio se realiza mediante la solucin numrica de las ecuaciones de balance de masa cantidad de movimiento y energa en coordenadas cilndricas. Se emplearon las tcnicas de volumen finito y mtodos espectrales para la modelacin computacional de la conveccin en un contenedor cilndrico lleno de agua. Se valid los resultados numricos con observaciones experimentales reportadas en la literatura, lo que permiti que se tuviera una mayor certeza del resto de la informacin del flujo obtenida por la solucion numerica y que no fue accesible de manera experimental.

Se propuso una formulacin hbrida para resolver las ecuaciones gobernantes de la conveccin en coordenadas cilndricas. Se utiliza el mtodo de Fourier Galerkin en la direccin azimutal y el mtodo de volumen finito para la direccin radial y axial. Un metodo de correccin de la presin para el desacople de la ecuaciones de Navier-Stokes tambien fue propuesto.

Adicionalmente se explora el efecto de fuerzas electromagnticas y fuerzas de rotacin utilizando estas herramientas numricas desarrolladas.

Abstract

This work is a numerical study of natural convection in slender cylinders. We study the case when buoyancy is the only body force affecting the fluid motion and when rotational forces or electromagnetic forces change the flow behavior, generating a large variation in the hydrodynamic instabilities of the flow.

The purpose of this thesis is to develop computational models to deepen the knowledge of convective flows. This is done by numerical solution of the mass balance equations of momentum and energy in cylindrical coordinates. The techniques of finite volume and spectral methods for computational modeling of convection in a cylindrical container filled with water were used. Numerical results were validated with experimental observations reported in the literature, which had allowed certainty of the rest of the information of flow obtained by the numerical which was not accessible experimentally.

A hybrid formulation was proposed to solve the governing equations of convection in cylindrical coordinates, using the Fourier method Galerkin in the azimuth direction and finite volume method for radial and axial direction, also a pressure correction method for Navier-Stokes equations the decoupling was proposed.

Additionally, we explore the effect of electromagnetic forces and rotational forces developed using these numerical tools.

Introduction

Natural convection is the motion of a fluid generated by density gradients in presence of a volumetric force. The density gradient can be caused by inhomogeneous concentrations of a solute or by non uniform temperature fields. Examples of volumetric forces are the gravitational, centrifugal, Coriolis or Lorentz forces or combinations of them. Natural convection is the continuum counterpart of the Archimedes force. Pioneering observations on the natural convection of extended shallow layers of a thick oil heated from below were made by Benard in 1900 and revealed a rich dynamical behavior that included convective cells with clearly defined spatial patterns, stability exchange between different patterns, bifurcations, and steady and time-dependent flows. Lord Rayleigh devised a theoretical model considering that the fluid layer is unbounded in the horizontal directions and and confined between two horizontal planes separated a distance h. He also introduced a fundamental non-dimensional parameter that describes the qualitative behavior of the flow and has since been called the Rayleigh number. Its formal definition is

$$Ra = \frac{\rho g \beta \Delta T h^3}{\alpha \nu}, \tag{1}$$

where ρ, g, and β are respectively the density, acceleration of gravity and the volumetric expansion coefficient. The characteristic temperature difference is ΔT. One of the main conclusions of the analysis is the determination of a critical Rayleigh number equal to 1708 below which no motion occurs in the fluid layer. Lord Rayleigh's study has been profusely expanded, generalized and specialized by numerous studies in the almost 100 years since it was originally published. A comprehensive summary of the work on the subject up 1993 has been presented by Koschmieder (1993) [1]. The influence of the lateral walls of the fluid container on the stability of the flow was incorporated in the analysis after reliable numerical solutions to the stability equations were available. It is interesting to observe that the Rayleigh number does not include a characteristic horizontal length, and also that this geometrical feature is incorporated into the problem via the boundary conditions. As expected, the effect of the lateral walls is to stabilize the flow and the critical Rayleigh number is larger for more slender containers where the influence of the lateral walls is larger. See Catton and Buell ([2]). Also, accurate algorithms for the numerical integration of the full conservation equations have been proposed and nonlinear analyses are now available.

The study of natural convection in cylindrical geometries is important for many problems present in industry like for instance, flow in heat exchangers, nuclear reactor cooling, mixers and crystal growth processes. It is this last application that we mostly have in mind in the present investigation. It has been noted that the quality of optical and electronic properties of semiconductor crystals grown with the Czochralski or Bridgman methods depend strongly on the compositional homogeneity which in turn is dictated by the dynamics of the molten materials from which the crystal is obtained. For this reason, understanding the transport properties of the natural convective flows is of paramount importance for the semiconductor industry. In this same context, it is known that the presence of other body forces during the crystallization process can change the qualitative properties of the natural convective flow of the molten material and this can be used to control the convective flow dynamics. Studies on the effects of the Coriolis force when the solidification process takes place in a rotating frame of reference or Lorentz force due to the presence of electromagnetic effects while the crystallization occurs, are available in the literature, but the comprehensive picture of their effect on the quality of the crystals is far from being complete.

The present investigation starts with the statement of the conservation equations for mass, momentum and energy. As is well known, a general analytical solution to this set of equations under the initial and boundary conditions of interest is not known. In this thesis, we use and develop several methodologies for the numerical solution of the conservation equations of fluid dynamics in cylindrical coordinates. These include finite volume methods and Fourier- Galerkin methods with Chebyshev polynomials: We proposed a hybrid approach involving both of these techniques. Each methodology has advantages and disadvantages from the points of view of the accuracy of the solution and the computational effort. For this reason, one or more methods can be identified as the most appropriate for specific applications.

The flow patterns and instabilities of the flow are described and a detailed validation of the numerical solution with experimental observations tailor made for the purpose by a member of our group (Miguel Lopez), is also presented [3]. Since experimental observations are in general limited due to technical reasons, the numerical solutions we can be extremely useful to fill in the gaps of information and define a much more complete picture of the physical phenomenon. Indeed, numerical simulations and experimental observations, constitute complementary tools that validate each other and give certitude to the results.

Chapter I of this thesis is a description and a literature's review of the equations of fluid mechanics. The assumptions for modeling natural convection are mentioned.

From chapter II to IV is the description of the methodologies to solve the equations of fluid dynamics in cylindrical coordinates.

Chapter II describes the algorithm of the finite volume method. This method produces low-order solutions but is characterized by its simplicity of implementation and that can easily handle problems with discontinuities in the boundary conditions of the system. For this reason the finite volume method is widely applied in this work.

In chapter III we describe the spectral methods for solving the governing equations of fluid dynamics. Spectral methods are techniques that provide very accurate solutions.

For problems in cylindrical coordinates the Fourier spectral Galerkin method is the best methodology that guarantees the periodicity of the solution.

Based on the experience gained working with finite volume methods and spectral methods, in Chapter IV we present a proposed hybrid methodology with Fourier Galerkin and finite volume method for the solution of the equations of fluid dynamics in cylindrical coordinates. We used Fourier Galerkin in the azimuthal direction and finite volume for the radial an axial directions.

In chapter V we present the study of natural convection in a cylindrical container heated from below and cooled from above. All the numerical tools developed and described in Chapters II-IV were very useful to made this analysis.

In chapter VI we present the study of other configurations of interest for the natural convection problem. The effect of a rotational force or a magnetic field in the case of electrically conductive fluid is considered.

Chapter 1

Governing equations for natural convection

Convection in general means fluid motions caused by temperatures differences with the temperature gradient pointing in any direction.

In natural convection, fluid surrounding a heat source receives heat, becomes less dense and rises. The surrounding, cooler fluid then moves to replace it. This cooler fluid is then heated and the process continues, forming a convection current; this process transfers heat energy from the bottom of the convection cell to top.

The driving force for natural convection is buoyancy, a result of differences in fluid density. Because of this, the presence of gravity or an equivalent force (such as acceleration, centrifugal force or Coriolis force) is essential for natural convection.

To study natural convection should be need it a little review of heat transfer and fluid mechanics as the theory of convection rests on both these subjects.

The equations which describes the motion of a Newtonian fluid are, the continuity equation, the Navier-Stokes equations, the energy equation, and some equations of state. For purpose of summary the governing equations of natural convection will be presented here, they could be found in many books [4], [5].

1.1 The fluid dynamics equations

Consider a fluid in which the density ρ is a function of position $\vec{r} = (x_k)$, $k = 1, 2, 3$. Let u_k $(k = 1, 2, 3)$ the components of the fluid velocity $\vec{u}$ and p, T are the pressure and the temperature of the fluid respectively. The equations governing these variables are the principles of mass, momentum, and energy conservation. In writing the conservation equations, we shall use the notation of cartesian tensors with the usual summation convention and the vector operator notation.

1.1.1 Conservation of mass

The equation expressing conservation of mass is

$$\frac{\partial \rho}{\partial t} + \frac{\partial}{\partial x_k}(\rho u_k) = 0 \tag{1.1}$$

Equation (1.1) is usually called the continuity equation.

In many practical cases of fluid flows, the variation of the density of the fluid may be ignored, in such cases the fluid is said to be incompressible. For an incompressible fluid the equation of continuity reduces to

$$\frac{\partial u_k}{\partial x_k} = 0 \tag{1.2}$$

using vector operator notation, conservation of mass rewrites as follows

$$\nabla \cdot \vec{u} = 0 \tag{1.3}$$

1.1.2 Conservation of momentum

We can write the conservation of momentum equations as follows

$$\rho\frac{\partial u_j}{\partial t} + \rho u_k \frac{\partial u_j}{\partial x_k} = -\frac{\partial p}{\partial x_j} + \frac{\partial}{\partial x_j}\left(\lambda\frac{\partial u_k}{\partial x_k}\right) + \frac{\partial}{\partial x_i}\left[\mu\left(\frac{\partial u_i}{\partial x_j} + \frac{\partial u_j}{\partial x_i}\right)\right] + \rho f_j \tag{1.4}$$

where μ, λ are the coefficient of viscosity and the second coefficient of viscosity respectively, f_j is the jth component of whatever external force may be acting on the fluid.

For an incompressible fluid in which μ is constant, equation (1.4) simplifies to

$$\rho\frac{\partial u_j}{\partial t} + \rho u_k \frac{\partial u_j}{\partial x_k} = -\frac{\partial p}{\partial x_j} + \mu\frac{\partial}{\partial x_k}\left(\frac{\partial u_j}{\partial x_k}\right) + \rho f_j \tag{1.5}$$

in vector operator notation

$$\rho\left(\frac{\partial \vec{u}}{\partial t} + (\vec{u}\cdot\nabla)\,\vec{u}\right) = -\nabla p + \mu\nabla^2\vec{u} + \rho\vec{F} \tag{1.6}$$

Equations 1.6 are called the Navier-Stokes equations.

1.1.3 Conservation of energy

The equation which expresses the conservation of energy is

$$\rho\frac{\partial e}{\partial t} + \rho u_k\frac{\partial e}{\partial x_k} = -p\frac{\partial u_k}{\partial x_k} + \frac{\partial}{\partial x_j}\left(k\frac{\partial T}{\partial x_j}\right) + \lambda\left(\frac{\partial u_k}{\partial x_k}\right)^2 + \mu\left(\frac{\partial u_i}{\partial x_j} + \frac{\partial u_j}{\partial x_i}\right)\frac{\partial u_j}{\partial x_i} \tag{1.7}$$

using the equation of state

$$e = e(\rho, T) = c_V T$$

making use of the equation of continuity, neglecting dissipations terms, for an incompressible fluid, we can simplify the foregoing equation to the form

$$\rho\frac{\partial}{\partial t}(c_V T) + \rho u_k\frac{\partial}{\partial x_k}(c_V T) = \frac{\partial}{\partial x_j}\left(k\frac{\partial T}{\partial x_j}\right) \tag{1.8}$$

or

$$\frac{\partial T}{\partial t} + (\vec{u}\cdot\nabla)\,T = \alpha\nabla^2 T \tag{1.9}$$

for a constant coefficients k, ρ, c_V, where $\alpha = k/(\rho c_V)$.

1.2 The Boussinesq approximation

Equations (1.1),(1.4) and (1.7) are the basic hydrodynamic equations to describes the fluid motion of a compressible fluid. For natural convection density variations provides the driving mechanism of the convective motions, therefore should be solved as compressible problem.

However for many fluid flows the density variations is important only in the body force term of conservation of momentum equations. In all other places in which the density appears in the governing equations,the variations of density leads to an insignificant effect.

The Boussinesq approximation consist in neglecting any variation the variation with the temperature of the material properties of the fluid such as the kinematic viscosity, the thermal diffusivity, and the volume expansion coefficient. This may be considered to be reasonable where relatively small density difference exist over moderate distances. The density is also considered constant except in the body force term of the Navier-Stokes equations. The later term is the prime importance since it represents the force which causes the motion. The variation in density is neglected in the continuity equation as well as in the energy equation.

In the frame of Boussinesq approximation the fluid is treated as incompressible. The equations governing the flow of an incompressible fluid are 1.3,1.6. If gravity provides the only significant body force the Navier-Stokes equations are

$$\frac{\partial \vec{u}}{\partial t} + (\vec{u} \cdot \nabla)\,\vec{u} = -\nabla p/\rho_0 + \nu \nabla^2 \vec{u} + (1 + \frac{\delta\rho}{\rho_0})\vec{g} \tag{1.10}$$

we take $\vec{g} = -g\hat{e}_z$, here $\hat{e}_z$ is the unit vector acting in the positive z direction, and its assumed that the gravity acts in the negative z direction.

In thermal convection the density variation is caused by a temperature variations in the fluid. The density is usually expressed in terms of the temperature by the following relationship

$$\delta\rho = -\beta(T - T_0) \tag{1.11}$$

β is the coefficient of thermal expansion of the fluid, and T_0 is the mean temperature of the fluid which exist at the static equilibrium. Substituting this value

$$\frac{\partial \vec{u}}{\partial t} + (\vec{u} \cdot \nabla)\,\vec{u} = -\nabla p/\rho_0 + \nu \nabla^2 \vec{u} + \beta g(T - T_0)\hat{e}_z \tag{1.12}$$

In order to achieve a closed mathematical system, the energy equation (1.9) must be employed.

1.3 Non dimensional form of the equations for natural convection problems

The governing equations for natural convection are commonly written in dimensionless form, its means that we choose characteristics quantities to scale the system. We can use a characteristic length L , the temperature difference ΔT, the velocity $u_c = \sqrt{g\beta\Delta T L}$ namely the free fall velocity, and a reference time L/u_c. With these scales we defined the dimensionless quantities as follows

$$\vec{x}^* = \frac{\vec{x}}{L}, \qquad t^* = \frac{t}{L/u_c}, \qquad \vec{u}^* = \frac{\vec{u}}{u_c} \tag{1.13}$$

$$p^* = \frac{p}{\rho_0 u_c^2}, \qquad T^* = \frac{T - T_0}{\Delta T} \tag{1.14}$$

The governing equations in dimensionless form is written below

$$\nabla \cdot \vec{u} = 0 \tag{1.15}$$

$$\frac{\partial \vec{u}}{\partial t} + (\vec{u} \cdot \nabla)\,\vec{u} = -\nabla p + \left(\frac{Pr}{Ra}\right)^{\frac{1}{2}} \nabla^2 \vec{u} + T\hat{e}_z \tag{1.16}$$

$$\frac{\partial T}{\partial t} + (\vec{u} \cdot \nabla)\,T = \left(\frac{1}{PrRa}\right)^{\frac{1}{2}} \nabla^2 T. \tag{1.17}$$

The flow is characterized by two dimensionless parameters, the Rayleigh number and the Prandtl number, which is defined as

$$Ra = \frac{g\beta\Delta T L^3}{\nu\alpha}, \quad Pr = \frac{\nu}{\alpha} \tag{1.18}$$

In order to achieve a closed system the boundary conditions must be specified.

Chapter 2

Finite volume method to solve fluid dynamics equations in cylindrical geometries

The finite volume method is a numerical technique that has been used intensively to obtain approximate solutions of partial differential equations. The finite volume method has been described in great detail in many books for instance, [6], [7],[8] and [9].

The basic idea behind the finite volume discretization strategy is as follows: First, divide the domain in a set of non overlapping control volumes, then integrate the incumbent equation on each volume using a linear approximation for the variation of the functions inside the volume. The resulting expression, is the discrete version of the equation which has the form of a linear system of algebraic equations. This system is then solved in a exact or in approximate way, using for example direct or iterative solvers.

In the next section we describe briefly the finite volume method to solve the fluid dynamic equations in cylindrical coordinates.

2.1 General scalar transport equation

A scalar transport equation is a partial differential equation that describes transport phenomena such as heat, mass, momentum transfer, that has the form

$$\frac{\partial \phi}{\partial t} + \nabla \cdot (\vec{u}\phi) = \nabla \cdot (\Gamma \nabla \phi) + S, \tag{2.1}$$

where ϕ is a generalized variable, Γ is a generalized diffusion coefficient. The second term on the left and the first term on the right hand side of the previous equation are the convective and diffusive terms respectively, S is the source term. In cylindrical coordinates, equation [2.1] takes the form

$$\frac{\partial \phi}{\partial t}+\frac{1}{r}\left[\frac{\partial (r u_r \phi)}{\partial r} + \frac{\partial (u_\theta \phi)}{\partial \theta} + \frac{\partial (r u_z \phi)}{\partial z}\right] = \frac{\Gamma}{r}\left[\frac{\partial}{\partial r}\left(r\frac{\partial \phi}{\partial r}\right) + \frac{\partial}{\partial \theta}\left(\frac{1}{r}\frac{\partial \phi}{\partial \theta}\right) + \frac{\partial}{\partial z}\left(r\frac{\partial \phi}{\partial z}\right)\right]+S. \tag{2.2}$$

where u_r, u_θ and u_z are the velocity components.

2.1.1 Governing equations as a transport equations

In this subsection, we give the specialized form of the transport equation for mass, momentum, and energy in cylindrical geometry.

Mass conservation

$$\frac{1}{r}\frac{\partial}{\partial r}(ru_r)+\frac{1}{r}\frac{\partial u_\theta}{\partial \theta}+\frac{\partial u_z}{\partial z}=0. \tag{2.3}$$

Momentum conservation

$$\frac{\partial u_r}{\partial t}+(\vec{u}\cdot\nabla)u_r-\frac{u_\theta^2}{r}=-\frac{\partial p}{\partial r}+\left(\frac{Pr}{Ra}\right)^{\frac{1}{2}}\left(\nabla^2 u_r-\frac{u_r}{r^2}-\frac{2}{r^2}\frac{\partial u_\theta}{\partial \theta}\right)+f_r, \tag{2.4}$$

$$\frac{\partial u_\theta}{\partial t}+(\vec{u}\cdot\nabla)u_\theta+\frac{u_\theta u_r}{r}=-\frac{1}{r}\frac{\partial p}{\partial \theta}+\left(\frac{Pr}{Ra}\right)^{\frac{1}{2}}\left(\nabla^2 u_\theta-\frac{u_\theta}{r^2}+\frac{2}{r^2}\frac{\partial u_r}{\partial \theta}\right)+f_\theta, \tag{2.5}$$

$$\frac{\partial u_z}{\partial t}+(\vec{u}\cdot\nabla)u_z=-\frac{\partial p}{\partial z}+\left(\frac{Pr}{Ra}\right)^{\frac{1}{2}}\nabla^2 u_z+f_z, \tag{2.6}$$

where f_r, f_θ and f_z are the components of the body force term.

Energy conservation

$$\frac{\partial T}{\partial t}+(\vec{u}\cdot\nabla)\,T=\left(\frac{1}{PrRa}\right)^{\frac{1}{2}}\nabla^2 T. \tag{2.7}$$

where

$$\vec{u}\cdot\nabla=u_r\frac{\partial}{\partial r}+\frac{u_\theta}{r}\frac{\partial}{\partial \theta}+u_z\frac{\partial}{\partial z} \tag{2.8}$$

and

$$\nabla^2=\frac{1}{r}\frac{\partial}{\partial r}\left(r\frac{\partial}{\partial r}\right)+\frac{1}{r^2}\frac{\partial^2}{\partial \theta^2}+\frac{\partial^2}{\partial z^2} \tag{2.9}$$

The previous equations can be obtained from the general expression (equation 2.1) using the parameters listed in table 2.1

Equation	ϕ	Γ	S
Mass	1	0	0
r-Momentum	u_r	$\left(\frac{Pr}{Ra}\right)^{\frac{1}{2}}$	$\frac{u_\theta^2}{r}-\frac{\partial p}{\partial r}+\left(\frac{Pr}{Ra}\right)^{\frac{1}{2}}\left(-\frac{u_r}{r^2}-\frac{2}{r^2}\frac{\partial u_\theta}{\partial \theta}\right)+f_r$
θ-Momentum	u_θ	$\left(\frac{Pr}{Ra}\right)^{\frac{1}{2}}$	$-\frac{u_\theta u_r}{r}-\frac{1}{r}\frac{\partial p}{\partial \theta}+\left(\frac{Pr}{Ra}\right)^{\frac{1}{2}}\left(-\frac{u_\theta}{r^2}+\frac{2}{r^2}\frac{\partial u_r}{\partial \theta}\right)+f_z$
z-Momentum	u_z	$\left(\frac{Pr}{Ra}\right)^{\frac{1}{2}}$	$-\frac{\partial p}{\partial z}+f_z$
Energy	T	$\left(\frac{1}{PrRa}\right)^{\frac{1}{2}}$	0

Table 2.1: Parameter definitions to obtain the conservation equations (equations 2.3-2.7) from the general expression (equation 2.1)

2.2 Discrete equations: Integrating over a control volume

The discrete form of the governing equations is obtained by integrating all terms of the general advection-diffusion equation [2.1] over each control volume.

In symbols:

$$\int_V \frac{\partial \phi}{\partial t}\, dV + \oint \vec{u}\phi \cdot \hat{n} dA = \oint \Gamma \nabla \phi \cdot \hat{n} dA + \int_V S_\phi\, dV \tag{2.10}$$

Using the Gauss theorem, the volume integrals in the partial differential equation that contain a divergence term are expressed in terms of surface integrals.

$$\int_V \nabla \cdot \vec{a} dV = \int_A \vec{a} \cdot \hat{n} dA \tag{2.11}$$

Where $\hat{n}$ is the normal outwards to the surface and A is the area enclosing the volume V. Figure 2.1 shows a control volume for a mesh in the (r, θ) plane of cylindrical coordinates. The nomenclature used throughout this document is illustrated in figure 2.1, lowercase letters are used to denote variables evaluated at the boundaries to the volume's contour. Uppercase letters are used to denote variables calculated at the center of the volume.

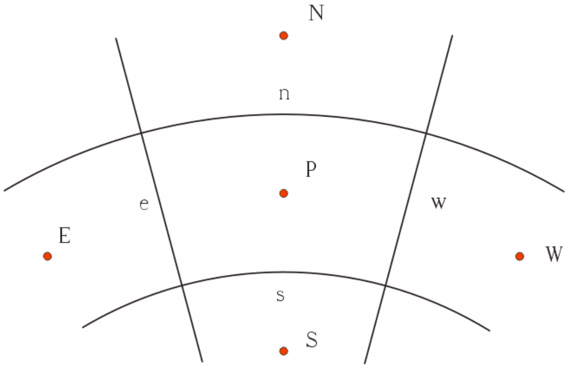

Figure 2.1: Control volume in the (r, θ) plane of cylindrical coordinates

In this study, all integrals are approximate, using the midpoint rule as follows: Convection and diffusion terms are taken implicitly, and the source term explicitly.

Integration of first term of equation [2.10]

$$\int \frac{\partial \phi}{\partial t} dV = (\phi_P - \phi_P^0)\frac{\delta V}{\delta t}. \tag{2.12}$$

The Green's theorem is used to calculate the volume integral in the convective terms as the sum of integrals over the surface of the volume

$$\int \nabla \cdot (\vec{u}\phi) dV = \int (\vec{u}\phi) \cdot \hat{n} dA =$$

$$(u_\theta)_e A_e \phi_e - (u_\theta)_w A_w \phi_w + (u_r)_n A_n \phi_n - (u_r)_s A_s \phi_s + (u_z)_f A_f \phi_f - (u_z)_b A_b \phi_b.$$

the continuity equation is integrated to yield

$$(u_\theta)_e A_e - (u_\theta)_w A_w + (u_r)_n A_n - (u_r)_s A_s + (u_z)_f A_f - (u_z)_b A_b = 0. \tag{2.13}$$

In order to calculate the variables on the volume's surface we use a second order central approximation

$$\phi_e = \frac{\phi_E + \phi_P}{2}, \quad \phi_w = \frac{\phi_W + \phi_P}{2}, \tag{2.14}$$

$$\phi_n = \frac{\phi_N + \phi_P}{2}, \quad \phi_s = \frac{\phi_S + \phi_P}{2}, \tag{2.15}$$

$$\phi_f = \frac{\phi_F + \phi_P}{2}, \quad \phi_b = \frac{\phi_B + \phi_P}{2}. \tag{2.16}$$

The convective terms in the general scalar transport equations need be calculated carefully since they are their nonlinear part in the momentum equations. Other approximations to calculate the convection terms are not discussed here, they are shown in the recommended books of the finite volume method [6], [7],[8] and, [9].

For the diffusive terms

$$\int_V \nabla \cdot (\Gamma \nabla \phi) dV = \int_A (\Gamma \nabla \phi) \cdot \hat{n} dA = \left(\frac{\Gamma}{r} \frac{\partial \phi}{\partial \theta} \right)_e A_e - \left(\frac{\Gamma}{r} \frac{\partial \phi}{\partial \theta} \right)_w A_w + \\ \left(\Gamma \frac{\partial \phi}{\partial r} \right)_n A_n - \left(\Gamma \frac{\partial \phi}{\partial r} \right)_s A_s + \left(\Gamma \frac{\partial \phi}{\partial z} \right)_f A_f - \left(\Gamma \frac{\partial \phi}{\partial z} \right)_b A_b.$$

These terms are calculated with a central differences scheme which is also a second order approximation

$$\left(\frac{\Gamma}{r} \frac{\partial \phi}{\partial \theta} \right)_e = \frac{\Gamma}{r_p} \frac{\phi_E - \phi_P}{\delta \theta}, \quad \left(\frac{\Gamma}{r} \frac{\partial \phi}{\partial \theta} \right)_w = \frac{\Gamma}{r_p} \frac{\phi_P - \phi_W}{\delta \theta}, \tag{2.17}$$

$$\left(\Gamma \frac{\partial \phi}{\partial r} \right)_n = \Gamma \frac{\phi_N - \phi_P}{\delta r}, \quad \left(\Gamma \frac{\partial \phi}{\partial r} \right)_s = \Gamma \frac{\phi_P - \phi_S}{\delta r}, \tag{2.18}$$

$$\left(\Gamma \frac{\partial \phi}{\partial z} \right)_f = \Gamma \frac{\phi_F - \phi_P}{\delta z}, \quad \left(\Gamma \frac{\partial \phi}{\partial r} \right)_b = \Gamma \frac{\phi_P - \phi_B}{\delta z}. \tag{2.19}$$

The volume and its surface are calculated in the following way

$$\delta V = \frac{(r_n^2 - r_s^2)}{2} \delta \theta \delta z = r_p \delta r \delta \theta \delta z; \quad r_p = \frac{(r_n + r_s)}{2}.$$

$$A_n = r_n \delta \theta \delta z; \quad A_s = r_s \delta \theta \delta z; \quad A_e = A_w = \delta r \delta z; \quad A_f = A_b = r_p \delta r \delta \theta.$$

Finally, the source term is

$$\int S_\phi dV = \bar{S}_P \delta V. \tag{2.20}$$

With the approximations described in the previous paragraphs, we have the following discrete version of the general scalar transport equation [2.1]

$$
\begin{aligned}
&(\phi_P - \phi_P^0)\frac{\delta V}{\delta t} + (u_\theta)_e A_e(\frac{\phi_E + \phi_P}{2}) - (u_\theta)_w A_w(\frac{\phi_W + \phi_P}{2}) + (u_r)_n A_n(\frac{\phi_N + \phi_P}{2}) - \qquad (2.21)\\
&(u_r)_s A_s(\frac{\phi_S + \phi_P}{2}) + (u_z)_f A_f(\frac{\phi_F + \phi_P}{2}) - (u_z)_b A_b(\frac{\phi_B + \phi_P}{2}) = \\
&\left(\frac{\Gamma}{r_p}\frac{\phi_E - \phi_P}{\delta\theta}\right) A_e - \left(\frac{\Gamma}{r_p}\frac{\phi_P - \phi_W}{\delta\theta}\right) A_w + \left(\Gamma\frac{\phi_N - \phi_P}{\delta r}\right) A_n - \left(\Gamma\frac{\phi_P - \phi_S}{\delta r}\right) A_s + \\
&\left(\Gamma\frac{\phi_F - \phi_P}{\delta z}\right) A_f - \left(\Gamma\frac{\phi_P - \phi_B}{\delta z}\right) A_b + \bar{S}_P \delta V.
\end{aligned}
$$

This equation can be transformed in to

$$a_P\phi_P = a_N\phi_N + a_S\phi_S + a_W\phi_W + a_E\phi_E + a_F\phi_F + a_B\phi_B + S_P. \tag{2.22}$$

where the a_P's coefficients are

$$a_E = \frac{\Gamma}{r_p}\frac{A_e}{\delta\theta} - \frac{(u_\theta)_e A_e}{2}, \tag{2.23}$$

$$a_W = \frac{\Gamma}{r_p}\frac{A_w}{\delta\theta} + \frac{(u_\theta)_w A_w}{2}, \tag{2.24}$$

$$a_N = \frac{\Gamma A_n}{\delta r} - \frac{(u_r)_n A_n}{2}, \tag{2.25}$$

$$a_S = \frac{\Gamma A_s}{\delta r} + \frac{(u_r)_s A_s}{2}, \tag{2.26}$$

$$a_F = \frac{\Gamma A_f}{\delta z} - \frac{(u_z)_f A_f}{2}, \tag{2.27}$$

$$a_B = \frac{\Gamma A_b}{\delta z} + \frac{(u_z)_b A_b}{2}, \tag{2.28}$$

$$a_P = a_E + a_W + a_N + a_S + a_F + a_B + \frac{\delta V}{\delta t}, \tag{2.29}$$

$$S_P = \phi_P^0\frac{\delta V}{\delta t} + \bar{S}\delta V. \tag{2.30}$$

Note that this system of equations is not complete. In order to close the system, we apply the boundary conditions for the domain. The solution of this linear system of equations is an approximate numerical solution of the partial differential equation.

2.2.1 Boundary conditions

In many problems, the boundary conditions are represented by a given value of ϕ in the boundary; this cases are known as boundary conditions of the first kind or Dirichlet boundary conditions. In other cases, the the normal derivative of ϕ is known in the boundary. These cases are boundary conditions of the second kind or Neumann boundary conditions. For problems in cylindrical coordinates, we have periodic boundary conditions in the angular direction.The required algorithm to specify the boundary conditions is described in the subsequents paragraphs. The origin of the frame of reference needs a similar treatment like a boundary condition.

Dirichlet boundary conditions

Let us consider that ϕ is known on the external radius and denoted by ϕ_b. In the discrete equation for all volumes adjacent to that boundary, the unknown value ϕ_N is interpolated from ϕ_b as

$$\phi_n = \phi_b \approx \frac{\phi_N + \phi_P}{2} \Rightarrow \phi_N = 2\phi_b - \phi_P. \tag{2.31}$$

Substituting in equation 2.22 we have

$$a_P^* \phi_P = a_N^* \phi_N + a_S \phi_S + a_W \phi_W + a_E \phi_E + a_F \phi_F + a_B \phi_B + S_P^*, \tag{2.32}$$

where

$$a_P^* = a_P + a_N; \quad a_N^* = 0; \quad S_P^* = S_P + 2a_N \phi_b \tag{2.33}$$

Neumann boundary condition

In this case the normal derivative ϕ'_b is known at the exterior radius. The value of ϕ_N is interpolated in the following way

$$\phi'_b = \left(\frac{\partial \phi}{\partial r}\right)_n \approx \frac{\phi_N - \phi_P}{\delta r} \Rightarrow \phi_N = \phi_P + \delta r \phi'_b. \tag{2.34}$$

Substituting in equation 2.22 we have

$$a_P^* \phi_P = a_N^* \phi_N + a_S \phi_S + a_W \phi_W + a_E \phi_E + a_F \phi_F + a_B \phi_B + S_P^*, \tag{2.35}$$

where

$$a_P^* = a_P - a_N; \quad a_N^* = 0; \quad S_P^* = S_P + a_N \delta r \phi'_b \tag{2.36}$$

Calculations involving the origin of coordinates

When polar (or cylindrical) coordinates are used, a singularity is introduced at the origin of coordinates. Calculations involving this point must be treated differently from other points to avoid the singularity.

Different treatments have been proposed (see [10] or [11]). In the present study, an artificial boundary condition for the origin is used as shown in the next figure.

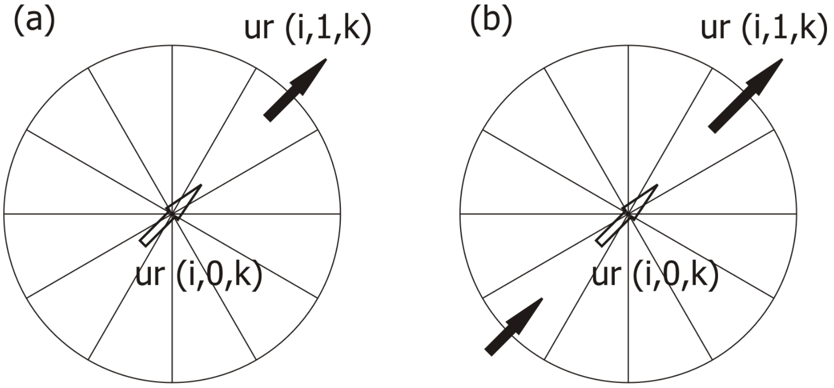

Figure 2.2: Axis treatment in cylindrical coordinates

The firs proposed is applied as follows

$$\phi_{i,0} = \phi_{i,1} \tag{2.37}$$

Where $\phi_{i,0}$ is an artificial boundary value at the origin and $\phi_{i,1}$ sis the value at the first internal radius. It is an explicit boundary condition which is basically a Newman boundary condition at the pole.

The second methodology for the axis treatment is a streamwise average boundary condition

$$\phi_{(i,0)} = (\phi_{(i,1,k)} - \phi_{(i+n_\theta/2,1)})/2 \tag{2.38}$$

2.3 Implementing finite volume method to solve the fluid dynamics equations

Once the discrete version the general scalar transport equation resulting from the finite volume discretization has been obtained, we describe the strategy to solve the coupled fluid dynamics equations.

We apply a pressure correction method to determined the pressure, that is an iterative procedure described as follows: We start with a guess for the pressure, with this pressure the solutions of the Navier-Stokes equations don't satisfied the continuity equation, then we correct the pressure and we correct the velocity iteratively until we have small divergence in each control volume.

There are many decoupling strategies to solve the fluid dynamics equations which are not going to be described here. The SIMPLEC method has the advantages that the pressure correction equation is not to ill conditioned and these iterative procedure guarantees a low divergence convergence rate.

The velocity components u_i of the momentum equations, satisfies special cases of the general scalar transport equation [2.1] if we take the nonlinear terms of the equations in a semi implicit way for each time iteration.

In the fluid dynamics equations the pressure gradient is part of the source term therefore we cannot solve the equations unless the pressure is known. Since there is not an explicit equation for the pressure, the continuity equation should be used to calculate the correct pressure distribution.

It is convenient to use a staggered mesh to avoid unphysical solutions [7]. In a staggered mesh, the velocities are calculated at the surfaces and scalar fields are calculated at the center of the volumes. Figure 2.3 illustrate a staggered mesh in cylindrical coordinates

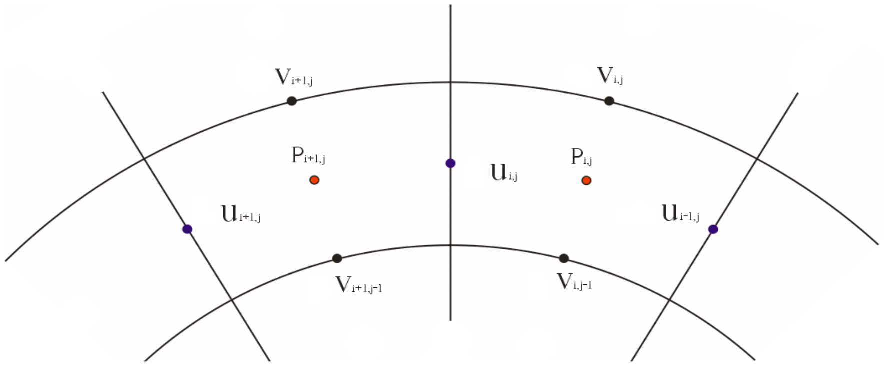

Figure 2.3: Staggered mesh in cylindrical coordinates

2.3.1 Pressure correction methods

The discrete version of the general scalar transport equation resulting from the finite volume[2.22] can be written as

$$a_n u_n = \sum a_{nb} u_{nb} + b + A_n(p_P - p_N), \tag{2.39}$$

where b is all source terms without the pressure gradient, A_n is the area where the pressure force is acting. Coefficients a_{nb} are calculated as described above by taking into account the staggered mesh arrangement. We can write similar equations for each velocity component.

With an initial pressure field guess p^*, we solve the velocity equations. The result is an expression for the velocity field u^*

$$a_n u_n^* = \sum a_{nb} u_{nb}^* + b + A_n(p_P^* - p_N^*). \tag{2.40}$$

In general this solution for the velocity field u^* does not satisfy the continuity equation. In a second step, we correct the guess for the pressure until the resulting velocity field satisfies the continuity equation using the following procedure.

Let p' the pressure correction, corresponding to u^* we defined the correction u', such that

$$p = p^* + p' \quad y \quad u = u^* + u'. \tag{2.41}$$

From 2.39 and 2.40, we get

$$a_n u'_n = \sum a_{nb} u'_{nb} + A_n(p'_P - p'_N). \tag{2.42}$$

Simplifications of the term $\sum a_{nb} u'_{nb}$ defines a series of methods with names having the generic root SIMPLE (Semi Implicit Pressure Linked Equations). This method was originally proposed by Patankar [9].

2.3.2 SIMPLEC method

In these method the equation 2.42 is simplified by subtracting the term $\sum a_{nb} u'_n$, from the two sides of equations 2.39

$$(a_n - \sum a_{nb}) u'_n = \sum a_{nb}(u'_{nb} - u'_n) + A_n(p'_P - p'_N), \tag{2.43}$$

and neglecting the term $\sum a_{nb}(u'_{nb} - u'_n)$

$$u_n = u^* + d_n(p'_P - p'_N), \tag{2.44}$$

where

$$d_n = \frac{A_n}{a_n - \sum a_{nb}}. \tag{2.45}$$

Corresponding equations are written for each velocity component, in the next step we substitute the resulting equations in the continuity equation to obtain the following equation for the pressure correction.

$$a_P p'_P = a_N p'_N + a_S p'_s + a_W p'_W + a_E p'_E + a_F p'_F + a_b p'_B + b_p, \tag{2.46}$$

where

$$a_N = A_n d_n \tag{2.47}$$

$$a_P = a_E + a_W + a_N + a_S + a_F + a_B \tag{2.48}$$

$$b_p = (u^*_\theta)_e A_e - (u^*_\theta)_w A_w + (u^*_r)_n A_n - (u^*_r)_s A_s + (u^*_z)_f A_f - (u^*_z)_b A_b \tag{2.49}$$

Since no correction is necessary for the velocity in the boundary, the pressure correction is zero at the boundary

In summary the SIMPLEC strategy comprises in the following steps

1. Start with a guess for the variables u^*_r, u^*_θ, u^*_z, p^*,T^*
2. Calculate the coefficients for the balance equations
3. Solve the equations for velocity components
4. Calculate coefficients for pressure correction
5. Solve the equations for the pressure correction p'

6. Apply the correction for the pressure $p = p' + p^*$
7. Correct the velocities
8. Solve equations for other variables T^*
9. Repeat until convergence is reached.

CHAPTER 3

Fourier Galerkin with Chebyshev pseudo spectral method to solve fluid dynamics equations in cylindrical geometries

In this chapter we will show the way to implement spectral methods to solve the fluid dynamics equations in cylindrical geometries. First, the basis to implement spectral methods to solve second order differential equations is presented. It includes, the discretized equations and the treatment of boundary conditions using Galerkin and collocation methods. Then, we present a direct method to solve the linear system of equations resulting from Chebyshev collocation method. Finally, we show the procedure to solve the fluid dynamics equations.

3.1 Spectral methods

Spectral methods is the generic name given to numerical techniques to solve differential equations using basis of the function space. The most common formulations used in spectral methods are Galerkin and collocation methods. It can be demonstrated that the convergence of spectral methods is exponential while the convergence of finite difference is only algebraic (see [12]). The idea is to approximate the exact solution of the differential equation as a linear combination of known basis functions.

In spectral methods, the solution of an equation is expressed in terms of trigonometric functions e^{ikx} for periodic problems, and Chebyshev $T_k(x)$ or Legendre $L_k(x)$ polynomials, for non periodic problems. To solve the fluid dynamic equations in cylindrical coordinates we can use, Fourier-Galerkin method in the azimuthal direction, and pseudo spectral Chebyshev collocation method for the axial and radial directions.

Many books show how to apply spectral methods to solve partial differential equations in Cartesian coordinates [13], [14], [12], but the case in cylindrical coordinates has not been profusely.

3.1.1 The method of weighted residuals

Consider a differential equation

$$Lu(x) = f(x) \quad \text{over the interval} \quad a \leq x \leq b, \tag{3.1}$$

with the boundary conditions

$$Bu(x) = g \quad \text{on } x = a \text{ and } x = b. \tag{3.2}$$

Here, L is a second order partial differential operator and B denotes a Dirichlet, Newman or Robin boundary conditions

The weighted residual method uses a finite number of functions $\{\phi_i(x)\}_{i=0}^{N}$ to approximate the solution to equation 3.1 as a truncated series expansion.

A trial solution is defined as follows:

$$u_N\left(x\right) = \sum_{n=0}^{N} \hat{u}_n \phi_n\left(x\right) \tag{3.3}$$

The trial (or basis) functions are assumed to be known, then, only the expansion coefficients must be determined to. The trial functions span is a finite-dimensional subspace of square integrable functions.

Useful sets of basis functions must have the following properties:

1. Easy to compute. For example trigonometric functions and polynomials both certainly satisfy this criterion

2. Rapid convergence. This means that any solution can be represented to arbitrarily high accuracy by taking a sufficiently large truncation N parameter .

3. Completeness. The basis functions must be sufficient to represent all functions in the class we are interested in. A rigorous completeness proof is too complicated to discuss here, Fourier series and Chebyshev polynomials do have the property of completeness.

The goal is to construct $u_N(x)$ such that the residual

$$r(x) = Lu_N(x) - f(x) \tag{3.4}$$

is minimized by the scalar product

$$(w_k(x), r(x)) = \int_a^b w_k(x)(Lu(x) - f(x))dx, \qquad k = 0, 1, ..., N \tag{3.5}$$

for some choices of weight functions $w_k(x)$.

Weighted residuals method is a general theory that describes many types of different numerical methods; the particular choice of the trial and weight functions defines the specific method. Spectral methods are classified according test functions as follows:

- Galerkin-type methods: The test functions are equal to the trial functions, i.e.

$$w_k = \phi_k \qquad . \tag{3.6}$$

- Collocation method: Test functions are Dirac's delta functions at some special points called collocations points

$$w_k = \delta\left(x - x_k\right) \tag{3.7}$$

The collocations points x_k are selected points on (a, b). The choice of such points is not completely arbitrary. There is a set of collocation points that gives an optimal solution methodology.

In the collocation method, the residual is exactly zero at the collocation points whereas in the Galerkin-type method the residual is zero in the mean.

3.2 Approximation of the solution of a differential equation with the Galerkin method

Galerkin methods apply when the trial functions ϕ_k satisfy the boundary conditions associated, i.e.:

$$B_- \phi_k = g_- \text{ at } x = a, \text{and} \qquad B_+ \phi_k = g_+ \text{ at } x = b. \tag{3.8}$$

Then, according to the general formulation expressed in equations (3.1), (3.3) and (3.5), the Galerkin equations are

$$(r, \phi_i) = (Lu_N - f, \phi_i) = 0, \quad i = 0, \ldots, N \tag{3.9}$$

replacing u_N by the series expansion

$$\sum_{k=0}^{N} \hat{u}_k \left(L\phi_k, \phi_i\right) = \left(f, \phi_i\right), \quad i = 0, \ldots, N \tag{3.10}$$

The scalar product $(L\phi_k, \phi_i)$ is evaluated using the properties of the trial functions. In particular, if they are orthogonal functions the following relation holds,

$$(\phi_k, \phi_l) = c_k \delta_{k,l} \tag{3.11}$$

where c_k is some constant and $\delta_{k,l}$ is the Kronecker delta. The scalar product (f, ϕ_i) is equal to $c_i \hat{f}_i$ where $\hat{f}_i$, $i = 0, \ldots, N$, is the expansion coefficient for f.

3.2.1 Fourier Galerkin method in cylindrical coordinates

In this section, we describe some details is to solve partial differential equations in cylindrical coordinates using the Fourier Galerkin method. More complete discussion can be found in references [15], [12], [16], The Fourier Galerkin method is naturally applied in the azimuthal direction since the harmonic functions satisfy periodic boundary conditions, and grants full periodicity of the solution.

As an example to illustrate the method, let us consider a two dimensional Poisson equation in cylindrical coordinates:

$$\frac{\partial^2 \phi}{\partial r^2} + \frac{1}{r}\frac{\partial \phi}{\partial r} + \frac{1}{r^2}\frac{\partial^2 \phi}{\partial \theta^2} = f. \tag{3.12}$$

First, we approximate ϕ as a truncated Fourier expansion in the azimuthal coordinate

$$\phi = \sum_{k=-N/2}^{N/2-1} \hat{\phi}_k(r) e^{ik\theta} \tag{3.13}$$

Substituting in equation (3.12) we obtain

$$\sum_{k=-N/2}^{N/2-1} \left(\frac{\partial^2 \phi_k}{\partial r^2} + \frac{1}{r}\frac{\partial \phi_k}{\partial r} - \frac{k^2}{r^2}\phi_k \right) e^{ik\theta} = f \tag{3.14}$$

Using the Galerkin method and applying the orthogonality condition for the Fourier series, the result is a system of partial differential equations for the expansion coefficients (Fourier modes).

$$\frac{\partial^2 \phi_k}{\partial r^2} + \frac{1}{r}\frac{\partial \phi_k}{\partial r} - \frac{k^2}{r^2}\phi_k = f_k \qquad \text{for } k = -N/2, N/2-1 \tag{3.15}$$

This process can be described as translation of the problem from the physical space to the Fourier space. The resulting equations can be solved using a pseudo spectral collocation method with Chebyshev polynomials [12]. Combining these two method we can solve the Poisson equation in cylindrical coordinates. In the next section, we will describe the Chebyshev collocation method.

The coefficients, f_k are the Fourier coefficients of f and can be found from the orthogonal projection $(f, e^{ik\theta})$ which is the well known Fourier Transform. The Fourier Galerkin method requires the evaluation of integrals to compute the orthogonal projections. This calculation procedure can be combined with the Fast Fourier Transform algorithm to optimize the calculation. An alternative procedure is to represent the function f in terms of grid point values by way of an interpolant. Such approximations are called nodal. Nodal approximations are used to introduce of a rule that we used to find the modal coefficients in the next section.

3.2.2 Discrete Fourier transform

In this section we present a methodology to obtain the Fourier modes of a series expansion of a real function ϕ defined on a discrete set of points (collocation points). First we present some properties of the Fourier modes of the Fourier expansion of a real function.

- In general, Fourier modes are complex, i.e. $\hat{\phi}_k = a_k + ib_k$
- If ϕ is a real function, then the Fourier modes satisfy the following properties:

  $$\hat{\phi}_0 = a_0 \qquad \text{is real,}$$

  $$\hat{\phi}_{-N/2} = a_{-N/2} \qquad \text{is real,}$$

  and for $k = 1, N/2 - 1$

  $$\hat{\phi}_{-k} = a_k - ib_k$$

  .
- If ϕ is real, then the derivative of ϕ is real

  $$\frac{\partial\phi}{\partial\theta} = \sum_{k=-N/2}^{N/2-1} ik\hat{\phi}_k e^{ik\theta}, \tag{3.16}$$

  and the Fourier coefficients for the derivative of ϕ must satisfy the conditions of real Fourier expansion.

Direct forward Fourier transform

The truncated Fourier series expansion of ϕ is:

$$\phi = \sum_{k=-N/2}^{N/2-1} \hat{\phi}_k e^{ik\theta}, \qquad 0 \le \theta \le 2\pi \tag{3.17}$$

where $\hat{\phi}_k = a_k + ib_k$ for all k. ϕ is determined at the N collocations points

$$\theta_j = \frac{2\pi j}{N} \qquad j = 0, ..., N-1. \tag{3.18}$$

Then, for ϕ_j $j = 0, ..., N-1$

$$\phi_j = \sum_{k=-N/2}^{N/2-1} \hat{\phi}_k e^{ik\theta_j}, \tag{3.19}$$

and therefore

$$\phi_j = \sum_{k=1}^{N/2-1} (a_k + ib_k)e^{ik\theta_j} + \sum_{k=1}^{N/2-1} (a_k - ib_k)e^{-ik\theta_j} + a_0 e^{i0} + a_{-N/2}e^{-i\theta_j N/2}. \tag{3.20}$$

Given that ϕ is assumed to be a real function, using the assumptions for a real function Fourier expansion

$$\phi_j = a_0 + \sum_{k=1}^{N/2-1} 2\left[a_k \cos(k\theta_j) - b_k \sin(k\theta_j)\right] + a_{-N/2}\cos(\pi j) \tag{3.21}$$

Equation (3.21) can be interpreted as a matrix multiplication that evaluates ϕ at the collocation points from the Fourier modes.

Inverse Fourier transform

The objective of the inverse Fourier transform is calculate the Fourier modes at the collocation points for $j = 0, ..., N-1$.

$$\hat{\phi}_k = \frac{1}{N}\sum_{j=0}^{N-1} \phi_j e^{-ik\theta_j} \tag{3.22}$$

or

$$\hat{\phi}_k = \frac{1}{N}\sum_{j=0}^{N-1} \phi_j(\cos(k\theta_j) - i\sin(k\theta_j)) \tag{3.23}$$

Specifically

$$\hat{\phi}_0 = \frac{1}{N}\sum_{j=0}^{N-1} \phi_j \tag{3.24}$$

$$\hat{\phi}_k = a_k + ib_k = \frac{1}{N}\sum_{j=0}^{N-1} \phi_j \cos(k\theta_j) + i\frac{1}{N}\sum_{j=0}^{N-1} \phi_j(-\sin(k\theta_j)) \tag{3.25}$$

$$\hat{\phi}_{-N/2} = \frac{1}{N}\sum_{j=0}^{N-1} \phi_j(\cos(N\theta_j/2)) \tag{3.26}$$

Equations 3.24-3.26 is a matrix multiplication to calculate the Fourier modes of ϕ expansion from its values at the collocation points.

3.3 The collocation method

In this section we give a brief summary of the procedure to obtain the solution of a differential equations with Chebyshev collocation spectral method. Different algorithms to compute the derivative matrices are discussed and the treatment for pole conditions at r=0 are also presented.

The collocation equations were obtained by considering a truncated expansion and by making the associated residual $r = Lu_N - f$ equal to zero at the inner collocation points $x_i, i = 1, \ldots, N-1$. The collocation equations are

$$L\left(\sum_{n=0}^{N} \hat{u}_n \phi_n(x_i)\right) = f(x_i), \quad i = 1, \ldots, N-1, \tag{3.27}$$

which constitute a linear system of $N+1$ equations for the $N+1$ coefficients $\hat{u}_k$, $k = 0, \ldots, N$. The system is closed with the boundary conditions

$$B_- u_N(x_0) = g_-, \quad B_+ u_N(x_N) = g_+ \tag{3.28}$$

However, an equivalent formulation is generally preferred. It consist of considering the values $u_N(x_i)$ at the collocation points x_i, $i = 0, \ldots, N$, as unknowns rather than the coefficients $\hat{u}_k$. This is possible since the expansion coefficients $\hat{u}_k$, $k = 0, \ldots, N$, can be expressed in terms of the $u_N(x_i)$, $i = 0, \ldots, N$.

As consequence, we can construct differentiation formulas expressing the derivative, of any order, at a given collocation point in terms of the values of the function itself at all collocation points. The derivatives of the function $u(x)$, in the collocation points $u_N^{(p)}(x_i)$ are calculated in the following manner

$$u_N^{(p)}(x_i) = \sum_{j=0}^{N} d_{i,j}^{(p)} u_N(x_j). \tag{3.29}$$

If $u(x)$ is defined over the interval $-1 \leq x \leq 1$, the Gauss-Lobatto collocation points are calculated by

$$x_j = \cos\left(\frac{j\pi}{N}\right) \tag{3.30}$$

for those collocation points first and second order derivative matrices are the optimum positions since they have analytical expressions [12].

3.3.1 Matrix derivatives

The derivatives of $u(x)$ at the collocation points x_i can be calculated in many different ways. Here we present the most commonly used expressions.

First order derivative

$$\begin{aligned}
d_{i,j}^{(1)} &= \frac{\bar{c}_i}{\bar{c}_j} \frac{(-1)^{i+j}}{x_i - x_j} && 0 \leq i, j \leq N,\ i \neq j \\
d_{i,i}^{(1)} &= -\frac{x_i}{2(1 - x_i^2)}, && 1 \leq i \leq N-1 \\
d_{0,0}^{(1)} &= -d_{N,N}^{(1)} = \frac{2N^2 + 1}{6}
\end{aligned}$$

Second order derivative

$$
\begin{aligned}
d^{(2)}_{i,j} =& \frac{(-1)^{i+j}}{\bar{c}_j}\frac{x_i^2 + x_i x_j - 2}{(1-x_i^2)(x_i-x_j)^2}, && 0 \leq i \leq N-1 \\
& && 0 \leq j \leq N,\ i \neq j \\
d^{(2)}_{i,i} =& -\frac{(N^2-1)(1-x_i^2)+3}{3(1-x_i^2)^2}, && 1 \leq i \leq N-1 \\
d^{(2)}_{0,j} =& \frac{2}{3}\frac{(-1)^j}{\bar{c}_j}\frac{(2N^2+1)(1-x_j)-6}{(1-x_j)^2}, && 1 \leq j \leq N \\
d^{(2)}_{N,j} =& \frac{2}{3}\frac{(-1)^{j+N}}{\bar{c}_j}\frac{(2N^2+1)(1+x_j)-6}{(1+x_j)^2}, && 1 \leq j \leq N \\
d^{(2)}_{0,0} =& d^{(1)}_{N,N} = \frac{N^4-1}{15}
\end{aligned}
$$

When problem is a defined in an arbitrary interval $r_0 \leq x \leq r_1$ we use the following coordinate transformation

$$
r = a + bx, \qquad a = \frac{r_1 + r_0}{2}, \qquad b = \frac{r_1 - r_0}{2} \tag{3.31}
$$

Which maps the function and the differential equation over the interval $-1 \leq x \leq 1$. For cylindrical coordinates in an annular domains we can use the matrix derivatives defined above. Only for a region containing the origin we need a different form of the matrix derivatives which includes a special treatment for the axis of coordinates.

Radial derivative matrix

To calculate the derivative matrix using collocation technique two alternatives have been proposed. In order to avoid coordinate singularities, we do not define the point at $r = 0$ as a collocation point.

Gauss Radau points

The first methodology consist in considering the interval $-1 < x \leq 1$, and use the Gauss Radau points defined by

$$
y_j = \cos\left(\frac{j\pi}{N+1}\right). \tag{3.32}
$$

A matrix derivative, based on those points,can be constructed

$$
dr^{(1)}_{i,j} = \frac{1+y_j}{1+y_i} d^{(1)}_{i,j} - \frac{\delta_{i,j}}{1+y_j}, \tag{3.33}
$$

where $d^{(1)}_{i,j}$ is the first order derivative based on Gauss Lobatto points. It should be noted the if we use N Gauss Radau collocation points,N+1 Gauss Lobatto collocation points must be used.

Odd, Even, derivatives matrices

The second option to calculate a radial derivative matrix is based on the parity of the Fourier modes. Taking $N_x = 2N_r + 1$ collocations points over the interval $[-1, 1]$ we construct $d^{(1)_{i,j}}$, $d^{(2)_{i,j}}$ derivatives and calculate a matrix derivative over the interval $(0, 1]$. Radial derivatives matrices are constructed as follows:

First order derivative

$$dr^{(1)}_{i,j} = d^{(1)}_{i,j} + d^{(1)}_{i,N_x-j}; \qquad 0 \le i \le N_r, \quad 0 \le j \le N_r, \qquad k = even$$

$$dr^{(1)}_{i,j} = d^{(1)}_{i,j} - d^{(1)}_{i,N_x-j}; \qquad 0 \le i \le N_r, \quad 0 \le j \le N_r, \qquad k = odd$$

Second order derivative

$$dr^{(2)}_{i,j} = d^{(2)}_{i,j} + d^{(2)}_{i,N_x-j}; \qquad 0 \le i \le N_r, \quad 0 \le j \le N_r, \qquad k = even$$

$$dr^{(2)}_{i,j} = d^{(2)}_{i,j} - d^{(2)}_{i,N_x-j}; \qquad 0 \le i \le N_r, \quad 0 \le j \le N_r, \qquad k = odd$$

3.3.2 Boundary conditions

The collocation method fort the interior points leads to an algebraic system for the unknowns $u_N(x_i)$, $i = 0, \ldots, N$. The boundary values $u(x_0) = u_0$ and $u(x_N) = u_N$ are given by the boundary conditions. We add the contributions of the information at the boundaries to get a closed the linear system of equations.

Let us consider for example the one dimensional Poisson equation

$$\frac{d^2u}{dx^2} = h, \quad -1 < x < 1 \tag{3.34}$$

Using the collocation method, for the inner collocations points $i = 1, N-1$ we have

$$\sum_{l=0}^{N} d^2_{i,l} u_l = h_i, \tag{3.35}$$

and taking the values at the boundary

$$\sum_{l=1}^{N-1} d^2_{i,l} u_l + d^2_{i,0} u_0 + d^2_{i,n} u_n = h_i, \tag{3.36}$$

the linear system of equations is closed. It means that the form of the linear system of equations present changes dependent on the combination of boundary conditions. It must be remarked that different set of boundary conditions ca be considered, as is described as follows

Dirichlet-Dirichlet boundary conditions

For Dirichlet-Dirichlet boundary conditions, the values of the dependent variables at the boundary are known, and therefore the form of the linear system of equation is

$$\sum_{l=1}^{N-1} \tilde{d}^2_{i,l} u_l = \tilde{h}_i, \tag{3.37}$$

where

$$\tilde{d}^2_{i,l} = d^2_{i,l}, \tag{3.38}$$

and

$$\tilde{h}_i = h_i - d^2_{i,0} u_0 - d^2_{i,n} u_n. \tag{3.39}$$

Dirichlet-Neumann boundary conditions

For Dirichlet-Neumann boundary conditions, one value at the boundary is known and the other can be can calculated from the Newman boundary condition

$$\sum_{l=0}^{N} d^1_{0,l} u_l = g_0. \tag{3.40}$$

Extracting the first and the last term of the sum

$$\sum_{l=1}^{N-1} d^1_{0,l} u_l + d^1_{0,0} u_0 + d^1_{0,n} u_n = g_0 \tag{3.41}$$

u_0 is defined by

$$u_0 = \frac{1}{d^1_{0,0}} g_0 - \frac{1}{d^1_{0,0}} \left(\sum_{l=1}^{N-1} d^1_{0,l} u_l + d^1_{0,n} u_n \right). \tag{3.42}$$

Substituting this expression in equation (3.36), the linear system of equations has the form

$$\sum_{l=1}^{N-1} \tilde{d}^2_{i,l} u_l = \tilde{h}_i \tag{3.43}$$

where

$$\tilde{d}^2_{i,l} = d^2_{i,l} - \frac{d^2_{i,0} d^1_{0,l}}{d^1_{0,0}} \tag{3.44}$$

and

$$\tilde{h}_i = h_i - d^2_{i,n} u_n + \frac{d^2_{i,0} d^1_{0,n} u_n}{d^1_{0,0}} - \frac{d^2_{i,0} g_0}{d^1_{0,0}} \tag{3.45}$$

Neumann-Neumann boundary conditions

For Neumann-Neumann boundary conditions, the values at the boundary can be obtained from Neumann boundary conditions at the initial point

$$\sum_{l=0}^{N} d^1_{0,l} u_l = g_0 \tag{3.46}$$

$$\sum_{l=1}^{N-1} d^1_{0,l} u_l + d^1_{0,0} u_0 + d^1_{0,n} u_n = g_0, \tag{3.47}$$

an at the final point

$$\sum_{l=0}^{N} d^1_{n,l} u_l = g_n \tag{3.48}$$

$$\sum_{l=1}^{N-1} d^1_{n,l} u_l + d^1_{n,0} u_0 + d^1_{n,n} u_n = g_n \tag{3.49}$$

This is a linear system of equations whose solution are

$$u_0 = \frac{d^1_{n,n} g_0 - d^1_{0,n} g_n}{ex} - \frac{d^1_{n,n}}{ex} \sum_{l=1}^{N-1} d^1_{0,l} u_l + \frac{d^1_{0,n}}{ex} \sum_{l=1}^{N-1} d^1_{n,l} u_l \tag{3.50}$$

$$u_n = -\frac{d^1_{n,0} g_0 - d^1_{0,0} g_n}{ex} + \frac{d^1_{n,0}}{ex} \sum_{l=1}^{N-1} d^1_{0,l} u_l - \frac{d^1_{0,0}}{ex} \sum_{l=1}^{N-1} d^1_{n,l} u_l \tag{3.51}$$

where

$$ex = d^1_{0,0} d^1_{n,n} - d^1_{0,n} d^1_{n,0} \tag{3.52}$$

Substituting expressions (3.50) and (3.51) in equation 3.36, the form of the linear system of equations for Neumann-Neumann boundary conditions is

$$\sum_{l=1}^{N-1} \tilde{d}^2_{i,l} u_l = \tilde{h}_i, \tag{3.53}$$

where

$$\tilde{d}^2_{i,l} = d^2_{i,l} + \frac{d^2_{i,0}}{ex}(-d^1_{n,n} d^1_{0,l} + d^1_{0,n} d^1_{n,l}) + \frac{d^2_{i,n}}{ex}(d^1_{n,0} d^1_{0,l} - d^1_{0,0} d^1_{n,l}) \tag{3.54}$$

and

$$\tilde{h}_i = h_i - \frac{d^2_{i,0}}{ex}(d^1_{n,n} g_0 - d^1_{0,n} g_n) - \frac{d^2_{i,n}}{ex}(-d^1_{n,0} g_0 + d^1_{0,0} g_n). \tag{3.55}$$

Boundary conditions in cylindrical geometries

In order to illustrate the treatment of boundary conditions in cylindrical geometries, let us consider the one dimensional Poisson equation in cylindrical coordinates

$$\frac{\partial^2 \phi}{\partial r^2} + \frac{1}{r}\frac{\partial \phi}{\partial r} = f. \tag{3.56}$$

Using collocation method, for the inner collocations points $i = 1, N_r$ we have,

$$\sum_{l=0}^{n_r} (d^2_{i,l} + \frac{d^1_{i,l}}{r_i})\phi_l = f_i. \tag{3.57}$$

Defining

$$dr^2_{i,l} = d^2_{i,l} + \frac{d^1_{i,l}}{r_i}, \tag{3.58}$$

we have a linear system of equations with the following form

$$\sum_{l=0}^{n_r} dr^2_{i,l}\phi_l = f_i. \tag{3.59}$$

Is very important take the contribution of the boundary conditions. For an annular domain the implementation of boundary condition is similar as that described in the last section 3.3.2. When the domain includes the origin we must use matrix derivatives for the the pole. When the origin is part of the domain there is no boundary condition at the pole, the only boundary condition being at the exterior radius. In the notation of the spectral method, the exterior radius is r_0, while the nearest point to origin is r_{N_r}

Dirichlet boundary conditions

For Dirichlet boundary conditions the form of the linear system is(see equation 3.59)

$$\sum_{l=1}^{n_r} dr^2_{i,l}\phi_l = f_i - dr^2_{i,0}\phi_0 \tag{3.60}$$

Neumann boundary condition

For Neumann boundary condition the value at the boundary is calculated in the following manner

$$\sum_{l=0}^{n_r} d^1_{0,l}\phi_l = \sum_{l=1}^{n_r} d^1_{0,l}\phi_l + d^1_{0,0}\phi_0 = g0 \tag{3.61}$$

$$\phi_0 = \left(g0 - \sum_{l=1}^{n_r} d^1_{0,l}\phi_l \right) / d^1_{0,0} \tag{3.62}$$

therefore the form of the linear system of equations is

$$\sum_{l=1}^{n_r}(dr^2_{i,l} - (dr^2_{i,0}/d^1_{0,0})d^1_{0,l})\phi_l = f_i - ((dr^2_{i,0}/d^1_{0,0}) * g0 \tag{3.63}$$

3.4 Solution of the linear system of equations: Diagonalization method

Applying spectral method to a discretized differential equation, gives as result a linear system of equations which is required to be solved with high accuracy. For this reason a direct method is preferred to an iterative method. In spectral method for collocation with Chebyshev polynomials and Gauss Lobatto points, the matrix of the linear system of equations can be diagonalized. As is well known this property allows one to rewrite the matrix in terms of its eigenvectors and eigenvalues. This procedure is described in detail in references [12] and [17] here we present only a brief summary.

For an efficient application of the matrix-diagonalization technique in the two-dimensional case, it is convenient to write the discrete system to be solved in the following matrix form,

$$\mathcal{D}_x\mathcal{U} + \mathcal{U}\mathcal{D}_y^T - \sigma U = \mathcal{H}, \tag{3.64}$$

where $\mathcal{U}$ is the matrix of dimension $\bar{N}_x \times \bar{N}_y$, with the inner unknowns $\bar{N}_x = \bar{N}_x - 1$ and $\bar{N}_y = \bar{N}_y - 1$, i.e.

$$\mathcal{U} = [u_N(x_i, y_i)], \qquad i = 1, ..., \bar{N}_x, \qquad j = 1, ..., \bar{N}_y, \tag{3.65}$$

In equation (3.64) $\mathcal{D}_x$ and $\mathcal{D}_y$ are matrices of dimension $\bar{N}_x \times \bar{N}_y$, analogous to the one-dimensional case described in equations (3.38),(3.44),(3.54). $\mathcal{H}$ is an $\bar{N}_x \times \bar{N}_y$ matrix containing the inner values of f and the boundary conditions.

Let us denote by Λ_x and Λ_y the diagonal matrices whose whose entries are the eigenvalues $\Lambda_{x,i}, i = 1, ..., \bar{N}_x$ and $\Lambda_{y,j}, j = 1, ..., \bar{N}_y$ of the matrices $\mathcal{D}_x$ and $\mathcal{D}_y$ respectively, so that

$$\mathcal{D}_x = \mathcal{P}\Lambda_x\mathcal{P}^{-1}, \qquad \mathcal{D}_y = \mathcal{Q}\Lambda_y\mathcal{Q}^{-1}, \tag{3.66}$$

where $\mathcal{P}$ and $\mathcal{Q}$ are the matrices whose columns are the eigenvectors of matrix (3.38).

In summary, the calculation steps of the algorithm are:

1. Calculate $\tilde{\mathcal{H}} = \mathcal{P}^{-1}\mathcal{H}$
2. Calculate $\hat{\mathcal{H}} = \tilde{\mathcal{H}}(\mathcal{Q}^T)^{-1}$
3. Calculate $\hat{\mathcal{U}}$ with

$$\hat{u}_{i,j} = \frac{\hat{h}_{i,j}}{\Lambda_{x,i} + \Lambda_{y,j} - \sigma}, \qquad i = 1, ..., \bar{N}_x, \qquad j = 1, ..., \bar{N}_y, \tag{3.67}$$

4. Calculate $\tilde{\mathcal{U}} = \hat{\mathcal{U}}\mathcal{Q}^T$
5. Calculate $\mathcal{U} = \mathcal{P}\tilde{\mathcal{U}}$
6. Calculate the boundary values

The computational effort associated with the matrix-diagonalization procedure is made of two parts. The first part consists of the calculation of the eigenvalues and eigenvectors, as well as the inversion of the eigenvector matrices. This part is called preprocessing and it has to be made only once. In the second part, described in the above algorithm, essentially four matrix-matrix products have to be performed.

3.5 Numerical solution of fluid dynamics equations using spectral methods

In this section we will show how to implement spectral methods to the numerical solution of the conservation equations of fluid dynamics.

Consider the mass conservation equation of a Newtonian incompressible fluid

$$\nabla \cdot \vec{u} = 0 \tag{3.68}$$

the momentum conservation equation (Navier-Stokes equations) in non-dimensional form is:

$$\frac{\partial \vec{u}}{\partial t} + \vec{u} \cdot \nabla \vec{u} = -\nabla p + \frac{1}{Re}\nabla^2 \vec{u} + \vec{F} \qquad \text{in} \qquad \Omega \tag{3.69}$$

where $\vec{u}$ is the velocity vector, p is the static pressure, $\vec{F}$ a body force and Re the Reynolds number characteristic of the flow.

The conservation equations are a system of four parabolic, non-linear, coupled partial differential equations. Many authors used spectral method for the numerical solution of incompressible flows, see references [18], [19], [20] for a detailed description.

The numerical solution using Chebyshev pseudo-spectral (or collocation) method has the following properties

- High spectral accuracy
- No spurious modes other than the physical one (constant mode)
- No staggered grids.
- No special treatment of convective terms.

To begin, first we put the conservation equation in the following form

$$\nabla \cdot \vec{u} = 0 \qquad \text{in} \qquad \Omega \tag{3.70}$$

$$\frac{\partial \vec{u}}{\partial t} + N(\vec{u}) = -\nabla p + \frac{1}{Re} L(\vec{u}) + \vec{F} \qquad \text{in} \qquad \Omega \tag{3.71}$$

Specific initial and boundary conditions $\vec{W}$ are given for the velocity field, such that

$$\vec{u} = \vec{W} \qquad \text{on} \qquad \partial\Omega \qquad \text{and} \qquad \vec{u}^0 = \vec{W}^0 \qquad \text{t=0} \qquad \text{in} \qquad \Omega \tag{3.72}$$

with

$$\nabla \cdot \vec{W}^0 = 0 \qquad \text{in} \qquad \Omega. \tag{3.73}$$

The first step to derive a Poisson equation for the pressure from equations (3.70), and (3.71)

$$\nabla^2 p = \nabla \cdot [-N(\vec{u}) + \vec{F}] \qquad \text{in} \qquad \Omega. \tag{3.74}$$

A consistent boundary condition is required to solve this elliptic equation 3.74 because no natural condition exist. A straight consistent Neumann condition can be derived form form equations 3.70, 3.71

$$\frac{\partial p}{\partial n} = \hat{n} \cdot [-\frac{\partial \vec{u}}{\partial t} - N(\vec{u}) + \frac{1}{Re} L(\vec{u}) + \vec{F}] \qquad \text{on} \qquad \partial\Omega \tag{3.75}$$

In this condition Karniadakis [21] have separated the diffusion term $L(\vec{u})$ in solenoidal part, approximated by an explicit scheme, and the irrotational part approximated by an implicit scheme

$$L(\vec{u}) = \nabla(\nabla \cdot \vec{u}) - \nabla \times (\nabla \times \vec{u}) \tag{3.76}$$

The time accuracy for the global solution is directly dependent of the treatment of this pressure boundary condition [21].

3.5.1 Projection method

Since the conservation equations are a coupled partial differential equations, a procedure to handle this difficulty is required. There are many recent papers discussing the solution of the fluid dynamics equations in cylindrical geometries using the spectral method.The details of these methods can be found in references [20], [19] and [22].

The implementation of the algorithm to decouple the governing equations involves the solution of three partial differential equations. The fractional steps procedure is as follows

(i) The predictor for the pressure: before each time integration, solve a preliminary pressure $\bar{p}^{n+1}$ according to the following expression obtained from the Navier-Stokes and continuity equations

$$\nabla^2 \bar{p}^{n+1} = \nabla \cdot [-2N(\vec{u}^n) + N(\vec{u}^{n-1}) + \vec{F}^{n+1}] \qquad \text{in} \qquad \Omega, \tag{3.77}$$

with

$$\frac{\partial p}{\partial n} = \hat{n} \cdot \left[\frac{-3\vec{w}^{n+1} + 4\vec{u}^{n} - \vec{u}^{n-1}}{2\Delta t} - 2N(\vec{u}^{n}) + N(\vec{u}^{n-1}) + \frac{1}{Re}[2L(\vec{u}^{n}) - L(\vec{u}^{n-1})] + \vec{F}^{n+1} \right]. \tag{3.78}$$

(ii) Solve implicitly for a predictor $\vec{u}^{*}$ for the velocity from the momentum equation, including this pressure field

$$\frac{3\vec{u}^{*} - 4\vec{u}^{n} + \vec{u}^{n-1}}{2\Delta t} + 2N(\vec{u}^{n}) - N(\vec{u}^{n-1}) = -\nabla \bar{p}^{n+1} + \frac{1}{Re}\nabla^2 \vec{u}^{*} + \vec{F}^{n+1} \qquad \text{in} \qquad \Omega, \tag{3.79}$$

with the actual boundary condition

$$\vec{u}^{*} = \vec{W}^{n+1} \qquad \text{on} \qquad \partial\Omega. \tag{3.80}$$

(iii) The correction step consists of the explicit evaluation of the final divergence free velocity field defined by

$$\frac{3\vec{u}^{n+1} - 3\vec{u}^{*}}{2\Delta t} = -\nabla(p^{n+1} - \bar{p}^{n+1}) \qquad \text{in} \qquad \bar{\Omega} = \Omega \cup \partial\Omega \tag{3.81}$$

and

$$\nabla \cdot \vec{u}^{n+1} = 0 \qquad \text{in} \qquad \Omega \tag{3.82}$$

with

$$\hat{n} \cdot \vec{u}^{n+1} = \hat{n} \cdot \vec{W}^{n+1} = \hat{n} \cdot \vec{u}^{*} \qquad \text{on} \qquad \partial\Omega \tag{3.83}$$

This step is solved through an intermediate variable ϕ, defined as

$$\phi = \frac{2\Delta t}{3}(p^{n+1} - \bar{p}^{n+1}). \tag{3.84}$$

Taking the divergence of equation (3.81) with (3.84) yields a Poisson equation for ϕ

$$\nabla^2 \phi = \nabla \cdot \vec{u}^{*} \qquad \text{in} \qquad \Omega, \tag{3.85}$$

with the consistent Neumann boundary condition

$$\frac{\partial \phi}{\partial n} = 0 \qquad \text{on} \qquad \partial\Omega. \tag{3.86}$$

Finally, update the corrected pressure and velocity fields in $\bar{\Omega} = \Omega \cup \partial\Omega$

$$p^{n+1} = \bar{p}^{n+1} + \frac{3}{2\Delta t}\phi, \tag{3.87}$$

$$\vec{u}^{n+1} = \vec{u}^{*} - \nabla\phi. \tag{3.88}$$

This method is very powerful because it includes high order integration methods and a spectral discretization schemes.

The design of the spectral method is very important since, a properly constructed spectral method can be used to obtain solutions very accurate and efficient, but a poorly designed spectral method may perform much worse than simpler finite difference or finite element techniques.

CHAPTER 4

Mixed Fourier Galerkin – finite volume method to solve the fluid dynamics equations in cylindrical geometries[1]

In this chapter, we describe a hybrid method based on the combined use of Fourier Galerkin and finite volume techniques to solve the fluid dynamics equations in cylindrical geometries. The proposal is to use a Fourier expansion in the angular direction, partially translating the problem to the Fourier space and then solve the resulting equations using a finite volume technique. We also describe an algorithm required to solve the coupled mass and momentum conservation equations similar to a pressure correction method [23] that was adapted for the present formulation .

Using the Fourier Galerkin method for the azimuthal direction has two advantages. First, it has a high order approximation of the partial derivatives in the angular direction, and second, it naturally satisfies the azimuthal periodic boundary conditions. In contrast, using finite volume method in the radial and axial directions, allows one to handle boundary conditions with discontinuities these directions. Also, the resulting linear system of equations are band diagonal which are easier to solve fast and efficiently. The benefits of the mixed method are illustrated with sample examples.

4.1 Introduction

The formulation of fluid dynamics equations is based on the physical concepts of mass and momentum conservation and constitutive equations, and they form a coupled system of nonlinear partial differential equations. When a numerical solution is sought, the equations for continuous variables must be turned into their approximate discrete versions. The fact that the conservation equations are coupled is an important feature that determines the method for the numerical solution.

---

[1] The concepts contained in this chapter are described in the article 'José Núñez, Eduardo Ramos and Juan M. Lopez. Mixed Fourier-Galerkin-finite-volume method to solve the fluid dynamics equations in cylindrical geometries. Fluid Dynamics Research. 2012'

In this chapter, we present a numerical scheme to solve the fluid dynamics equations in cylindrical geometries. The spatial discretization of the equations is made using a mixed formulation based on the Fourier Galerkin spectral method and the finite volume method. The decoupling strategy used to solve the momentum equations is an iterative procedure, first calculating an intermediate velocity field based on an estimated pressure field and then obtaining appropriate corrections to satisfy the continuity equation.

Several numerical algorithms to solve the fluid dynamics equations in the cylindrical coordinate system have been reported in the literature. The well known discretization methods, finite difference/finite volume have been used in these algorithms, see for instance [10], [24], [11]. These studies explore the convenience of using discretization schemes like central differences, high-order compact or energy-conservative. Also, different treatments to avoid the singularity in the axis have been presented and discussed. The decoupling strategies examined in these investigations include the fractional step or projection method [25] and the SIMPLE algorithm introduced by Patankar [23]. With these methods, it is possible to find the solution to the a pressure equation by a sequence of steps. Briefly, the projection method can be described as follows: First, ignoring the pressure gradient and the continuity equation, the Navier-Stokes equations are solved to obtain a first guess of the velocity field; then, the velocity distribution is projected over a divergence free space, this is done by solving a Poisson equation for the pressure with Neumann boundary conditions. Another decoupling strategy frequently used together with the finite volume method is the Semi Implicit Method for Pressure Linked Equations (SIMPLE), this method is an iterative procedure to solve the system of equations and consists of the following steps. First, the momentum equations are solved using a guessed value for the pressure to get a first approximation for the velocity; a pressure corrections is then calculated using the mass conservation equation. The process is repeated until the velocity satisfies the divergence free condition. Many improvements that accelerate the convergence rate of this iterative procedure are available in the literature [26], [27], [28]. A major feature to be considered in the implementation of finite differences in cylindrical coordinates is the periodicity in the azimuthal direction. To satisfy the periodic boundary condition, the domain must be chosen to exceed the period length by one cell width resulting in an overlap of the first an the last cells. The velocity, and the pressure are to be set to coincide in the overlap cells. The resulting linear system of equations is a slightly perturbed tridiagonal system, that can be solved, for instance, using Gaussian elimination [29].

If the system under analysis can be conveniently described in terms of a spatially cyclic coordinate, the harmonic functions are the natural basis to represent the dependent variables since these functions automatically and individually satisfy the periodic conditions. The Fourier representation and the corresponding identification of the expansion coefficients are the basic idea behind the spectral methods. The numerical solution of incompressible viscous flows in cylindrical domains using spectral methods have been published in many studies, like for instance references [30], [18], [19]. A further advantage of this representation is that for an equivalent computational effort, the solution is more accurate since the error decays exponentially. For this reason, Fourier spectral methods have been used for direct numerical simulations of turbulent flows [13] or as a tool for an stability analyses in fluid flows [31]. In most works, the spatial discretization for the azimuthal direction is done with Fourier series, while Chebyshev or Legendre polynomials are used for the radial and axial directions. Examples of these analyses are references [12] or [32]. The pressure-velocity decoupling strategies that have been used with the spectral methods representation are for example, projection methods [20] and influence matrix [33]. In spite of their advantages, spectral methods are not well suited for problems with discontinuities in the axial or radial directions due to the occurrence of Gibbs phenomenon. The linear system of equations resulting from the spectral discretization methods is full and therefore, more difficult to solve that. In these cases it turns out that using a finite volume discretization is more convenient.

A mixed formulation that includes finite volume and Fourier spectral method can take advantage of the two techniques described in the previous paragraph. Barbosa and Daube [34] implemented a mixed Fourier/finite-difference method to solve fluid dynamics equations in cylindrical geometries. Their work is closely related to the present study and deserves a somewhat detailed description. The integration is based upon the use of mimetic discrete first-order operators (divergence, gradient, curl). The non-linear terms were discretized in such a way that they are energetically neutral. No artificial boundary conditions are required on the axis $r = 0$ since they used a *ad hoc* definition for the divergence operator at the centers of the cells adjacent to the axis, and for the definition of the axial component of the vorticity on the axis. The velocity-pressure coupling is handled by means of an incremental projection method. It must be observed however that these fractional step methods introduce an error on the tangential component of the velocity along the boundary, which is sometimes referred as a spurious numerical boundary layer. They solved the flow in a circular lid driven cavity and the flow in a cylindrical tank with a rotating lid.

In this work, we propose a mixed method to solve the conservation equations in a cylindrical domain. Fourier expansion is used in the azimuthal direction, and finite volume discretization is the radial and axial directions. Also, we implement a pressure correction method to handle velocity-pressure coupling in fluid dynamics equations. The idea is to calculate pressure and velocity corrections for each Fourier mode of the solution's expansion until mass conservation is fullfilled. This can be made because the linear system of equations obtained in the finite volume discretization is sparse, band diagonal due to the local approximation.

In the next section, we describe the procedure to implement a mixed Fourier-Galerkin and finite volume method to discretize the fluid dynamics equations in cylindrical coordinates. In a following section, we present the pressure decoupling strategy. Finally we describe examples of solutions obtained with the hybrid method.

4.2 Conservation equations and Fourier expansion

The conservation equations for an incompressible fluid in cylindrical coordinates (θ, r, z) with velocity (u, v, w) can be written as

$$\frac{\partial v}{\partial t} + (\vec{u} \cdot \nabla)v - \frac{u^2}{r} = -\frac{\partial p}{\partial r} + \Gamma \left(\nabla^2 v - \frac{v}{r^2} - \frac{2}{r^2}\frac{\partial u}{\partial \theta} \right) + f_r \,, \tag{4.1}$$

$$\frac{\partial u}{\partial t} + (\vec{u} \cdot \nabla)u + \frac{uv}{r} = -\frac{1}{r}\frac{\partial p}{\partial \theta} + \Gamma \left(\nabla^2 u - \frac{u}{r^2} + \frac{2}{r^2}\frac{\partial v}{\partial \theta} \right) + f_\theta \,, \tag{4.2}$$

$$\frac{\partial w}{\partial t} + (\vec{u} \cdot \nabla)w = -\frac{\partial p}{\partial z} + \Gamma \nabla^2 w + f_z, \tag{4.3}$$

$$\frac{1}{r}\frac{\partial}{\partial r}(rv) + \frac{1}{r}\frac{\partial u}{\partial \theta} + \frac{\partial w}{\partial z} = 0\,, \tag{4.4}$$

where

$$\vec{u} \cdot \nabla = v\frac{\partial}{\partial r} + \frac{u}{r}\frac{\partial}{\partial \theta} + w\frac{\partial}{\partial z}\,, \tag{4.5}$$

and

$$\nabla^2 = \frac{1}{r}\frac{\partial}{\partial r}\left(r\frac{\partial}{\partial r} \right) + \frac{1}{r^2}\frac{\partial^2}{\partial \theta^2} + \frac{\partial^2}{\partial z^2}\,. \tag{4.6}$$

We start by rewriting the equations for the velocity components in a convenient form for the analysis. The expression for the azimuthal velocity component is

$$\frac{\partial u}{\partial t} + N_u = -\frac{1}{r}\frac{\partial p}{\partial \theta} + \Gamma \nabla^2 u + f_u\,, \tag{4.7}$$

where

$$N_u = (\vec{u} \cdot \nabla)u + \frac{uv}{r}\,, \tag{4.8}$$

is the nonlinear term and

$$f_u = \Gamma \left(-\frac{u}{r^2} + \frac{2}{r^2}\frac{\partial v}{\partial \theta} \right) + f_\theta\,, \tag{4.9}$$

is the body force plus terms that arise in the cylindrical coordinate formulation. Similar expressions can be written for the axial and radial components.

We approximate the velocity, pressure, N and f with truncated Fourier series expansions in the azimuthal direction as follows

$$u = \sum_{k=-K/2}^{K/2-1} \hat{u}_k e^{ik\theta}, \quad v = \sum_{k=-K/2}^{K/2-1} \hat{v}_k e^{ik\theta}, \quad w = \sum_{k=-K/2}^{K/2-1} \hat{w}_k e^{ik\theta}, \quad \theta \in [0, 2\pi)\,, \tag{4.10}$$

$$p = \sum_{k=-K/2}^{K/2-1} \hat{p}_k e^{ik\theta}, \quad N = \sum_{k=-K/2}^{K/2-1} \hat{N}_k e^{ik\theta}, \quad f = \sum_{k=-K/2}^{K/2-1} \hat{f}_k e^{ik\theta}, \quad \theta \in [0, 2\pi)\,, \tag{4.11}$$

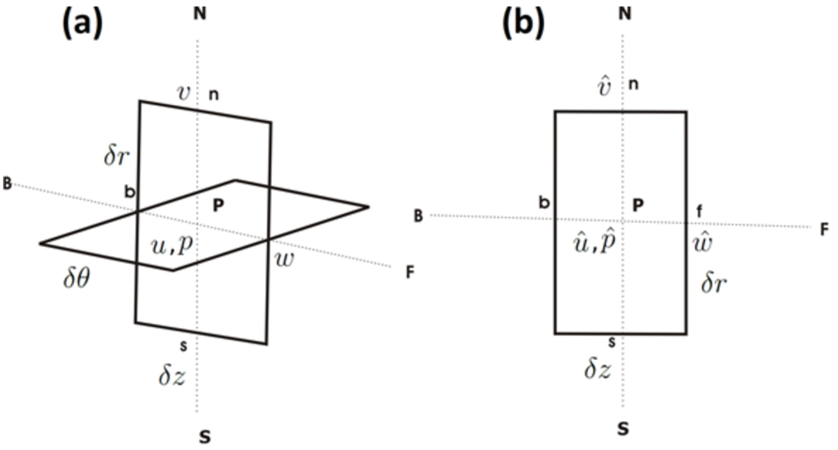

Figure 4.1: Staggered arrangement: (*a*) control volume in the physical space, and (*b*) control volume in Fourier space.

where $\hat{u}_k, \hat{v}_k, \hat{w}_k, \hat{N}_k$ and $\hat{f}_k$, are the Fourier expansion coefficients of the corresponding variables. In the previous expressions, K collocation points are used to evaluate the discrete Fourier transform.

Substituting Fourier expansions (4.10) and (4.11) into equations (4.1)–(4.4), the governing equations can be written in terms of the Fourier modes.

4.3 Discrete equations

The mass conservation equation (4.4) is expressed in terms of the Fourier modes as

$$\frac{ik}{r}\hat{u} + \frac{1}{r}\frac{\partial}{\partial r}(r\hat{v}) + \frac{\partial \hat{w}}{\partial z} = 0, \quad \text{for all } k\,. \tag{4.12}$$

For simplicity, the subindex k has been omitted and also, the range for k is only specified when required to avoid confusion.

The resulting equations are discretized with the finite-volume method. All equations are integrated on a control volume (Fig. 4.1), where the integral over the volume is approximated by the middle-point rule. As is commonly implemented in finite-volume techniques, we use a staggered arrangement for the velocity components and scalar fields (see Fig. 4.1*a*). In the present method we have also used a staggered arrangement for the Fourier modes (see Fig. 4.1*b*). Note that since the Fourier projection is only made in the azimuthal direction, the staggered mesh is only shown in the $\hat{v}, \hat{w}$ space.

Using the notation of Fig. 4.1, the discretized mass conservation equation is

$$\begin{aligned}\int_V \left(\frac{ik}{r}\hat{u} + \frac{1}{r}\frac{\partial}{\partial r}(r\hat{v}) + \frac{\partial \hat{w}}{\partial z}\right) dV \quad &= \tfrac{ik}{r_P}\hat{u}_P\delta V + \tfrac{1}{r_P}\tfrac{r_n\hat{v}_n - r_s\hat{v}_s}{\delta r}\delta V + \tfrac{\hat{w}_f - \hat{w}_b}{\delta z}\delta V\,, \\ &= \tfrac{ik}{r_P}\hat{u}_P\delta V + \hat{v}_n A_n - \hat{v}_s A_s + \hat{w}_f A_s - \hat{w}_b A_b\,, \end{aligned} \tag{4.13}$$

where $\delta V = r_P \delta r \delta\theta \delta z$, $A_n = r_n \delta\theta\delta z$, $A_s = r_s \delta\theta\delta z$, and $A_f = A_b = r_P \delta r \delta\theta$.

The equation for the u-component, in terms of the Fourier modes, with the time derivative approximated using the backward-Euler method, is

$$\frac{\hat{u} - \hat{u}^0}{\delta t} + \hat{N}_u^0 = -\frac{ik}{r}\hat{p} + \Gamma\left(\frac{1}{r}\frac{\partial}{\partial r}\left(r\frac{\partial \hat{u}}{\partial r}\right) - \frac{k^2}{r^2}\hat{u} + \frac{\partial^2 \hat{u}}{\partial z^2}\right) + \hat{f}_u^0 \,. \tag{4.14}$$

Rearranging, we have

$$\left(\frac{1}{\delta t} + \Gamma\frac{k^2}{r^2}\right)\hat{u} = -\frac{ik}{r}\hat{p} + \Gamma\left(\frac{1}{r}\frac{\partial}{\partial r}\left(r\frac{\partial \hat{u}}{\partial r}\right) + \frac{\partial^2 \hat{u}}{\partial z^2}\right) + \hat{f}_u^0 - \hat{N}_u^0 + \frac{\hat{u}^0}{\delta t}. \tag{4.15}$$

Integrating over a control volume gives

$$\begin{aligned}\left(\frac{1}{\delta t} + \Gamma\frac{k^2}{r_P^2}\right)\hat{u}_P\delta V = \ & \Gamma\left(\tfrac{\hat{u}_N - \hat{u}_P}{\delta r}A_n - \tfrac{\hat{u}_P - \hat{u}_S}{\delta r}A_s + \tfrac{\hat{u}_F - \hat{u}_P}{\delta z}A_f - \tfrac{\hat{u}_P - \hat{u}_B}{\delta z}A_b\right) \\ & + \left(\hat{f}_{u_P}^0 - \hat{N}_{u_P}^0 + \tfrac{\hat{u}_P^0}{\delta t}\right)\delta V - \tfrac{ik}{r_P}\hat{p}_P\delta V \,,\end{aligned} \tag{4.16}$$

which can be expressed as the following linear system

$$a_P\hat{u}_P = a_N\hat{u}_N + a_S\hat{u}_S + a_F\hat{u}_F + a_B\hat{u}_B + S_{\hat{u}_P} - \frac{ik}{r_P}\hat{p}_P\delta V, \tag{4.17}$$

where

$$a_N = \Gamma\tfrac{A_n}{\delta r}, \quad a_S = \Gamma\tfrac{A_s}{\delta r}, \quad a_F = \Gamma\tfrac{A_f}{\delta z}, \quad a_B = \Gamma\tfrac{A_b}{\delta z}, \tag{4.18}$$

$$a_P = a_N + a_S + a_F + a_B + \left(\tfrac{1}{\delta t} + \Gamma\tfrac{k^2}{r_P^2}\right)\delta V, \tag{4.19}$$

$$S_{\hat{u}_P} = \left(\hat{f}_{u_P}^0 - \hat{N}_{u_P}^0 + \tfrac{\hat{u}_P^0}{\delta t}\right)\delta V. \tag{4.20}$$

Applying analogous approximations and discretizations to the radial momentum conservation equation (v-velocity component), the following linear system is obtained

$$a_P\hat{v}_P = a_N\hat{v}_N + a_S\hat{v}_S + a_F\hat{v}_F + a_B\hat{v}_B + S_{\hat{v}_P} - (\hat{p}_N - \hat{p}_P)A_p \,, \tag{4.21}$$

where $A_p = \delta V/\delta r$, and the coefficients are

$$a_N = \Gamma\tfrac{A_n}{\delta r}, \quad a_S = \Gamma\tfrac{A_s}{\delta r}, \quad a_F = \Gamma\tfrac{A_f}{\delta z}, \quad a_B = \Gamma\tfrac{A_b}{\delta z}, \tag{4.22}$$

$$a_P = a_N + a_S + a_F + a_B + \left(\tfrac{1}{\delta t} + \Gamma\tfrac{k^2}{r_P^2}\right)\delta V, \tag{4.23}$$

$$S_{\hat{v}_P} = \left(\hat{f}_{v_P}^0 - \hat{N}_{v_P}^0 + \tfrac{\hat{v_P}^0}{\delta t}\right)\delta V \,. \tag{4.24}$$

The axial momentum conservation equation (w-velocity component) can be treated similarly to get

$$a_P\hat{w}_P = a_N\hat{w}_N + a_S\hat{w}_S + a_F\hat{w}_F + a_B\hat{w}_B + S_{\hat{w}_P} - (\hat{p}_F - \hat{p}_P)A_f \,, \tag{4.25}$$

where

$$a_N = \Gamma \tfrac{A_n}{\delta r}, \quad a_S = \Gamma \tfrac{A_s}{\delta r}, \quad a_F = \Gamma \tfrac{A_f}{\delta z}, \quad a_B = \Gamma \tfrac{A_b}{\delta z}, \tag{4.26}$$

$$a_P = a_N + a_S + a_F + a_B + \left(\tfrac{1}{\delta t} + \Gamma \tfrac{k^2}{r_P^2} \right) \delta V, \tag{4.27}$$

$$S_{\hat{w}_P} = \left(\hat{f}^0_{w_P} - \hat{N}^0_{w_P} + \tfrac{\hat{w_P}^0}{\delta t} \right) \delta V\,. \tag{4.28}$$

4.3.1 Nonlinear terms

The nonlinear terms in the conservation of momentum equations $\hat{N}^0_w$ are part of the source terms in the discretized equations. The nonlinear terms are calculated with a central difference scheme

$$\left(w \frac{\partial w}{\partial z} \right)_P \approx w_P \left(\frac{w_F - w_B}{2\delta z} \right). \tag{4.29}$$

Observe that other approximations, such as upwind or QUICK, could be used. Now, the nonlinear terms must be expressed in Fourier modes, and the most convenient way to do this is to calculate the products in physical space and then Fourier transform the products.

4.3.2 Axis treatment

Different treatments for the radial velocity at the origin have been proposed by many authors in the context of the finite volume discretization method ([10], [11]). These strategies can also be implemented in the present formulation for the Fourier mode equations. Frequently, an artificial boundary condition for the radial velocity v at the origin is used. Two examples are the Neumann-like condition $v(i, 0, k) = v(i, 1, k)$ and the streamwise average of the radial velocities $v(i, 0, k) = ((v(i, 1, k) + v(i + n_\theta/2, 1, k))/2$.

4.4 Pressure-velocity decoupling strategy

There are many decoupling strategies for the fluid dynamics equations. One of these methods is known as pressure-correction method [23] where a pressure field is guessed to solve the Navier-Stokes equations. If the velocity field does not satisfy the continuity equation, then a pressure correction is calculated to better approximate the velocity solution. This procedure is repeated until the mass conservation is satisfied.

4.4.1 Pressure correction method

Let $\hat{p}^*$ denote an initial guess for pressure. According to expressions (4.17), (4.21), and (4.25), the velocity corresponding to such a pressure field is $\hat{u}^*$, $\hat{v}^*$ and $\hat{w}^*$, given by

$$a_P\hat{u}^*_P = \sum_{nb} a_{nb}\hat{u}^*_{nb} + S_{\hat{u}_P} - \frac{ik}{r_P}\hat{p}^*_P\delta V\,, \tag{4.30}$$

$$a_P\hat{v}^*_P = \sum_{nb} a_{nb}\hat{v}^*_{nb} + S_{\hat{v}_P} - (\hat{p}^*_N - \hat{p}^*_P)A_p\,, \tag{4.31}$$

and

$$a_P\hat{w}^*_P = \sum_{nb} a_{nb}\hat{w}^*_{nb} + S_{\hat{w}_P} - (\hat{p}^*_F - \hat{p}^*_P)A_f\,. \tag{4.32}$$

Note that $\hat{u}^*$, $\hat{v}^*$ and $\hat{w}^*$ in general do not satisfy the incompressibility condition. The pressure and velocity corrections $(\hat{p}'_k, \hat{u}'_k)$ are defined by

$$\hat{p}_k = \hat{p}^*_k + \hat{p}'_k\,, \tag{4.33}$$

and

$$\hat{u}_k = \hat{u}^*_k + \hat{u}'_k, \quad \hat{v}_k = \hat{v}^*_k + \hat{v}'_k, \quad \hat{w}_k = \hat{w}^*_k + \hat{w}'_k\,. \tag{4.34}$$

Subtracting (4.30), (4.31) and (4.32) from (4.17),(4.21) and (4.25) respectively, we get the following expressions for the velocity corrections

$$a_P\hat{u}'_P = \sum_{nb} a_{nb}\hat{u}'_{nb} - \frac{ik}{r_P}\hat{p}'_P\delta V\,, \tag{4.35}$$

$$a_P\hat{v}'_P = \sum_{nb} a_{nb}\hat{v}'_{nb} - (\hat{p}'_N - \hat{p}'_P)A_p\,, \tag{4.36}$$

$$a_P\hat{w}'_P = \sum_{nb} a_{nb}\hat{w}'_{nb} - (\hat{p}'_F - \hat{p}'_P)A_f\,. \tag{4.37}$$

Subtracting $\sum_{nb} a_{nb}\hat{u}'_p$ from both sides of the first equation of the previous set, and the corresponding expressions for the second and third equations, gives

$$\left(a_P - \sum_{nb} a_{nb}\right)\hat{u}'_P = \sum_{nb} a_{nb}(\hat{u}'_{nb} - \hat{u}'_p) - \frac{ik}{r_P}\hat{p}'_P\delta V\,, \tag{4.38}$$

$$\left(a_P - \sum_{nb} a_{nb}\right)\hat{v}'_P = \sum_{nb} a_{nb}(v'_{nb} - v'_p) - (\hat{p}'_N - \hat{p}'_P)A_p\,, \tag{4.39}$$

and

$$\left(a_P - \sum_{nb} a_{nb}\right)\hat{w}'_P = \sum_{nb} a_{nb}(w'_{nb} - w'_p) - (\hat{p}'_F - \hat{p}'_P)A_f\,. \tag{4.40}$$

If the term $\sum_{nb} a_{nb}(\hat{u}'_{nb} - \hat{u}'_p)$ is neglected, equations for the correction of the velocity components in terms of the pressure correction are obtained as

$$\hat{u}'_P = -\frac{\delta V}{a_P - \sum_{nb} a_{nb}} \frac{ik}{r_P} \hat{p}'_P = -d_u \frac{ik}{r_P} \hat{p}'_P \,, \tag{4.41}$$

$$\hat{v}'_P = -\frac{A_p}{a_P - \sum_{nb} a_{nb}} (\hat{p}'_N - \hat{p}'_P) = -d_v (\hat{p}'_N - \hat{p}'_P) \,, \tag{4.42}$$

and

$$\hat{w}'_P = -\frac{A_f}{a_P - \sum_{nb} a_{nb}} (\hat{p}'_F - \hat{p}'_P) = -d_w (\hat{p}'_F - \hat{p}'_P) \,. \tag{4.43}$$

Substituting equations (4.41)–(4.43) into the mass conservation equation (4.13) gives

$$\frac{ik}{r_P}(\hat{u}^*_P + \hat{u}'_P)\delta V + (\hat{v}^*_n + \hat{v}'_n)A_n - (\hat{v}^*_s + \hat{v}'_s)A_s + (\hat{w}^*_f + \hat{w}'_f)A_s - (\hat{w}^*_b + \hat{w}'_b)A_b = 0 \,, \tag{4.44}$$

and the following expression for the pressure correction is obtained

$$a_P \hat{p}'_P = a_N \hat{p}'_N + a_S \hat{p}'_S + a_F \hat{p}'_F + a_B \hat{p}'_B + S_P \,, \tag{4.45}$$

where

$$a_N = (d_v)_n A_n, \quad a_S = (d_v)_s A_s \,, \tag{4.46}$$

$$a_F = (d_w)_f A_f, \quad a_B = (d_w)_b A_b \,, \tag{4.47}$$

$$a_P = a_N + a_S + a_F + a_B + \tfrac{k^2}{r_P^2} * d_u * \delta V \,, \tag{4.48}$$

$$S_P = -(\tfrac{ik}{r_P} \hat{u}^*_P \delta V + \hat{v}^*_n A_n - \hat{v}^*_s A_s + \hat{w}^*_f A_s - \hat{w}^*_b A_b) \,. \tag{4.49}$$

Note that the linear system of equations for the pressure correction contains complex numbers, but the entries of the matrix are real and therefore no calculations in the complex domain are necessary to find the inverse matrix.

When the pressure correction equation is solved, the pressure and velocity are modified to get a better approximation. In the next iteration step, the updated values are used as initial guesses and the procedure is repeated until the velocity satisfies the divergence-free criterion.

4.5 Validation of the methodology

Two examples are presented to illustrate the applicability of the proposed methodology for the numerical solution of Navier-Stokes equations in cylindrical domains. In the examples, one or more important characteristics that a robust method must have and a comparison with the corresponding numerical solution using a finite-volume method and Fourier-Chebyshev spectral method is presented. The algorithms used to solve the example problems with a finite-volume method and a Fourier-Galerkin and Chebyshev spectral method can be found in the literature [11, 8, 12, 15].

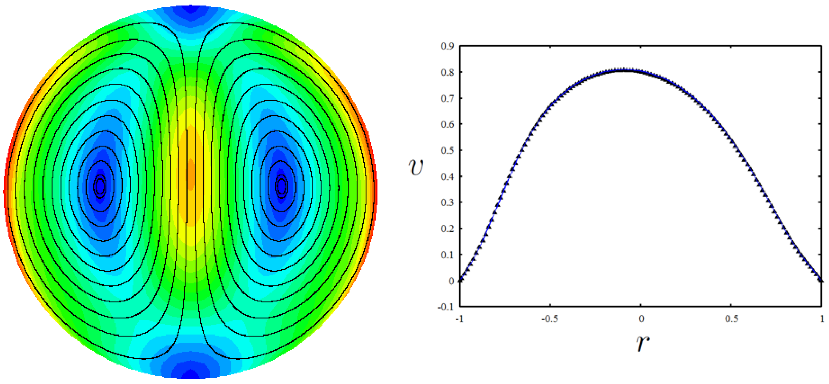

Figure 4.2: Streamlines and magnitude of the velocity field of the lid-driven flow at $Re = 400$ (left), and (right) radial velocity profiles at $\theta = \pi/4$ using a spectral method (continuous line) and Fourier/finite-volume method (triangular dots).

4.5.1 Lid driven flow

The first example is the lid driven flow in a circular domain with the tangential velocity condition at the outer radius defined by $u = \cos\theta$ for a Reynolds number $Re = 400$; the same conditions as in [34]. The motion of the boundary generates a flow with non-zero flow at r=0 and therefore, a correct calculation of the radial velocity at the origin is very important for an accurate numerical solution. In this particular calculation the streamwise average condition (see §4.3.2) strategy was used to avoid the singularity at the origin. The solution obtained with a Fourier-Chebyshev spectral method does not require any special treatment at the origin and can be used as a reference for a quantitative assessment. The left panel of Fig. 4.2 shows a color map for the velocity magnitude and the corresponding streamlines. The right panel shows radial velocity profiles at $\theta = \pi/4$ obtained from the two solution techniques; the flow field around the origin is smooth and the two radial velocity profiles agree.

We use the total kinetic energy $\mathcal{K}$ to compare the solutions obtained with the three different methods described previously. $\mathcal{K}$ is defined by

$$\mathcal{K} = \frac{1}{V}\int (u^2 + v^2)dV\,, \tag{4.50}$$

where V is the volume occupied by the fluid. In principle, to determine the convergence of the approximate solution, it would be necessary to know *a priori* the exact solution; but such information is usually unknown. An alternative criterion for the grid convergence error of steady-state flows can be estimated from $\epsilon = |\mathcal{K}_n - \mathcal{K}_{n-1}|/\mathcal{K}_{n_{max}}$, where n denotes the number of points used in the discretization. This relative convergence criterion is shown in Fig. 4.3 for the three integration methods. As can be appreciated, the spectral convergence in the angular direction of the proposed mixed method is very close to that of the Fourier-Chebyshev method, and has significantly better convergence properties than the finite-volume method.

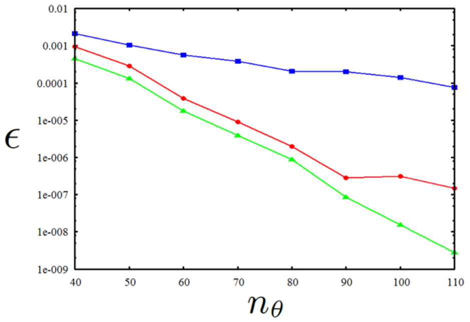

Figure 4.3: Relative convergence for a lid driven flow as a function of n_θ, using the spectral method (green line), Fourier/finite-volume method (red line), and finite-volume method (blue line). In all cases, $n_r = 60$.

4.5.2 Vortex breakdown in a cylindrical tank with a rotating lid.

The second example is the study of vortex breakdown in a cylinder driven by a rotating bottom. The flow is characterized by the aspect ratio $\Lambda = H/R$ where the H is the height and R the radius, and the Reynolds number defined by $Re = \Omega R^2/\nu$, where Ω is the angular velocity. Using a projection scheme for the velocity-pressure decoupling and a Legendre-Fourier approximation for the space variables, at $Re = 2730$ for $\Lambda = 3.0$ axisymmetric flow losses stability to a $m = 4$ rotating wave solution [35]. On increasing Re to 2900, a second bifurcation to a modulated rotating wave takes place, introducing an $m = 1$ mode that manifests itself near the axis. The results obtained with the method proposed here are illustrated in Figs. 4.4 and 4.5. All major features described in previous studies are correctly captured by the present model. Figure 4.4 shows contours of the axial velocity in a meridional plane and in a horizontal plane at $z = 0.8\Lambda$ for $Re = 2800$ and $\Lambda = 3.0$. The mode $m = 4$ flow is clearly observed and is confined to the region near the jet close to the lateral wall, as expected.

As the Reynolds number is increased, a second instability occurs and a modulated rotating wave that causes a precession with an $m = 1$ mode near the axis of symmetry appears. This flow at $Re = 3000$ is illustrated in Fig 4.5 where the secondary instability is well developed. The flow close to the lateral wall displays an $m = 4$ distribution while the flow near axis of the cylinder is clearly non-axisymmetric. The agreement with the results of [35] is very good.

4.6 Conclusions

A technique to solve the Navier-Stokes equations in cylindrical geometries with rigid boundary conditions that combines the advantages of the azimuthal periodicity and accuracy of the spectral methods with the possibility of considering discontinuous boundary

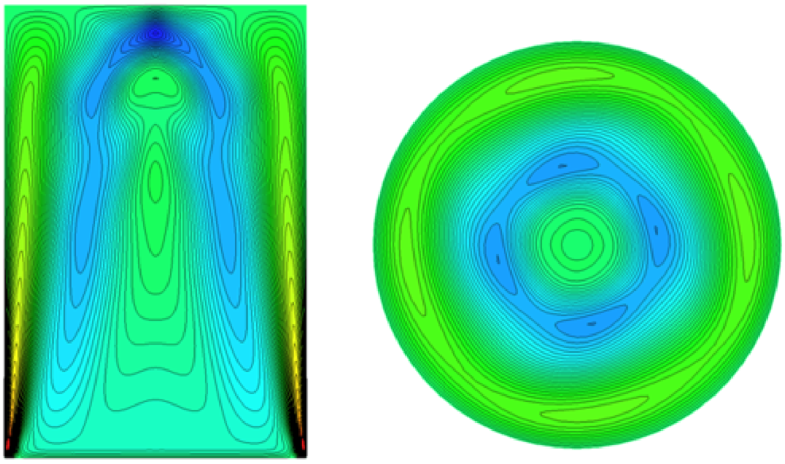

Figure 4.4: Instantaneous contours of the axial velocity of the $m = 4$ rotating wave at $Re = 2800$ and $\Lambda = 3.0$ in a meridional plane (left) and a horizontal plane at $z = 0.8\Lambda$ (right).

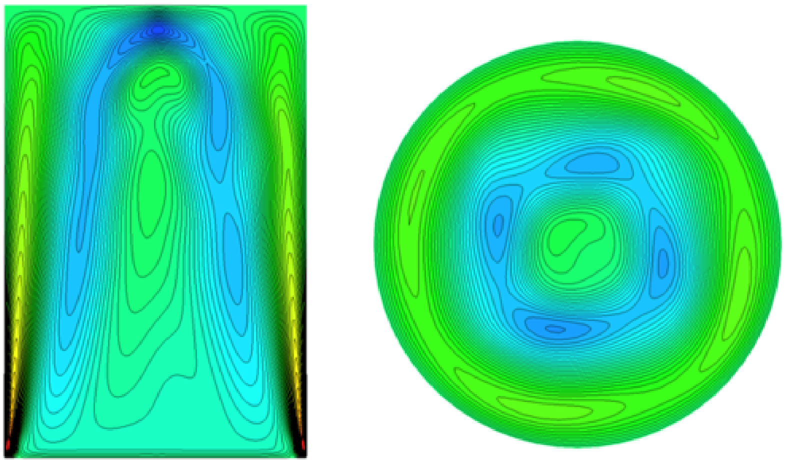

Figure 4.5: Instantaneous contours of the axial velocity of the modulated rotating wave with $m = 4$ and $m = 1$ at $Re = 3000$ and $\Lambda = 3.0$ in a meridional plane (left) and a horizontal plane at $z = 0.8\Lambda$ (right).

conditions in the axial and/or radial directions has been proposed. An important part of the method is a pressure-correction technique where the different Fourier components are required to satisfy mass conservation individually. In all tests, the method was demonstrated to have the expected properties and is potentially useful for a variety of problems that might be more difficult to solve with other methods. In particular, the proposed technique can be used for stability analyses of flows confined to cylindrical containers. It is expected that the present integration strategy will be useful to model flows encountered in the crystal growth processes when the Czochralski or Bridgman techniques are used, as these often have discontinuous boundary conditions.

Chapter 5

Verification and experimental validation of a numerical simulation of natural convection in a slender cylinder [1]

5.1 Introduction

Natural convection in containers this phenomenon has attracted much attention due to potential applications in the field of crystal growth where techniques like Czochralski, Bridgman and zone-melting involve natural convective motions that are determinant for the quality of the crystal. Recent monographs on these process are [36] and [37].

This flow is similar to the Rayleigh-Benard flow that describes the natural convection in a layer of fluid subject to a destabilizing temperature gradient, but with a strong influence of the lateral wall. It is well established that the convective pattern can be specified with three parameters, the aspect ratio (a = height/diameter), the Prandtl number and the Rayleigh number (for the definition of these parameters, see Section 5.2).

Several reviews on the subject that describe the generalities of the natural convective flows have appeared in the literature The works of Chandrasekhar [38] and Koschmieder [1] are comprehensive although somewhat old descriptions. Here, we restrict on review to only the papers that are closely related to our study.

Early investigations clarified the stability of the flow and determined the critical Rayleigh number for the onset of convection as a function of the aspect ratio of the container. The linear perturbation theory of Charlson and Sani [39], [40] is based on a variational formulation and uses the Rayleigh -Ritz method to solve the linearized equations that allows the calculation of the first critical Rayleigh number. They examined the cases where the convective flow is axisymmetric [39] and nonaxisymmetric [40].

Their results indicate that the stable steady state flow is non-axisymmetric (azimuthal mode m=1) for $a > 0.62$ and occurs at $Ra \approx 6590$ for a container with $a = 1.25$ and

---

[1] The concepts contained in this chapter are described in the article 'José Núñez, Miguel Lopez, Eduardo Ramos Guillermo Hernadez-Cruz, Minerva vargas and Sergio Cuevas. Verification and experimental validation of a numerical simulation of natural convection in a slender cylinder. Preprinted submitted'

adiabatic walls. The critical Rayleigh (Ra^{c1})numbers for the onset of convection were also calculated with linear Galerkin method by Buell and Catton [2] finding critical Rayleigh numbers up to 20% smaller than those obtained by Charlson and Sani for the nonaxisymmetric modes.

Experimental investigations of the convective instabilities in closed vertical cylinders have been made using arrangements of thermal sensors [41] to infer global dynamic features of the flow. Although relevant results on the critical Rayleigh numbers have been found with this technique that confirm the theoretical predictions for $a = 3$, details of the motion were not resolved.

The theoretical and experimental investigation of Mueller *et al.* [42] on the convective patterns in cylindrical container is closely related to the present study and deserves a somewhat detailed description. They made qualitative observations of motion inside water filled cylinders with aspect ratios ranging from 0.5 to 5 using the light cut technique which yields observations of the flow patterns in planes. A stability diagram (Ra *vs* a) indicating the regions with no flow, steady and time-dependent flow is presented. They report that the steady, two dimensional flow pattern observed for $a = 1$ and $Ra = 17,500$ is different depending on the orientation of the plane observed. In one section (of unspecified orientation), a single, non-axisymmetric cell is found, while the pattern in the perpendicular section is composed of four rolls. The observations were interpreted with a theoretical model obtained by numerically solving the conservation equations. They described the non-axisymmetric flow patterns obtained for a=1 in terms of the vertical velocity at horizontal planes and explained that the flow is rather complicated with a three dimensional structure.

Neumann [29], obtained a numerical solution based on the finite differences discretization of the conservation equations with boundary conditions corresponding to natural convective flow in cylinders. The solution was found using cylindrical coordinates and a mesh of 20 points in the r, θ and z directions. The aspect ratio of the cylinders considered are 0.5 and 1 which are, according to the linear theories, below and above the critical aspect ratio for the transition from axisymmetric to non-axisymmetric flow patterns. In the second case, he obtains a steady state, non-axisymmetric flow composed of a single convective cell for $Ra = 5 \times 10^4$ and $Pr = 6.7$ with fluid ascending on one side of the cavity and descending on the opposite with the orientation of the roll given by the initial temperature distribution. His results are in qualitative agreement with experimental results of Müller *et al.* [42].

A finite difference method was also used by Crespo *et al.* [43] to simulate natural convection in cylinders. They described the features of steady and time dependent non-axisymmetric convective patterns with $a = 2$ and Prandtl number 0.002.

5.2 Numerical Analysis

The natural convective motion inside the cylindrical container under the conditions of interest can be described by numerically solving the mass, momentum and energy conservation equations. Given that the maximum temperature differences are small, the Boussinesq approximation is used. In the frame of this approximation, the kinematic viscosity ν, the thermal diffusivity α, and the volume expansion coefficient β, are constant. The density ρ is also considered constant except for the body force term in the momentum conservation equation in the axial direction. The cylindrical sidewall is chosen to be adiabatic, i.e. the temperature gradient normal to the wall is set equal to zero. At all container walls the no-slip velocity boundary condition is prescribed.

The set of conservation equations have been solved in its dimensionless form. The scaling we have used was the most convenient for the numerical solution and includes the following characteristic quantities: the axial and radial coordinates are expressed in terms of the height (h) and diameter (D) of the cylinder respectively. The characteristic velocity (u_c) is the free fall velocity, namely $u_c = \sqrt{g\beta\Delta T h}$ where g is the terrestrial gravity acceleration. The symbol $\Delta T = T_H - T_C$ denotes the characteristic temperature scale with T_H and T_C the temperatures of the lower and upper walls respectively. The time scale is defined using the characteristic velocity as h/u_c.

In dimensionless form, the governing equations written in cylindrical coordinates (r, θ, z) are:

$$\frac{1}{r}\frac{\partial}{\partial r}(ru_r) + \frac{1}{r}\frac{\partial u_\theta}{\partial \theta} + \frac{\partial u_z}{\partial z} = 0, \tag{5.1}$$

$$\frac{\partial u_r}{\partial t} + (\vec{u}\cdot\nabla)u_r - \frac{u_\theta^2}{r} = -\frac{\partial p}{\partial r} + \left(\frac{Pr}{Ra}\right)^{\frac{1}{2}} \left(\nabla^2 u_r - \frac{u_r}{r^2} - \frac{2}{r^2}\frac{\partial u_\theta}{\partial \theta}\right), \tag{5.2}$$

$$\frac{\partial u_\theta}{\partial t} + (\vec{u}\cdot\nabla)u_\theta + \frac{u_\theta u_r}{r} = -\frac{1}{r}\frac{\partial p}{\partial \theta} + \left(\frac{Pr}{Ra}\right)^{\frac{1}{2}} \left(\nabla^2 u_\theta - \frac{u_\theta}{r^2} + \frac{2}{r^2}\frac{\partial u_r}{\partial \theta}\right), \tag{5.3}$$

$$\frac{\partial u_z}{\partial t} + (\vec{u}\cdot\nabla)u_z = -\frac{\partial p}{\partial z} + \left(\frac{Pr}{Ra}\right)^{\frac{1}{2}} \nabla^2 u_z + T, \tag{5.4}$$

$$\frac{\partial T}{\partial t} + (\vec{u}\cdot\nabla)T = \left(\frac{1}{RaPr}\right)^{\frac{1}{2}} \nabla^2 T, \tag{5.5}$$

where $\vec{u} = (u_r, u_\theta, u_z)$ is the velocity, p is the pressure and T is the temperature. The differential operators are

$$\vec{u}\cdot\nabla = u_r\frac{\partial}{\partial r} + \frac{u_\theta}{r}\frac{\partial}{\partial \theta} + u_z\frac{\partial}{\partial z}$$

and

$$\nabla^2 = \frac{1}{r}\frac{\partial}{\partial r}\left(r\frac{\partial}{\partial r}\right) + \frac{1}{r^2}\frac{\partial^2}{\partial \theta^2} + \frac{\partial^2}{\partial z^2}.$$

The flow is characterized by two dimensionless parameters, the Rayleigh and Prandtl numbers, defined by

$$Ra = \frac{g\beta\Delta T h^3}{\nu\alpha} \quad \text{and} \quad Pr = \frac{\nu}{\alpha}. \tag{5.6}$$

The boundary conditions corresponding to the physical situation of interest are:

$$T = 0 \quad \text{on} \quad z = 0, \qquad T = 1 \quad \text{on} \quad z = 1, \tag{5.7}$$

$$\frac{\partial T}{\partial r} = 0 \quad \text{on} \quad r = D/2h, \tag{5.8}$$

and

$$\vec{u} = 0 \quad \text{on all boundaries.} \tag{5.9}$$

In most runs, the initial conditions for the time integrations are zero velocity in the whole volume. The temperature and pressure distributions along the axial direction are assumed to be linear and quadratic, respectively.

The governing equations and boundary conditions are invariant under arbitrary rotations about the axis of the cylinder. If R_ψ is a rotation of angle ψ around the z-axis, its action is

$$R_\psi(u, v, w, T, p)(r, \theta, z) = (u, v, w, T, p)(r, \theta + \psi, z). \tag{5.10}$$

This property indicates that if a solution is obtained, the same velocity, pressure and temperature fields with a different orientation with respect to the vertical axis, constitute also a solution. These rotations generate the symmetry group O(2).

The conservation equations were discretized using the finite volume method and then solved numerically. The cylindrical volume is divided in small cells having edge lengths Δr, $r\Delta\theta$ and Δz. The derivatives in time and space were respectively approximated with first order forward differences and second order central differences. An appropriately staggered mesh is used where the velocity components are located at the cell faces and scalar fields are defined at the center of the cell [29]. The SIMPLEC algorithm was used for pressure decoupling [44], [45]. This algorithm is iterative and stops with a small velocity divergence criterion. A mesh refinement calculation was done to verify the accuracy of the numerical solution. In Table 2 we show results for the maximum of the three components of the velocity as functions of the mesh fineness. For further comments on the verification of the solution see Section 5.4.

Mesh	u_θ^{max}	u_r^{max}	u_z^{max}
20 × 20 × 20	8.0424488E-02	7.8527927E-02	0.1240261
30 × 30 × 30	7.9905130E-02	7.8891858E-02	0.1216930
40 × 40 × 40	7.9648100E-02	7.9282701E-02	0.1215185

Table 5.1: Mesh refinement test for numerical accuracy of the steady flow at $Ra = 5.12 \times 10^5$ and $Pr = 6.667$.

5.3 Results

The theoretical and experimental results presented in this section correspond to the interval $3.0 \times 10^5 < Ra < 2.0 \times 10^6$ and in all cases the Prandtl number is 6.67. The conditions chosen for the analysis were determined by limitations in the experimental equipment and also to comply with the restrictions imposed by the Boussinesq approximation. For the smaller Rayleigh numbers considered, the flow was found to be steady, in contrast to the time dependent flow observed for the large Rayleigh numbers. The experimentally determined critical Rayleigh number where the transition occurs is $5.12 \times 10^5 < Ra_c < 1.46 \times 10^6$, while the numerical calculations indicate that the transition occurs at $Ra_c \sim 1.3 \times 10^6$. These results are consistent with the (interpolated) values reported by Mueller *et al.* [42] for the aspect ratio of the cavity studied here. In the following subsection we describe the dynamics of the flow with $Ra = 5.12 \times 10^5$, and in subsection 5.3.2, the time-averaged velocity fields for $Ra = 1.53 \times 10^6$ are presented. The estimation of the experimental uncertainties was made according to the following procedure.

in steady state, 15 pairs of images were captured and averaged for every experimental observation reported. Histograms of the velocity in each individual observation at every point in the velocity field, allow us to calculate a standard deviation of an adjusted normal distribution. Considering the standard deviation as the uncertainty at every point of the interrogation grid, it is possible to build an uncertainty map. In the velocity as a function of position plots the uncertainty in position is due to instrumental precision.

5.3.1 Steady flow

For clarity in the presentation, we start by describing the structure of the flow using information from the numerical solution. Once we have identified the dominant features of the flow patterns, we proceed to compare with the experimental velocity fields. The velocity and temperature fields obtained with the numerical integration for $Ra = 5.12 \times 10^5$, which corresponds to steady flow, for two mutually perpendicular vertical planes, are shown in Figures 5.1 and 5.3, respectively. The planes on the left and right panels of these figures are labeled AA' and BB' respectively. The left panel of Figure 5.1 shows that the dominant flow pattern in plane AA' is a single convective cell rotating clockwise with its center defined by the point of vanishing velocity located near the geometrical center of the plane. Fluid ascends on one side of the plane and descends on the opposite with small vortical structures present in the left upper corner and right lower corner. The figure is symmetric under the composition of two rotations $\Omega_h \circ \Omega_v$. The first rotation (Ω_v) is around a vertical axis passing through the center of the cavity and the second rotation Ω_h is taken around the central horizontal axis. An examination of the magnitude of the velocity in the whole volume indicates that the point with maximum velocity is located in this plane. The velocity field in the right panel of the same figure indicates that the convective pattern in plane BB' is composed of four rotating structures one in each quadrant of the rectangle. The velocity distribution displays specular symmetry with respect to the vertical and horizontal lines passing through the center of the rectangular plane, *i.e.* if the origin of Cartesian coordinates is defined at the center of the rectangle, the following relations hold,

$$u(x,y) = -u(-x,y), \quad v(x,y) = v(-x,y) \tag{5.11}$$

and

$$u(x,y) = u(x,-y), \quad v(x,y) = -v(x,-y). \tag{5.12}$$

The remarks leading to equation (5.10) indicate that there is no preferred orientation implicit in the conservation equations and boundary conditions. However, as indicated in the left panel of Figure 5.1, the solution is clearly non-axisymmetric and solutions with the same convective pattern, but different azimuthal orientations exist. The calculation procedure used in the numerical integration defines a specific orientation of the convective pattern, and for this reason we have no control on the resulting orientation of the calculated flow. It was found that the symmetries described in the flow shown in the right panel of Figure 5.1 and equation (5.11) occur only in this particular plane. Hence, this plane can be used as a reference for the definition of the orientation of the convective cell. In all other planes containing the axis of the cylinder, it was observed that the flow does not feature these symmetries but are smooth transitions from one of the two patterns in Figure 5.1 to the other.

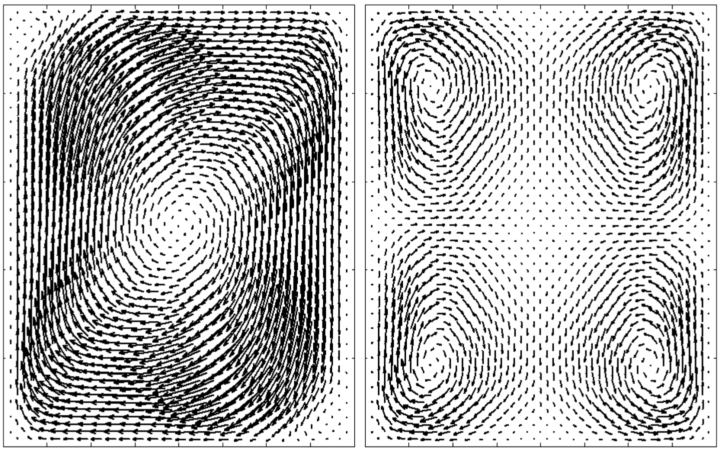

Figure 5.1: Velocity fields in two mutually perpendicular vertical planes containing the cylinder axis. Left and right panels show respectively planes AA' and BB' of Figure 5.2.

In order to give a global idea of the flow inside the cavity, we use the concept of *vortex core* as a visualization tool, calculated according to the definition of Jeong and Hussain [46] and shown in Figure 5.2. The volume contained in the vortex core indicates the region where local rotational motion dominates over strain deformation. The outline of the container and the position of planes AA' and BB'are also shown in Figure 5.2. As expected, the vortex core is not axisymmetric but displays clearly the symmetries discussed in the context of Figures 5.1.

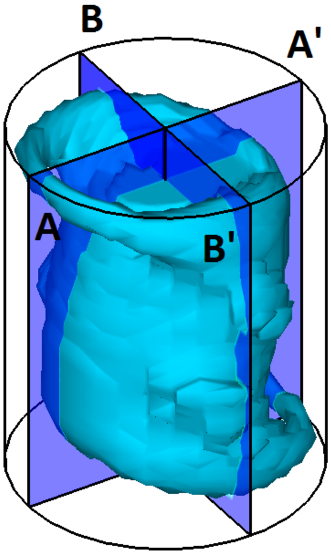

Figure 5.2: Vortex core for $Ra = 5.12 \times 10^5$.

Figure 5.3 shows the temperature fields corresponding to planes AA' and BB'. As expected, the temperature distributions are deformed by the convective motion, but in a large part of the the volume, the temperature has approximately the same value. In some experimental studies reported in the literature, the flow has been characterized by a local recording of the temperature. The temperature distribution displayed in Figure 5.3 makes it clear that the correct positioning of the temperature sensors is critical for this characterization strategy.

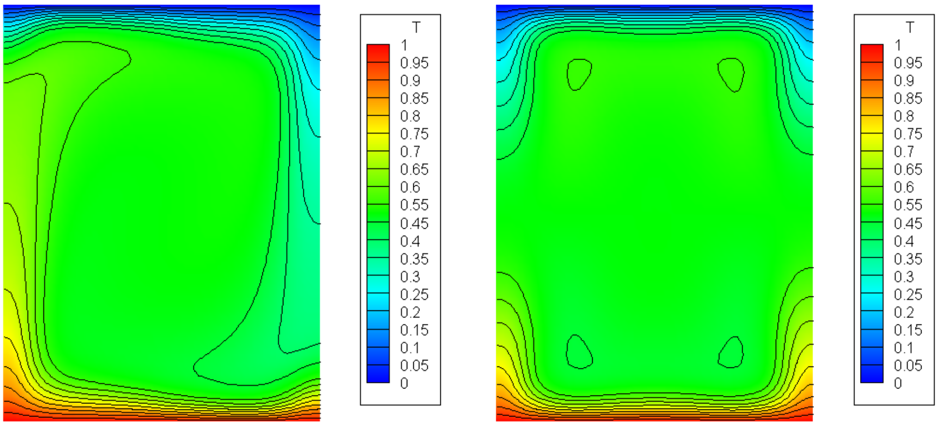

Figure 5.3: Temperature fields at planes AA'(left) and BB'(right).

Comparison with experimental data

As explained in previous sections, a cylindrical coordinate system was used for the numerical calculations, while the information from the experimental system was acquired by moving the light planes in Cartesian directions; see Figure 5.4.

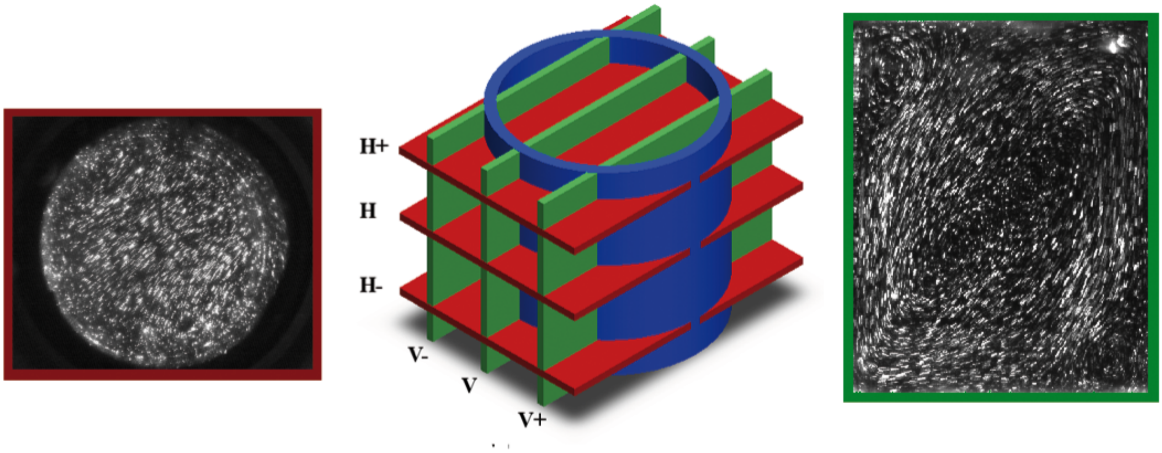

Figure 5.4: The central sketch shows the positions of the horizontal (**H**) and vertical (**V**) planes where experimental observations were made. Planes **V**$\pm$ are located at $\pm$ 4 mm from the central vertical plane, while planes **H**$\pm$ are located at $\pm$ 5 mm from the central horizontal plane. The figures on the sides are samples of the horizontal and vertical images of the tracers.

Hence, in order to compare the theoretical and experimental results, interpolations were required. Given that the density of data in the calculations is far larger than that of the experimental observations, we chose to interpolate the numerical calculations to find the velocities in the points where the experimental data were observed. We attempt to compare the projection of the velocity field on a vertical plane that contains the axis of the cylinder (plane **V** in Figure 5.4), but since the orientation of the experimentally observed plane is not known a priori, it is required to search for the best fit of the calculated velocity fields with different orientations. Even though all orientations can be calculated, we find that this is not a straightforward task since differences between calculated velocity fields and the experimentally observed velocity field are similar for a relatively wide range of orientations and it is difficult to single out the optimum orientation. However, using information from the velocity fields in the horizontal planes, the relative orientation is relatively simple to find. Figure 5.5 shows the experimental (upper row) and calculated (lower row) projection of the velocity field on the three horizontal planes, **H+**, **H** and **H-** of Figure 5.4. As can be clearly seen, the velocity fields display analogous qualitative features. The first and last velocity fields show that the flow is mostly one directional and in opposite sense from each other; the central field displays a sink at the center of the circular region.

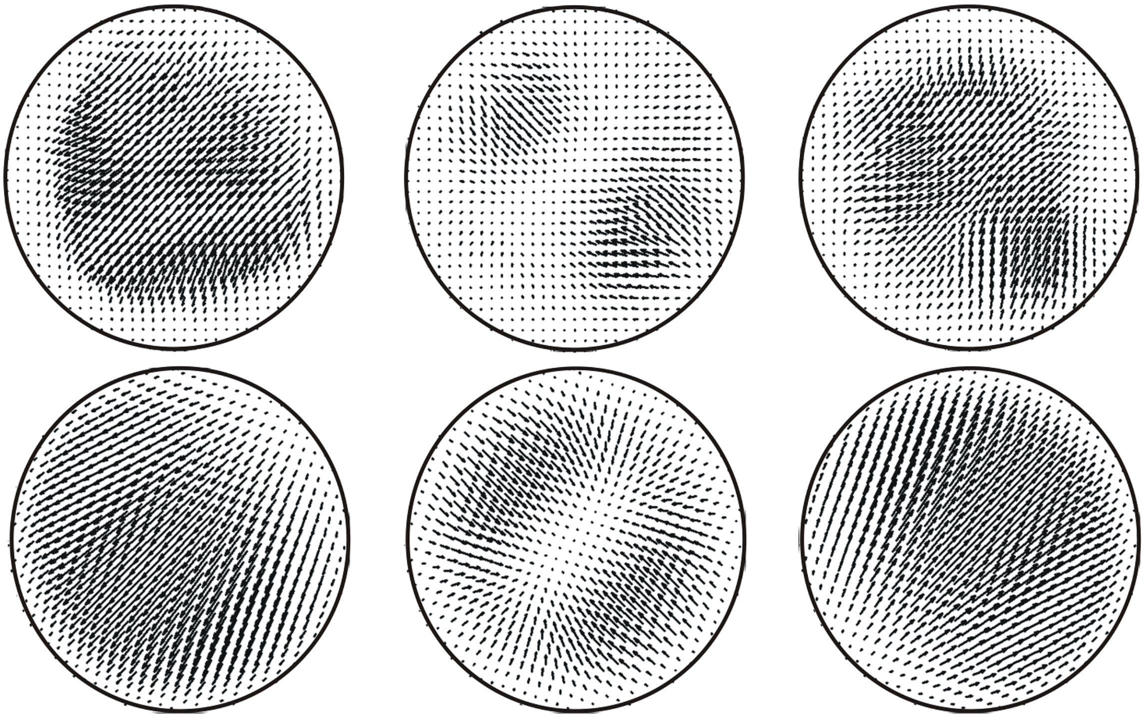

Figure 5.5: Upper row, experimental horizontal projection of the velocity field; lower row, calculated horizontal projection of the velocity field. The first, second and third columns correspond, respectively, to planes **H-**, **H** and **H+** of Figure 5.4.

Figure 5.6 shows the velocity field projections in vertical planes **V-**, **V** and **V+** of Figure 5.4. As can be appreciated, all major features of the flow are correctly captured by the numerical solution, in particular, the displacements of the center of the dominant vortex as the planes examined are moved toward (**V+**) or away (**V-**) from the observer. Another interesting feature clearly displayed in both velocity fields at position (**V**) are the two small counter-rotating cells in the upper left and lower right corners.

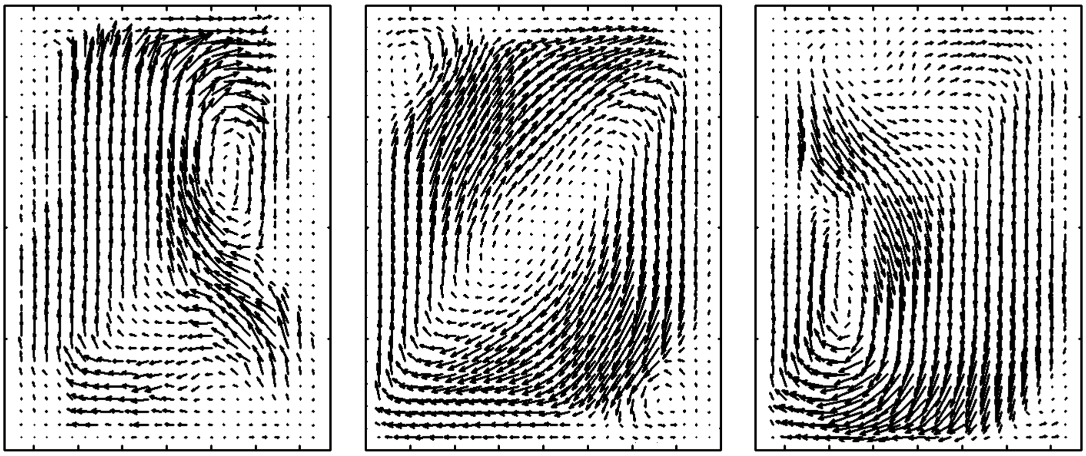

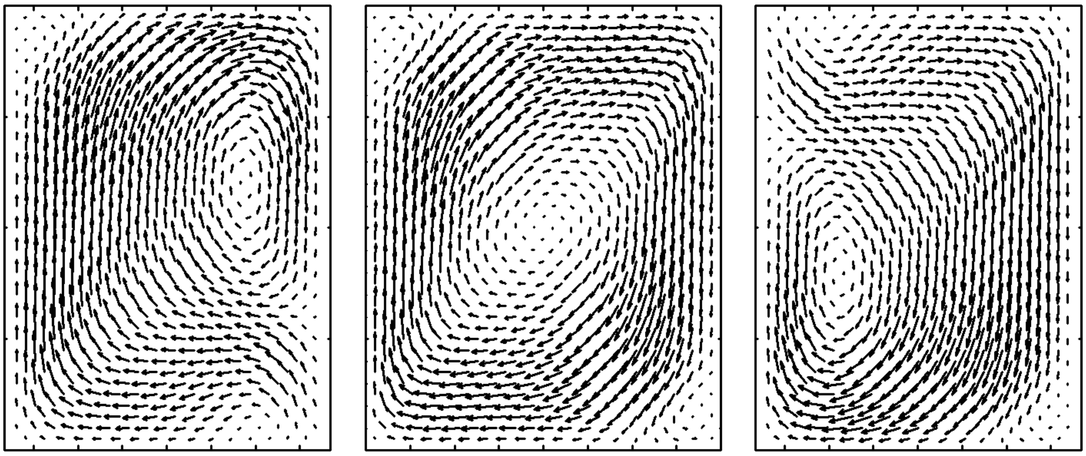

Figure 5.6: Upper row, experimental vertical projection of the velocity field; lower row, calculated vertical projection of the velocity field. The first, second and third columns correspond respectively to planes **V-**, **V** and **V+** of Figure 5.4.

In order to make a quantitative comparison, we plot the two components (u,v) of the velocity field in the vertical plane **V** (see Figure5.4) as functions of the Cartesian coordinate x, defined as the horizontal coordinate on plane **V**. The axis of coordinates is at the center of **V**. The velocity distributions are taken at $z = -5.0$ mm, $z = 0$ and $z = 5.0$ mm. In the upper row of Figure 5.7, the velocity component u is plotted as a function of x. The dots are experimental observations and the continuous lines are numerical calculations; the green and blue dots were obtained with the horizontal and vertical PIV systems, respectively. In the lower row, the velocity component v is plotted as a function of x the coordinate. The method to calculate the experimental uncertainty is described in the first paragraph of this section.

As can be appreciated in Figure 5.7, experimental observations coincide with the numerically calculated velocity profiles in most cases. It is interesting to note that the largest discrepancies between the numerical calculations and the observations are found for the green dots (horizontal PIV system) and $z = 5.0$ mm where limitations in the experimental equipment result in poor quality of the PIV images. Also, for the same reason, in this location the uncertainty bars are the largest. Figure 5.8, shows the vertical velocity (w) profiles at the plane **V** and $z = -5.0$ mm, 0 and 5.0 mm as functions of x. At the center of the cavity, where the velocity is larger, the observed and calculated profiles coincides quantitatively. Above and below these positions, although there is a qualitative coincidence, the calculated profiles underestimate the observed velocities in some intervals.

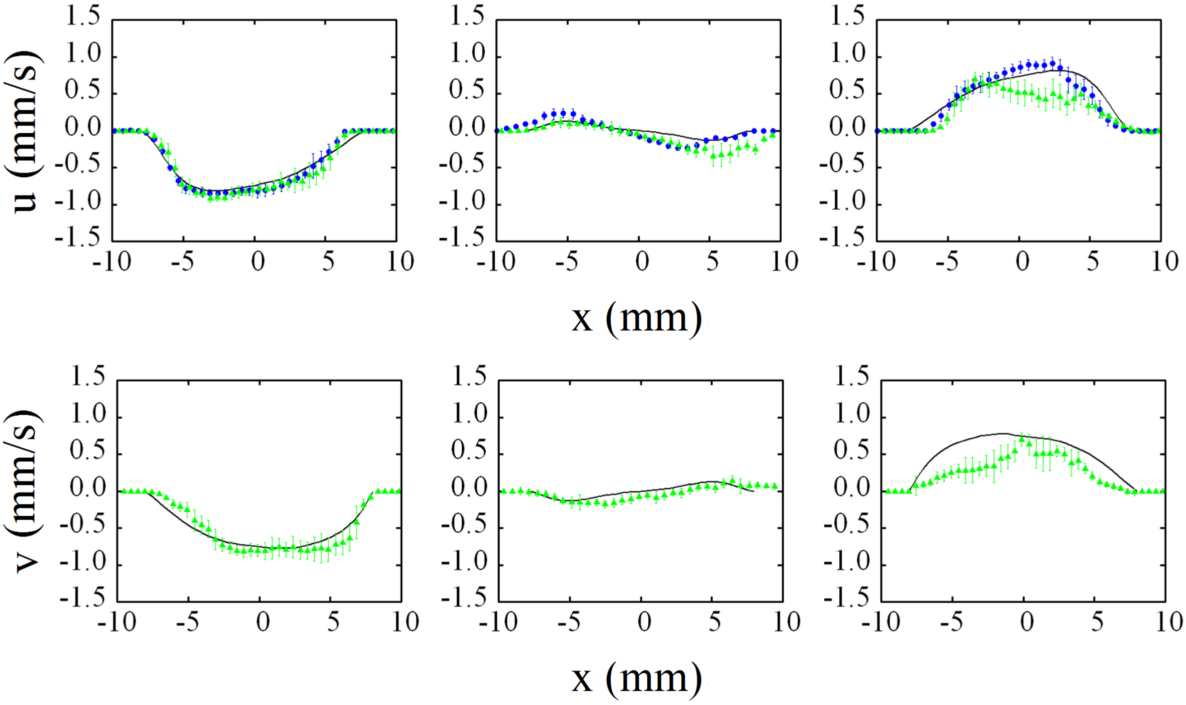

Figure 5.7: Upper row: x-velocity component (u) as a function of x. Left, $z = -5.0$ mm, center $z = 0$ right $z = 5.0$ mm. The continuous lines are numerical calculations and the dots are experimental observations. Green and blue dots are data obtained with the horizontal and vertical PIV systems respectively. Lower row: y-velocity component (v) as a function of x for the same vertical locations as in the upper line.

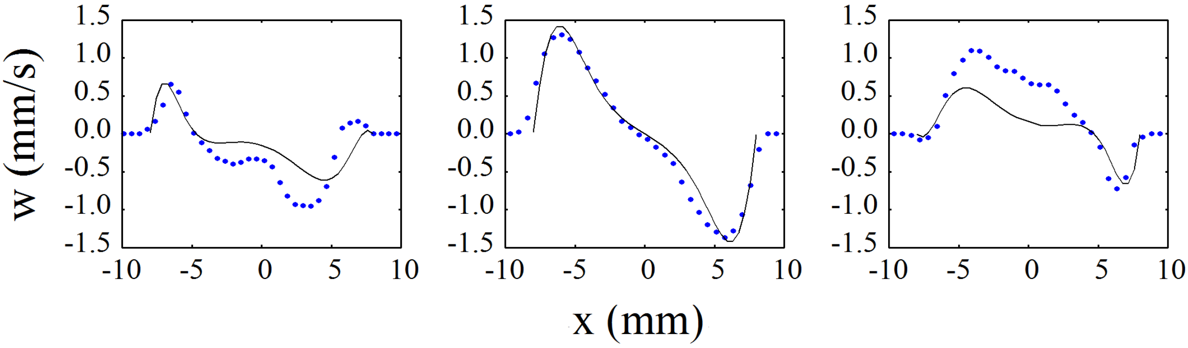

Figure 5.8: Numerical and experimental w velocity component in the central vertical plane as a function of x at $z = -5.0$ mm (left), $z = 0$ (center) $z = 5.0$ mm (right).

5.3.2 Time dependent flow

The results presented in this section correspond to the unsteady flow occurring at $Ra = 1.53 \times 10^6$. Given the time-dependent nature of this flow, it was not possible to explore more than one vertical plane with the present experimental equipment. Also, no attempt was made to resolve the dynamics of the flow since the time resolution of the cameras was not fast enough to record the flow evolution. In addition, memory limitations in our equipment did not allow us to capture more than 300 subsequent images. We obtained time average velocity fields using 1760 vector fields which correspond to 540 s long observations. The numerical calculations indicate that the flow is periodic with an approximate characteristic time of 9 s and although the detailed time evolution of the flow does not coincide with experimental records, we could compare theoretical and experimental averaged velocity fields.

The dominant averaged convective structure observed is a single convective cell, similar to that observed in the steady state flow with two small counter rotating cells at the upper left and lower right corners, see Figure 5.9 left. The corresponding numerical simulation displays the same features as can be appreciated from Figure 5.9 right.

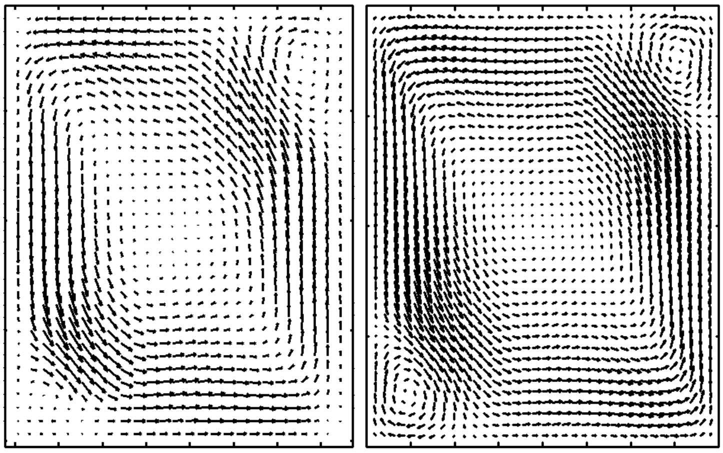

Figure 5.9: Averaged experimental (left) and numerical (right) velocity field at the central vertical plane. $Ra = 1.53 \times 10^6$.

Quantitative comparisons of the velocity profiles have been made using the same geometrical nomenclature and definitions of Section 5.3.1. Figure 5.10 shows experimental and numerical results of(u) and (w) at $z = -5.0$ mm, $z = 0$ and $z = 5.0$ mm.

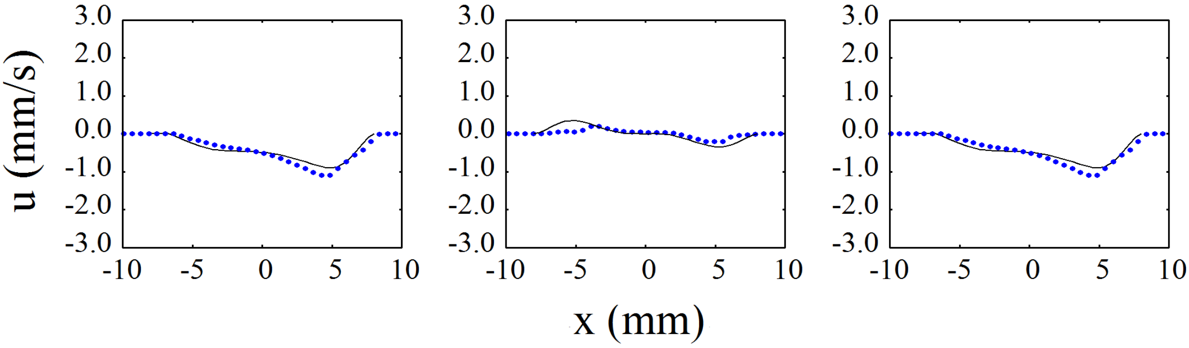

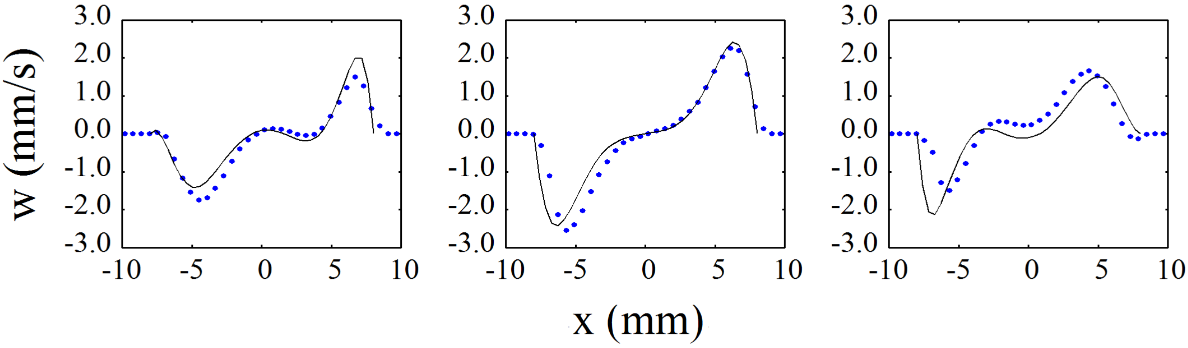

Figure 5.10: Upper row, average x-velocity (u) as a function of the horizontal coordinate x. Lower row, average z-velocity (w) as a function of the horizontal coordinate x. Left column, $z = 5.0$ mm, center column, $z = 0$, right column $z = -5.0$ mm. $Ra = 1.53 \times 10^6$.

As observed in Figure 5.10, the qualitative behavior calculated with the numerical model agrees with the corresponding experimental data in all cases. Also, the quantitative differences are small in most cases, particularly for the vertical component of the velocity where the signal to noise ratio is largest.

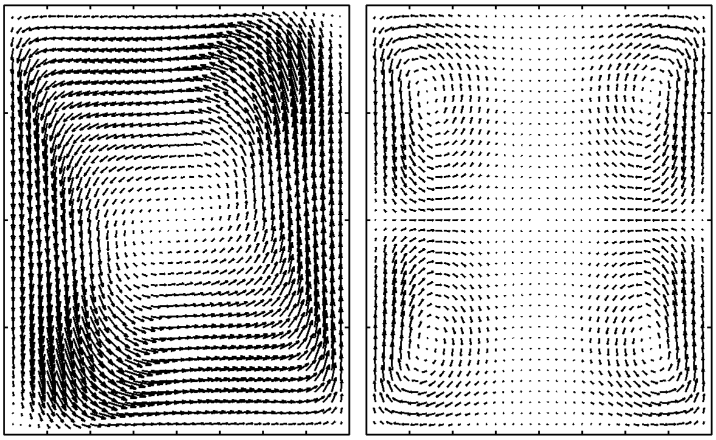

Figure 5.11: Averaged velocity fields for $Ra = 1.53 \times 10^6$ in two mutually perpendicular planes. The structures are similar to those obtained in steady state, see Figure 5.1.

Given the close similarity of the flow patterns in steady state and averaged time dependent conditions, it is interesting to explore whether a four circulating structure like the one observed in Figure 5.1, can be identified in the (averaged) time-dependent flow, if the orientation is correctly chosen. Figure 5.11 shows the calculated velocity fields for the equivalent AA' and BB' planes of Figure 5.1, demonstrating that this is indeed the case. Note however that for the averaged, time-dependent flow, the centers of the rotating structures are closer to the lateral walls as compared with the steady state case.

5.4 Discussion and Conclusions

Experimental and numerical investigations of steady and time-dependent natural convection in a slender cylindrical cavity filled with water and heated from below are reported. Steady and time-dependent flows were considered. We have followed the verification and validation methodology [2] to test adequacy of the physical model and numerical solution.

As a further verification of the numerical calculations, we solved the governing equations with a spectral method using Fourier-Galerkin for the azimuthal coordinate and Chebyshev polynomials for the radial an axial coordinates; we used a projection method for pressure decoupling [15]. Both methodologies gave equivalent results for the steady convective flow in the cylinder. We conclude that our results are verified and given that the finite volume method is a simpler methodology, we used it for obtaining the results presented in this report. Since the numerical solution is independent of the mesh and two different discretization methods give coincident results, the numerical solution was considered to be verified.

Although studies of flows similar to the one studied here are available in the literature, there have been very few attempts at detailed comparison between experimental observations and calculations from numerical simulations for natural convection flows. The present study contains such a comparison for a particular aspect ratio and range of Rayleigh numbers. In the context of numerical model credibility, this procedure constitutes the validation. It is interesting to note that a particular difficulty of the analysis of the flow explored here is the fact that the azimuthal orientation of the experimentally observed non-axisymmetric convective cell is not known. We solved this problem by simultaneously recording the velocity in horizontal and vertical planes. We conclude that the qualitative features of the observed flow are correctly modeled by the numerical solution and that in many specific comparisons, a quantitative agreement has been found. In turn, the numerical solution gives valuable information on flow features not directly observed.

---

[2] According to [47] *verification* is guaranteeing that the results obtained with an approximate numerical integration are independent of the method of integration used. *validation* is the comparison of the results of the numerical model and the experimental observations to determine the range of parameters for which the comparison is satisfactory.

Chapter 6

The effect of rotation on the natural convective flow in a cylindrical container

Consider a fluid in rotation about some fixed axis with a constant angular velocity ω. In many important examples, it is convenient to describe its motion as it appears to an observer at rest in a frame rotating about the same axis and with the same angular velocity. For example, this would be the case in many physical situations found in geophysical flows, like for instance, the analyses in the β plane [48]. Also, many industrial applications involving rotating machinery are better described in a frame of reference rotating with the system. In the present study, the most important application is the potential improvement of the crystals grown in rotating crucibles as described by that we have in mind is the natural convective flow in crucibles.

The establishment of the balance equations in a rotating frame of reference is due to Laplace who was interested in describing the formation of the solar system. According to Laplace's description of the hypothesis, the solar system had evolved from a globular mass of incandescent gas rotating around an axis through its center of mass [49], and Coriolis [50] who developed the mathematical theory of rotating engines. A modern account of the theory which includes a careful and detailed development of the equations from first principles can be found in [38].

The phenomenon of natural convection in a rotating frame depends fundamentally on the relative orientation and position of three vectors, the gravity acceleration vector, the rotation vector, and the temperature gradient vector, which indicates the direction of the temperature difference imposed in the system. By and large, the situation that has been analyzed in more thoroughly is when all three vectors are in the same direction (parallel or anti-parallel) since this configuration corresponds to local geophysical conditions; specifically, flows in the β plane. Important references in this area are Greenspan [51] and Koschmieder [1]. Another situation which has received much less attention in the literature, but one which is of interest here is when the (generalized) gravity acceleration vector and the temperature gradient are parallel, but the rotation vector is perpendicular to them. This situation coincides with that occurring when a natural convective flow takes place in a centrifuge. The generalized gravity acceleration is the vector sum of the gravity and the centrifugal acceleration vectors. Figure 6.1 shows a sketch of the two sets of vector orientations described in the previous paragraphs.

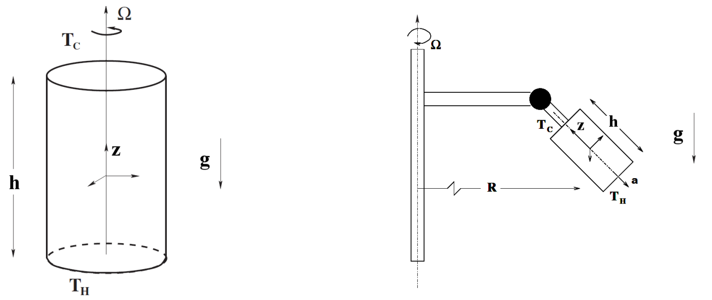

Figure 6.1: Left: Configuration where the gravity, rotation and temperature gradient are parallel. Right: Configuration where temperature gradient and effective gravity are parallel to each other but the rotation vector has a component perpendicular to this two vectors.

Regardless of the relative orientation of the rotation, gravity and temperature gradient vectors, the expression for momentum conservation in a rotating frame of reference includes terms that arise from the fact that the axis of coordinates rotates. These terms are known as the centrifugal and Coriolis accelerations. The centrifugal acceleration is proportional to the product of the angular velocity and the distance to the center of rotation and as is well known, it can be expressed as a gradient. This term can be interpreted as a pseudo pressure in the same sense as it is done with the terrestrial gravity, thus the name generalized gravity. The Coriolis acceleration which incidentally was originally deduced by Laplace, is proportional to the local velocity and is entirely new effect.

In many important cases, the study of natural convective flows is made using the Boussinesq approximation which assumes that all physical properties of the working fluid are constant except for the density in the buoyancy term. The validity of this approximation for a non-rotating natural convective flow was discussed in references [52] and [53].

6.0.1 The equations of natural convection in a rotating frame of reference

In a rotating fluid, the Boussinesq approximation has a slightly different interpretation. For the case when all three vectors are parallel, Lopez et al [52] indicate that the density should be considered constant in the centrifugal term, but variable in the Coriolis term. A more quantitative treatment of the ranges of validity of the Boussinesq approximation for rotating flows where the important fact that the base flow is not zero velocity, can be found in [53]

In the rotating frame of reference, the governing equations are

$$\frac{\partial \vec{u}}{\partial t} + (\vec{u} \cdot \nabla)\, \vec{u} = -\nabla p/\rho_0 + \nu \nabla^2 \vec{u} + \beta T \vec{g} - 2\vec{\omega} \times \vec{u} \tag{6.1}$$

$$\frac{\partial T}{\partial t} + (\vec{u} \cdot \nabla)\, T = \alpha \nabla^2 T \tag{6.2}$$

where $\vec{u}$ is the velocity field $T = T^* - T_0$ is the temperature deviation with respect to the mean temperature T_0, p is the pressure which incorporates the hydrostatic pressure due to the gravitational and centrifugal forces, g is the gravitational acceleration, β is the coefficient of volume expansion, ν is the kinematic viscosity, and α is the thermal diffusivity. The term $2\vec{\omega} \times \vec{u}$ in this equation represents the Coriolis acceleration. To describe fluid motion in this system we must add a fictitious force to the Navier Stokes equations the Coriolis force from its definition it is seen that the Coriolis force occurs only if the system is in motion and therefore has an influence only under dynamic conditions.

The system is nondimensionalized using the same scales definitions as in chapter I, (see section 1.3) , here the magnitude of angular velocity ω is included. For natural convection under the influence of rotation the governing equations in dimensionless form are

$$\nabla \cdot \vec{u} = 0 \tag{6.3}$$

$$\frac{\partial \vec{u}}{\partial t} + (\vec{u} \cdot \nabla)\,\vec{u} = -\nabla p + \left(\frac{Pr}{Ra}\right)^{\frac{1}{2}} \nabla^2 \vec{u} + T\hat{e}_z - 2\Omega \left(\frac{Pr}{Ra}\right)^{\frac{1}{2}} \hat{\omega} \times \vec{u} \tag{6.4}$$

$$\frac{\partial T}{\partial t} + (\vec{u} \cdot \nabla)\,T = \left(\frac{1}{PrRa}\right)^{\frac{1}{2}} \nabla^2 T. \tag{6.5}$$

The dimensionless boundary conditions on the temperature and velocity are written as:

$$T = 0, \quad \text{for} \quad (r, \theta, 1, t) \tag{6.6}$$

$$T = 1, \quad \text{for} \quad (r, \theta, 0, t) \tag{6.7}$$

$$\frac{\partial T}{\partial r} = 0 \quad \text{for} \quad (A, \theta, 0 < z < 1, t) \tag{6.8}$$

and

$$\vec{u} = 0 \quad \text{on all boundaries, at all times} \tag{6.9}$$

Where A Where $A = h/2D$. There are four non-dimensional parameters

Rayleigh number:	$Ra = \beta g L^3 \Delta T / \alpha\nu$
Prandtl number:	$Pr = \nu/\alpha$
Coriolis number:	$\Omega = \omega L^2/\nu$
Aspect ratio:	$\gamma = r_0/L$

The effect of rotation on natural convection introduces a number of new elements into the problem and therefore a new group of dimensionless parameters. In this study we kept fixed the aspect ratio, the Rayleigh and the Prandtl number, we only explore the effect of the variations in the Coriolis number.

6.1 Results

In this section we study natural convection in a vertical cylinder heated from below in a system in a rotating frame of reference. Numerical solutions are obtained using finite volume method. We applied the same methodology as described in section 5.2, with the Coriolis force added as an explicit term in the the numerical integration of the Navier-Stokes equations.

6.1.1 Steady state flow

In the present study we assume that the rotation vector and the gravity vector are perpendicular to each other, and since the gravity vector runs along the z-axis we choose the angular velocity vector along the x-axis. In cylindrical coordinates

$$\hat{x} = \cos\theta\,\hat{\rho} - \operatorname{sen}\theta\,\hat{\theta}. \tag{6.10}$$

Inspection of the governing equations (equations 6.3 to 6.5) and boundary conditions (expressions 6.6 to 6.8) indicate that for $\Omega = 0$, the system has angular symmetry: These rotations generate the symmetry group O(2) it can be concluded that the solution is infinitely degenerate.

However, for $\Omega \neq 0$, the symmetry is broken and the system is not degenerate since there is an externally imposed specific orientation, namely, the orientation of the rotation vector in the rotating frame of reference. Given that frequently the symmetries lead to instabilities, in this sense, the rotation stabilizes the flow. As will be indicated below this is the case even for small but finite rotations. Note that this geometrical configuration corresponds to that of a cylinder rotating at the extreme of an arm o a centrifuge (see the right panel figure 6.1 and references [54]).

In all examples presented, we consider a cylindrical container of aspect ratio 1.25 filled with water $Pr = 6.67$, heated from below and cooled from above. In order to analyze the effect of rotation we fix the Rayleigh number at such $Ra = 5.12 \times 10^5$ and make a parametric study considering the angular velocity ω =0.01, 0.1, 1, and 10, the corresponding Coriolis numbers are $\Omega = 4.167, 416.7, \text{and } 4167$.

The left panel of the upper line in figure 6.2 obtain with no rotation shows that the dominant flow pattern in plane AA' is a convective cell rotating clockwise with its center defined by the point of vanishing velocity located near the geometrical center of the plane. Fluid ascends on one side of the plane and descends on the opposite with small vortical structures present in the left upper corner and right lower corner. The velocity field in the right panel of the same figure indicates that the convective pattern in plane BB' is composed of four rotating structures one in each quadrant of the rectangle. At low rotation rates $\omega = 0.01$, $\Omega = 4.167$ the flow is indistinguishable from the structure of obtain with no rotation as can be appreciate from the second line in figure 6.2.

Although the flow patterns are the same there is a major different between the two solutions in the no rotating case the solutions is infinity degenerate while in the rotating case the orientation is fix.

At high rotation rates ($\omega = 10, \Omega = 4167$) there is only one single convective cell, since the vortical structures on the corners have disappeared. Also dramatic changes are observed in the plane BB' where no rotating structures are present. These flow patterns in the bottom line of figure 6.2.

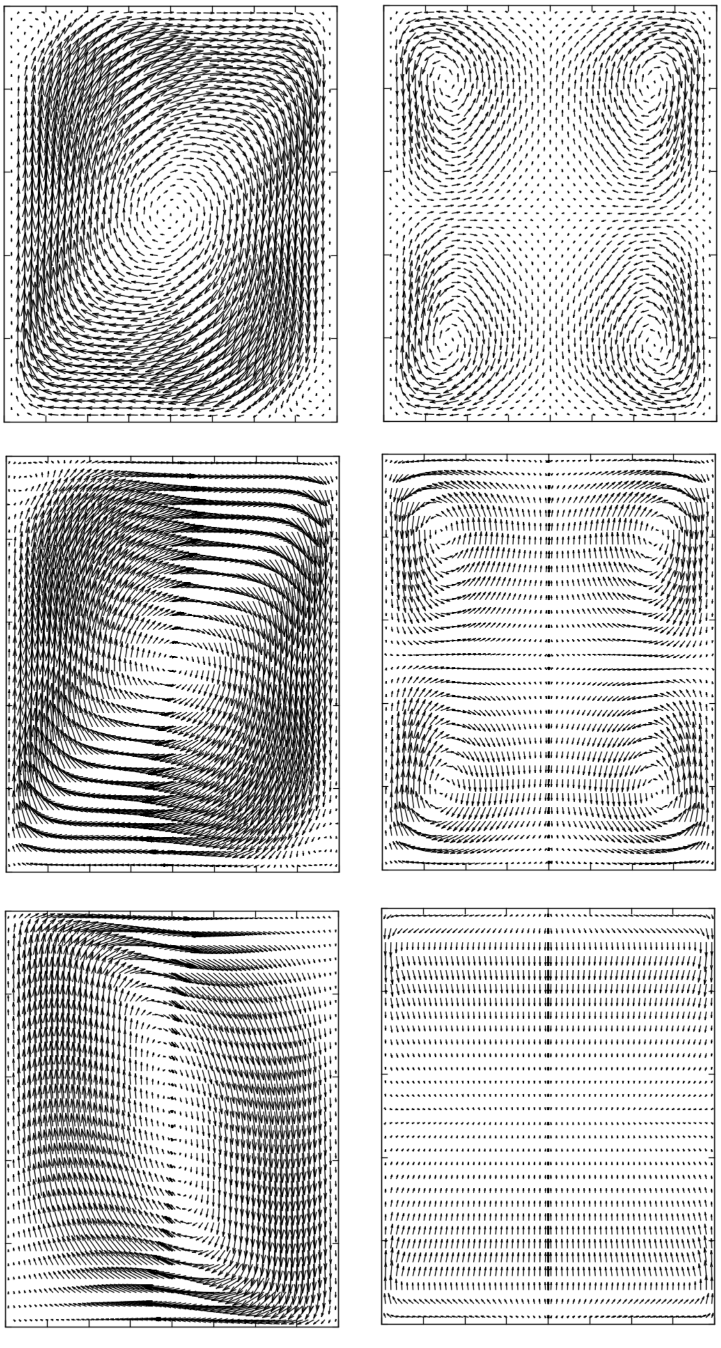

Figure 6.2: Upper line: Velocity field in the AA' (left) and BB' (right) for $Ra = 5.12 \times 10^5$

and $\Omega = 0$. Center line: Velocity field in the AA' (left) and BB' (right) for $Ra = 5.12 \times 10^5$ and $\Omega = 4.167$. Bottom line: Velocity field in the AA' (left) and BB' (right) for $Ra = 5.12 \times 10^5$ and $\Omega = 4167$.

Shape transitions when the rotation in the flow is increased are evident in the vortex core [46] of the flow. In figure 6.3 the vortex cores corresponding to cases $\Omega = 0$, $\Omega = 4.167$, $\Omega = 416.7$ and $\Omega = 4167$ are shown. For low rotation rates the flow has a similar structure as the non rotating case. For high rotation rates the influence of rotation is clearly seem in a reduction of the region occupied by main vortex core of the flow.

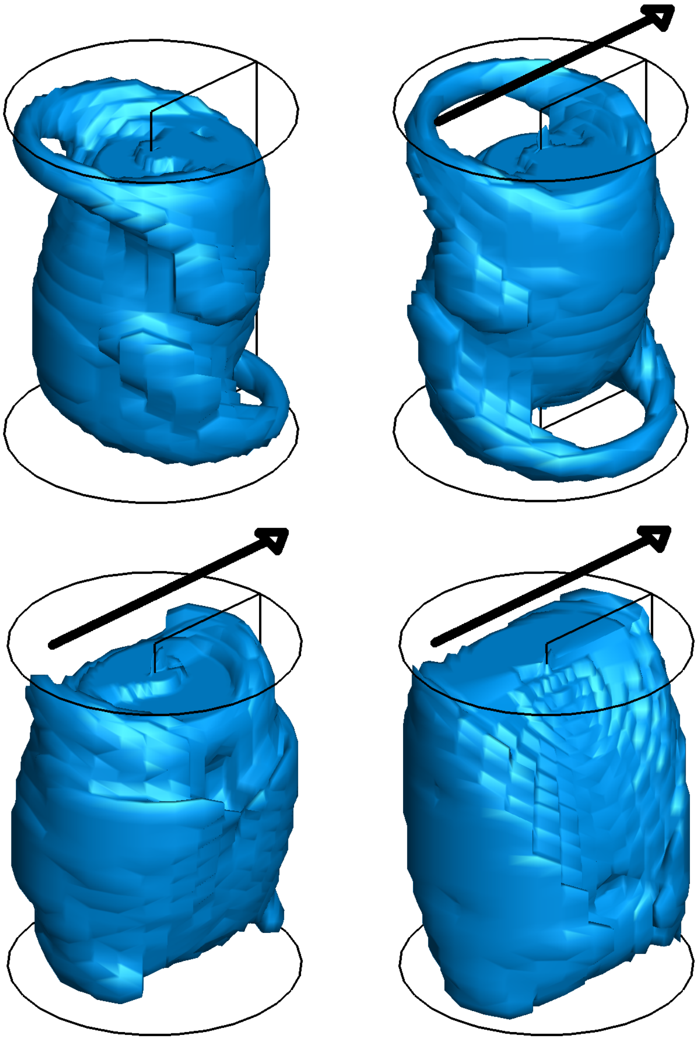

Figure 6.3: Vortex cores of the flow at $\Omega = 0$, $\Omega = 4.167$ and $\Omega = 4167$ in all case $Ra = 5.12 \times 10^5$. The bold arrow represent the position of the position vector note that the distance form the rotation axis to the cylinder has been greatly reduce for drawing purpose.

The relative orientation of the convective cell with respect to the rotation vector is also illustrated in figure 6.3.

6.1.2 Time dependent flow

One of the main objectives of the present study is to clarify the dynamic changes generated on the qualitative behavior of the flow by the rotation. The most notable effect is that at a fixed Rayleigh number a non rotating time dependent flow becomes steady when it rotates at a large angular velocity. In order to illustrate this observation we plot in figure 6.4 the z-component of the velocity at the point (A/2,π,1/2) as function of the time for a rotating and a non-rotating flow at a Rayleigh number $Ra = 1.5 \times 10^6$. As is it clearly observed in the non rotating case the velocity reflects an oscillatory behavior with an amplitude of 0.047. In contrast, where the cylinder is rotating, the initial oscillatory is transient and dies away at approximately 150 dimensionless time.

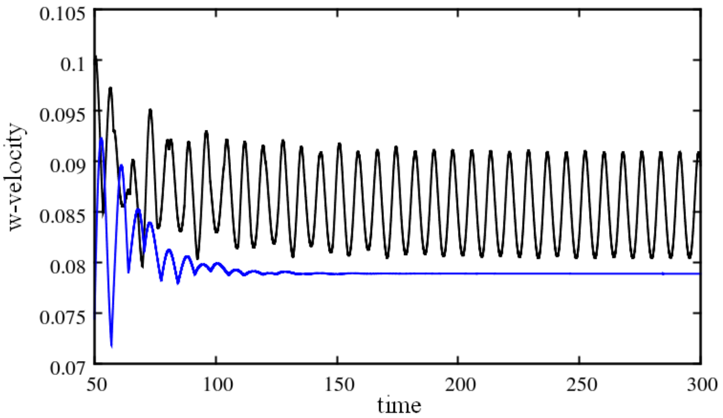

Figure 6.4: Time evolution of the flow with ($\omega = 10$, blue line) and without ($\omega = 0$, black line) the effect of rotation. $Ra = 1.5 \times 10^6$

The next issue that arises naturally from the observation described in the previous paragraph is the following: given a fixed Rayleigh number, which is the minimum angular velocity to suppress the oscillation that occurs in the non-rotating case?. In figure 6.5 we show the information required to answer this question for $Ra = 1.5 \times 10^6$. In this figure the amplitude of the oscillation is plotted as a function of the Coriolis number.

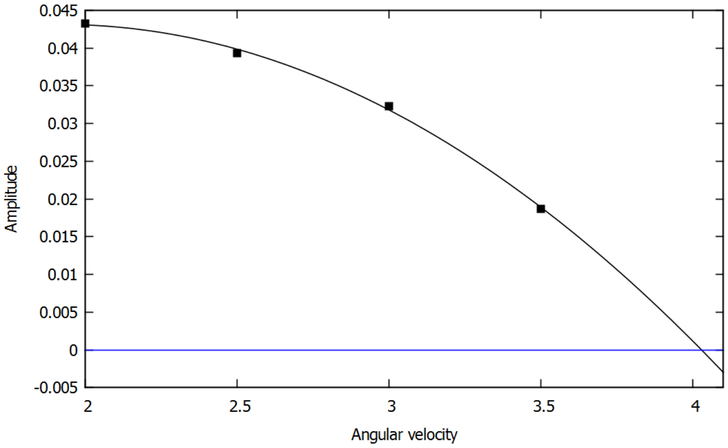

Figure 6.5: Amplitude vs angular velocity

The qualitative behavior indicates a monotonous decreasing function and a quadratic polynomial fit indicates that $\omega = 4.0278$ ($\Omega = 1678.2$) results in zero amplitude of the oscillation. The minimum Coriolis number required to turn the time dependent motion in to a steady state is defined as the critical Coriolis number.

The critical Coriolis number as a function of the Rayleigh number for an aspect ratio of 1.25 is plotted in figure 6.6

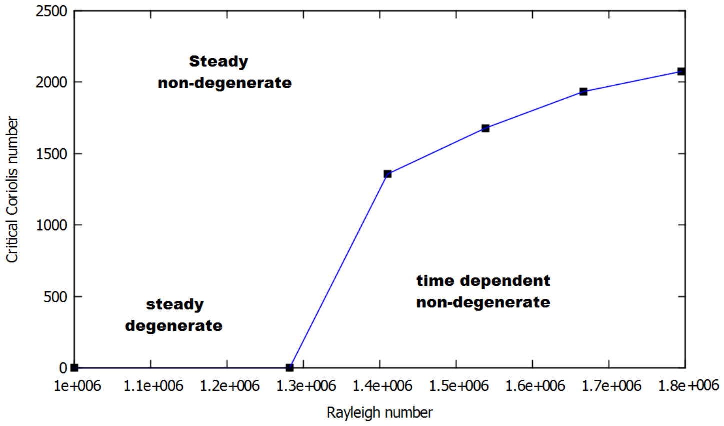

Figure 6.6: Rayleigh number vs angular velocity

Flows with Rayleigh numbers small than $1.28e{+}6$ and zero Coriolis number are degenerate steady flows. The same range of Rayleigh numbers that for finite Coriolis numbers are also steady, that not degenerate since the convective cell orientation is fixed by the position of rotation vector.

For $Ra > 1.28e + 6$ the flows are time dependent or steady depending on the Coriolis number. The trace of the critical Coriolis number as function of the Rayleigh number is non-linear as indicated in figure 6.6 .

Chapter 7

The effect of electromagnetic forces on the natural convective flow in a cylindrical container

In this chapter we briefly analyze the effect of an externally imposed magnetic field on the natural convective flow in a cylinder filled with an electrically conducting fluid. This is an example of how the numerical tools developed in this work can be used to study other physical systems of interest.

A general discussion of the effect of a magnetic field on the natural convection motion can be found in Chandrasekhar [38]. Informative references of similar flows are [55] and [56].

The analysis of the interaction of fluid motion of electrically conducting fluids with magnetic fields is called magnetohydrodynamics (MHD). In this subfield of physics fluid dynamics an electromagnetism are combined. Authoritative treatises on the subject are [57] and [58]. Here we just present the basis concepts required to illustrate the usefulness of the numerical tools to describe MHD flows.

If it can be assumed that in the flow of interest, the characteristic velocity is much smaller than the velocity of light, the time changes of the magnetic field are of low frequency and that the electric fields are of the order of the electromotive force induced by the motion of the fluid, then the accumulation or redistribution of electric charges can be neglected. This major simplification that renders the problem tractable is what is known the magnetohydrodynamic approximation.

The task is to solve the Maxwell equations coupled with the conservation equations of non isothermal fluid dynamics, where the body force on the fluid, called the Lorentz force term is

$$\vec{f} = \vec{j} \times \vec{B}$$

where $\vec{j}$ is the electric current and $\vec{B}$ is the magnetic field.

The magnetic field can be interpreted as the sum of the external magnetic field $\vec{B}_0$ and the induced field $\vec{b}$. In general, it can be stated that the magnetic field propagates due to convection and diffusion. When diffusion is the dominant effect, the induced magnetic field is negligible compared to the externally imposed field, and in this case, the magnetic field is not an unknown in the problem anymore.

One of these formulations uses the scalar electric potential ϕ. Using the inductionless approximation the electric field can be treated as potential and expressed in terms of the electric potential, such that $\vec{E} = -\nabla\phi$. This formulation is very common in the literature of MHD flows [59], [55].

For natural convection under the influence of a constant magnetic field, the governing equations (using a magnetohydrodynamic approximation) in dimensionless form are

$$\nabla \cdot \vec{u} = 0 \tag{7.1}$$

$$\frac{\partial \vec{u}}{\partial t} + (\vec{u} \cdot \nabla)\,\vec{u} = -\nabla p + \left(\frac{Pr}{Ra}\right)^{\frac{1}{2}} \nabla^2 \vec{u} + T\hat{e}_z + Ha^2 \left(\frac{Pr}{Ra}\right)^{\frac{1}{2}} \vec{j} \times \vec{B}_0 \tag{7.2}$$

$$\frac{\partial T}{\partial t} + (\vec{u} \cdot \nabla)\,T = \left(\frac{1}{PrRa}\right)^{\frac{1}{2}} \nabla^2 T. \tag{7.3}$$

$$\nabla^2 \phi = \vec{B}_0 \cdot \nabla \times \vec{u} \tag{7.4}$$

$$\vec{j} = -\nabla\phi + \vec{u} \times \vec{B}_0 \tag{7.5}$$

As a specific example consider the case where the magnetic field is parallel to the axis of the cylinder as shown in figure 7.1

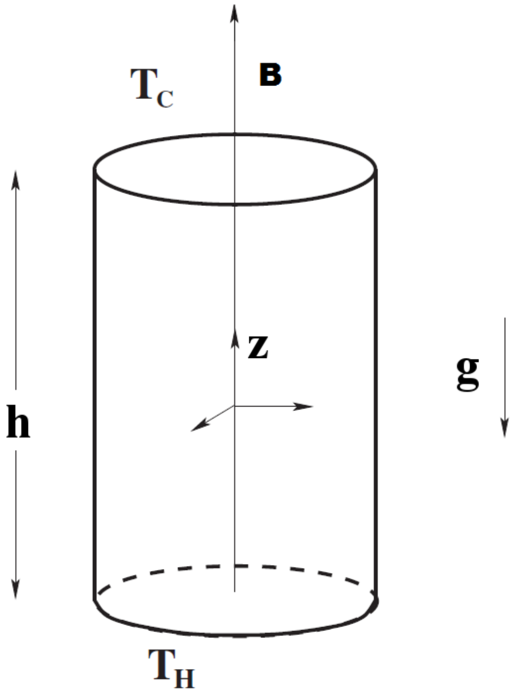

Figure 7.1: Configuration where the gravity, magnetic field and temperature gradient are parallel.

The dimensionless boundary conditions on the temperature the velocity and the electric potential are written as:

$$T = 0, \quad \text{for} \quad (r, \theta, 1, t) \tag{7.6}$$

$$T = 1, \quad \text{for} \quad (r, \theta, 0, t) \tag{7.7}$$

$$\frac{\partial T}{\partial r} = 0 \quad \text{for} \quad (A, \theta, 0 < z < 1, t) \tag{7.8}$$

$$\frac{\partial \phi}{\partial n} = 0, \quad \text{on all boundaries} \tag{7.9}$$

and

$$\vec{u} = 0 \quad \text{on all boundaries} \tag{7.10}$$

Where $A = h/2D$ and the equations are nondimensionalized using the same scales definitions as in chapter I, (see section 1.3), adding the magnitude of the external magnetic field B_0, and a characteristic electrical potential $\phi_0 = u_c B_0 L$. The new dimensionless parameter is the Hartmann number defined as $Ha = B_0 L\sqrt{\sigma/\rho\nu}$ which is the ratio of electromagnetic forces and viscous effects.

The governing equations 7.1 - 7.1 and boundary conditions 7.6 - 7.10 are invariant under arbitrary rotations about the axis of the cylinder. If R_ψ is a rotation of angle ψ around the z-axis, its action is

$$R_\psi(u, v, w, T, p, \phi)(r, \theta, z) = (u, v, w, T, p, \phi)(r, \theta + \psi, z). \tag{7.11}$$

This property indicates that if a solution is obtained, the same velocity, pressure, electric potential and temperature fields with a different orientation with respect to the vertical axis, constitute also a solution. These rotations generate the symmetry group O(2).

Numerical solutions are obtained using finite volume method. We applied the same methodology as described in section 5.2, with the Lorentz force added as an explicit term in the the numerical integration of the Navier-Stokes equations.

7.1 Results

We shall study the effect of Hartmann number, considering to cases. In the firs case we fix $Ra = 5.5 \times 10^5$ which corresponds to a steady state in the absence of magnetic field. In the second case we explore the MHD effects on a time dependent flow with a $Ra = 1.5 \times 10^6$.

7.1.1 Steady state flow

We consider a cylindrical container of aspect ratio 1.25 filled with water $Pr = 6.67$, heated from below and cooled from above. The Rayleigh number is $Ra = 5.5 \times 10^5$.

In figure 7.2 the vortex core of the flow for Hartmann numbers Ha =0, 10, 20 and 30 is shown

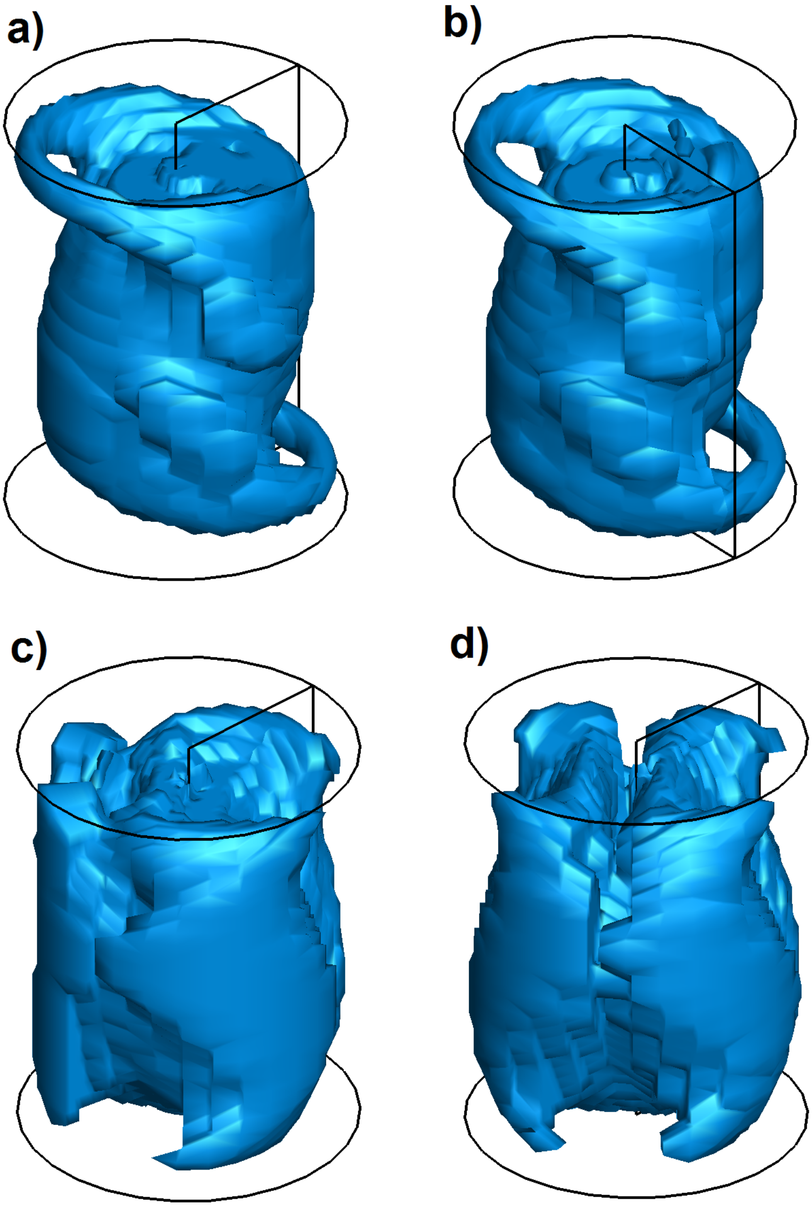

Figure 7.2: Evolution of the vortex core of the flow. a) Ha=0 (left top), b) Ha=10 (right top), c) Ha=20(left bottom) and d) Ha=30 (right bottom). $Ra = 5.5 \times 10^5$

For low Hartmann numbers $Ha < 10$ the electromagnetic force leads to insignificant modifications on the flow, but the flow pattern obtained is oriented different direction due to the degeneration on the solution brought about by the symmetries of the flow (see equation 7.11).

As discussed in section 5.3.1 the vortex core indicates that the dominant structure is a non-axisymmetric convective cell with two minor structure near the horizontal walls. The vortex core for the case Ha=10 is qualitatively the same and topologically equivalent, convective cells are slightly pushed towards the lateral walls.

At a high Hartmann number $Ha = 20$ the vortex core is noticeably displaced to the regions near to the lateral wall indicating that the convective cells are pushed further towards this wall. It is found that the flow patterns is symmetric with respect to a vertical plane which is interpreted as the reminiscence of the plane AA' but the vertical-azimuthal symmetry composition of the non- MHD case is lost (see section 5.3.1).

For the highest Hartmann explored $Ha = 30$ (see figure 7.2), the vortex core display a four lobe structure approximately symmetric with respect to two mutually perpendicular vertical planes. An interesting observation is that the vortex core is composed of four column-shaped structures.

Figure 7.3 shows the distribution of the vertical velocity at the mid-height of the cylinder for Ha=0, 10, 20 y 30. The plot corroborate the geometrical properties presented in the discussion of figure 7.2. For Ha=20 and Ha=30 lines are drown to emphasize the symmetries. It interesting to note the columnar geometry of the ascendant/descendant flow in the case of the largest Hartmann number.

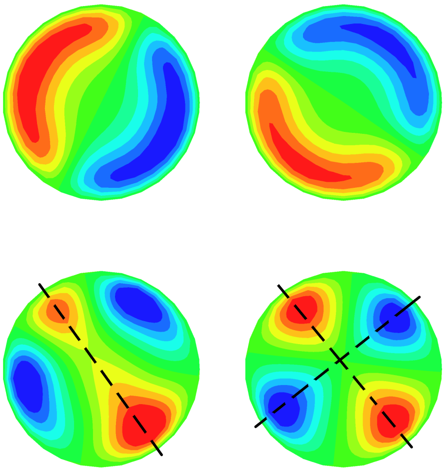

Figure 7.3: Color map of the w velocity at the center of the cylinder. a) Ha=0 (left top), b) Ha=10 (right top) c), Ha=20(left bottom) and d) Ha=30 (right bottom). $Ra = 5.5 \times 10^5$

The two dimensional velocity fields corresponding to cases Ha=0 and Ha=30 are shown int figure 7.4 to highlight the effect of the magnetic field on the flow. The orientation of the vertical planes shown in the previous figure 7.3 d) correspond to the velocity fields in the lower row of figure 7.4.

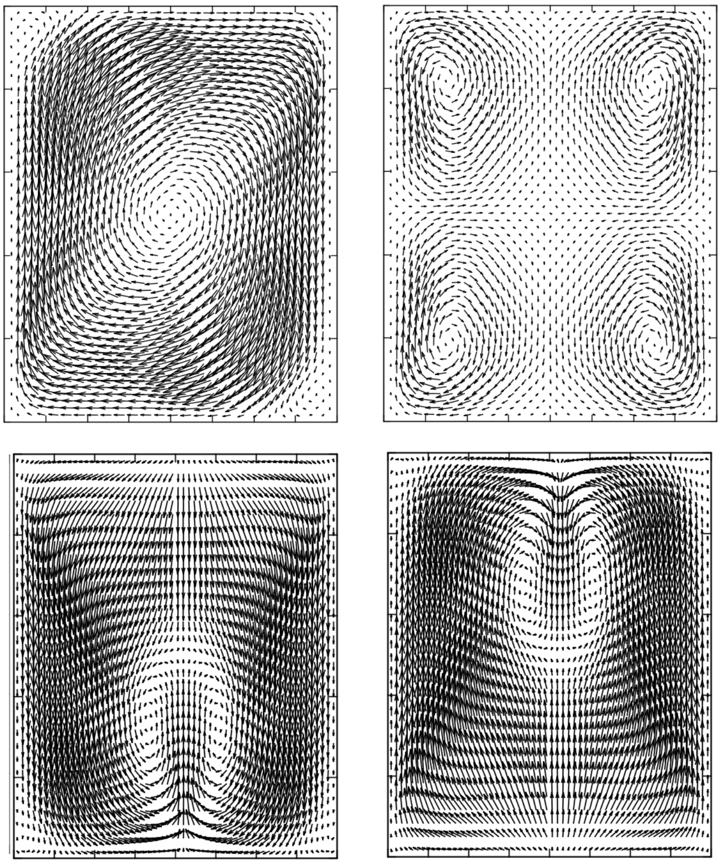

Figure 7.4: Planes AA' and BB'. Top Line: Natural convection without the effect of a magnetic field. Bottom line: Natural convection under the influence of a magnetic field $Ha = 30$. $Ra = 5.5 \times 10^5$

The dynamic properties discussed before are fully consistent with the velocity distribution shown in the figure 7.4. However the vertical symmetry is clearly displayed in the case Ha=30; i.e. flipping the velocity field of the lower left figure around the mid-height horizontal line, gives the lower right distribution.

7.1.2 Time dependent flow

We consider a cylindrical container of aspect ratio 1.25 filled with water $Pr = 6.67$, heating from below and cooled from above, the Rayleigh number is $Ra = 1.5 \times 10^6$, which is a time dependent flow without the effect of a magnetic field.

The structure of the flow in this case has an average behavior like the previous discussed situation an only a few comments will give to emphasize that the application of a magnetic field parallel to the axis of symmetry of the cylinder might transform a time dependent flow in to a steady state motion. This is of great importance in engineering application such the crystal growth processes.

The time dependent features corresponding to the case of the zero magnetic field is illustrated in figure 7.5 where the axial velocity field at point (A/2,π,1/2) is plotted as a function of the time, an initial transient flow is followed by a periodic motion (Black line). When Hartmann number is set to 40, the flow displays a large oscillations for times smaller than 700 followed by a constant velocity (zero amplitude for this particular point, blue line).

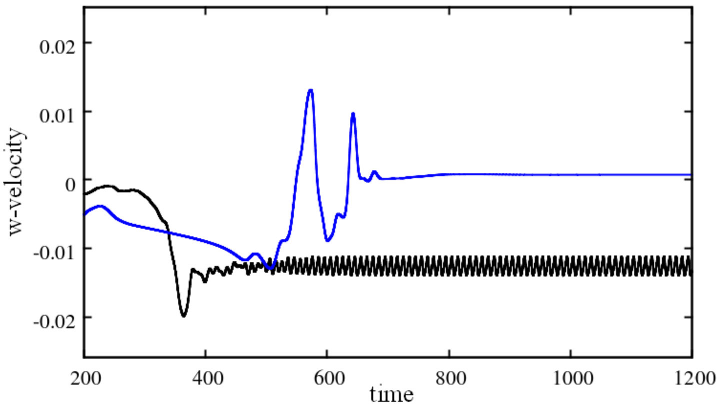

Figure 7.5: Time evolution of the flow with (Ha=40, blue line) and without (Ha=0, black line) the effect of a magnetic field. $Ra = 1.5 \times 10^6$

It is tempting to build a plot to find the critical Hartmann number required to kill the oscillation. However in contrast to the rotation case (see section 6.1.2). It is no possible to do such a calculation for the present conditions, since the system displays multiple solutions for the same Rayleigh and Hartmann numbers based on the initial conditions of the system. If we restrict ourselves to a single convective pattern obtained by zero velocity initial conditions, then a critical Hartmann number can be identified. An example of this calculation is shown in figure 7.6 the amplitude of the oscillation as a function of the Hartmann number.

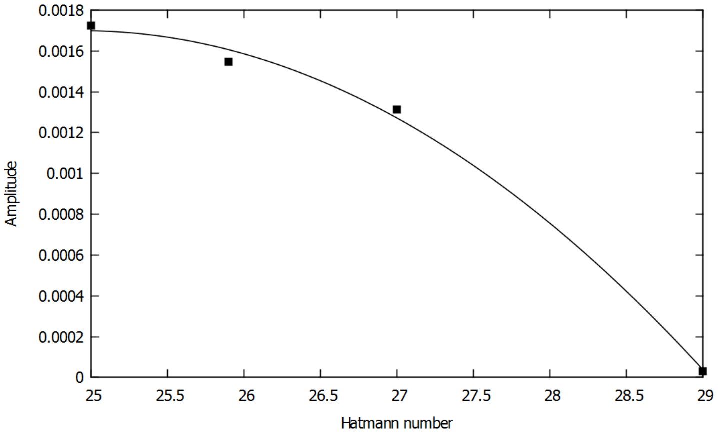

Figure 7.6: Amplitude vs Hartmann. Natural convection $Ra = 1.5 \times 10^6$.

The qualitative behavior indicates a monotonous decreasing function and a quadratic polynomial fit indicates that $Ha = 29.0446$ results in zero amplitude of the oscillation.

The multiplicity generated by the symmetric preserving conditions might be considered. A deep study should be needed, we only explore the efficacy of the numerical tools developed to study natural convection in cylindrical geometries now including the effect of a magnetic field for the case of an electrically conducting fluids.

Conclusions

A numerical techniques to solve the fluid dynamics equations in cylindrical coordinates were presented.

The finite volume method was widely applied in this study due to its simplicity and implementation facilitates but this methodology has issues with the periodicity and low order accuracy.

Spectral methods have proved to be very useful tools with high precision of the solution, ensuring periodicity and no special treatment of origin. Spectral codes to solve two dimensional and three dimensional flows was developed. Spectral method are more complicated to implemented and the numerical calculations are slower than the calculations with the finite volume method.

The difficulties handling discontinuous problems as many operations that characterize spectral methods begin the process that become a hybrid methodology proposal between finite volume and spectral methods. With this method the solutions obtained with finite volume can include the advantages of spectral methods as the guarantee of periodicity which can be obtained with the Fourier method as well as an accuracy increment in the azimuthal direction.

A methodology proposal were presented in chapter IV, it combines finite volume and a spectral methodology, conserving the simplicity of the finite volume code and solving periodicity problems and improving the accuracy with a Fourier spectral method.

The numerical strategies presented were proved for the case of natural convection in a cylindrical container. Those tools was used to solve the natural convection flows of fluid in a cylindrical container, also the effect of rotation or a electromagnetic force was added.

Bibliography

[1] Koschmieder E. L. *Bénard Cells and Taylor Vortices.* Cambridge Monographs on Mechanics, 1993.

[2] Buell J.C. and Catton I. The effect of wall conduction on the stability of a fluid in a right circular cylinder heated from below. *J. Heat Transf.*, 105:255–260, 1983.

[3] M. Lopez Caballero. Conveccion natural en cilindros esbeltos. Master's thesis, Universidad Nacional Autonoma de Mexico, Mexico D. F., Enero 2009.

[4] I.G Currie. *Fundamental Mechanics of Fluids.* McGraw Hill, 1974.

[5] L.D. Landau and E.M Lifshitz. *Fluid Mechanics.* Pergamon Press, 1987.

[6] J. H. Ferziger and M. Peric. *Computational Methods for Fluid Dynamics.* Springer-Verlag, 2002.

[7] T. Dornseifer M. Griebel and T. Neunhoeffer. *Numerical Simulation in Fluid Dynamics: A practical Introduction.* SIAM, 1998.

[8] H.K Versteeg and W. Malalasekera. *An introduction to Computational Fluid Dynamics, The Finite Volume Method.* Prentice Hall, 1995.

[9] S. V. Patankar. *Numerical Heat Transfer and Fluid Flow.* McGraw Hill, 1980.

[10] J. G. M. Eggels, F. Unger, M. H. Weiss, J. Westerweel, R. J. Adrian, R. Friedrich, and F. T. M. Nieuwstadt. Fully developed turbulent pipe flow: a comparison between direct numerical simulation and experiment. *J. Fluid Mech.*, 268:175–210, 1994.

[11] Koji Fukagata and Nobuhide Kasagi. Highly energy-conservative finite difference method for the cylindrical coordinate system. *J. Comput. Phys.*, 181(2):478–498, 2002.

[12] R. Peyret. *Spectral Methods for Incompressible Viscous Flow.* New York: Springer, 2002.

[13] Quarteroni A Canuto C, Hussaini MY and Zhang TA. *Spectral methods in fluid dynamics.* Berlin: Springer, 1988.

[14] Boyd J. *Chebyshev and fourier spectral methods.* New York: Dover, 2001.

[15] I. Mercader, O. Batiste, and A. Alonso. An efficient spectral code for incompressible flows in cylindrical geometries. *Computers & Fluids*, 39(2):215– 224, 2010.

[16] Yuhong Su. Collocation spectral methods in the solution of poisson equation. Master's thesis, The University of British Columbia, Vancouver, Canada, August 1998.

[17] Shengakai Zhao and Matthew J. Yedlin. A new iterative chebyshev spectral method for solving the elliptic equation $\nabla \cdot (\sigma \nabla u) = f$. *J. Comput. Phys.*, 113:215–223, 1994.

[18] Serre E. and Pulicani J.P. A three-dimensional pseudospectral method for rotating flows in a cylinder. *Computers & Fluids*, 30:491–519(29), 2001.

[19] Anthony Randriamampianina, Roland Schiestel, and Michael Wilson. Spatio-temporal behaviour in an enclosed corotating disk pair. *J. Fluid Mech.*, 434:39–64, 2001.

[20] David L. Brown, Ricardo Cortez, and Michael L. Minion. Accurate projection methods for the incompressible navier stokes equations. *J. Comput. Phys.*, 168(2):464–499, 2001.

[21] G.E. Karniadakis and S.J. Sherwin. *Spectral/hp Element Methods for CFD.* New York:Oxford University Press, 2005.

[22] J. M. Lopez, F. Marques, and Jie Shen. An efficient spectral-projection method for the navier-stokes equations in cylindrical geometries: Ii. three-dimensional cases. *J. Comput. Phys.*, 176(2):384 – 401, 2002.

[23] S.V Patankar and D.B Spalding. A calculation procedure for heat, mass and momentum transfer in three-dimensional parabolic flows. *Intnl J. Heat Mass Transfer*, 15(10):1787 – 1806, 1972.

[24] R. Verzicco and P. Orlandi. A finite-difference scheme for three-dimensional incompressible flows in cylindrical coordinates. *J. Comput. Phys.*, 123(2):402–414, 1996.

[25] A. J. Chorin. Numerical solution of the Navier-Stokes equations. *Math. Comp.*, 22:745–762, 1968.

[26] J. P. Van Doormaal and G. D. Raithby. Enhancements of the simple method for predicting incompressible fluid flows. *Numer. Heat Transfer*, 7:147–163, 1984.

[27] S.D. Connell and P. Stow. The pressure correction method. *Computers & Fluids*, 14(1):1–10, 1986.

[28] Ozoe H. Yu, B. and W. Q. Tao. A modified pressure-correction scheme for the simpler method, msimpler. *Numer. Heat Transfer B*, 39:439–449, 2001.

[29] Neumann G. Three-dimensional numerical simulation of buoyancy-driven convection in vertical cylinders heated from below. *J. Fluid Mech*, 214:559–578, 1990.

[30] P. Le Quéré and J. Pecheux. A three-dimensional pseudo-spectral algorithm for the computation of convection in a rotating annulus. In *ICOSAHOM '89: Proceedings of the conference on Spectral and high order methods for partial differential equations*, pages 261–271, 1990.

[31] J. M. Lopez, F. Marques, I. Mercader, and O. Batiste. Onset of convection in a moderate aspect-ratio rotating cylinder: Eckhaus-benjamin-feir instability. *J. Fluid Mech.*, 590:187–208, 2007.

[32] D. Gottlieb and S. Orzag. *Numerical Analysis of Spectral Methods : Theory and Applications*. SIAM, Philadelphia, PA, 1977.

[33] L.S. Tuckerman. Divergence-free velocity fields in nonperiodic geometries. *J. Comput. Phys.*, 80:403–441, 1989.

[34] E. Barbosa and O. Daube. A finite difference method for 3d incompressible flows incylindrical coordinates. *Computers & Fluids*, 34:950–971, 2005.

[35] F. Marques and J. M. Lopez. Precessing vortex breakdown mode in an enclosed cylinder flow. *Phys. Fluids*, 13(6):1679–1682, 2001.

[36] Lappa M. *Thermal convection, Patterns, evolution and stability.* Wiley, 2010.

[37] Duffar T. *Crystal growth processes based on capillarity.* Wiley, 2010.

[38] Chandrasekhar S. *Hydrodynamic and Hydromagnetic Stability.* New York: Dover, 1961.

[39] Charlson G.S. and Sani R. L. Thermoconvective instability in a bounded cylindrical fluid layer. *Int. J. Heat Mass Transf.*, 13:1479–1495, 1970.

[40] Charlson G.S. and Sani R.L. On the thermoconvective instability in a bounded cylindrical fluid layer. *Int. J. Heat Mass Transf.*, 14:2157–2160, 1971.

[41] Olson J.M. and Rosenberger F. Convective instabilities in a closed vertical cylinder heated from below. part 1. monocomponent gases. *J. Fluid Mech.*, 92:609–629, 1979.

[42] Mueller G. Neumann G. and Weber W. Natural convection in vertical bridgman configurations. *J. Crystal Growth*, 70:78–93, 1984.

[43] Crespo del Arco E., Bountoux P., Sani R.L., Hardin G., and Extrémet G.P. Steady and oscillatory convection in vertical cylinders heated from below. numerical simulation of asymmetric flow regimes. *Advances in Space Research*, 8(12):281 – 292, 1988.

[44] S. V. Patankar. *Numerical Heat Transfer and Fluid Flow.* McGraw Hill, 1980.

[45] VanDoormal J.R. and Raithby G.D. Enhancements of the simple method for predicting incompressible fluid flows. *Numer. Heat Transfer.*, 7:147–163, 1984.

[46] Hussain F. Jeong J. On the identification of a vortex. *J. Fluid Mech.*, 285:69–94, 1994.

[47] Aeschliman D.P., Oberkampf W.L., and Blottner F.G. A proposed methodology for computational fluid dynamics code verification, calibration, and validation. *International Congress on Instrumentation in Aerospace Simulation Facilities*, 16:255–260, 1995.

[48] Pedlosky J. *Geophysical fluid dynamics.* Springer-Verlag, 1992. English translation: translated by Nathaniel Bowditch.

[49] Laplace P. S. *Mécanique céleste.* Boston, 1829. English translation: translated by Nathaniel Bowditch.

[50] Coriolis G. G. Sur les équations du mouvement relatif des systemes de corps. *J. de l'Ecole royale polytechnique*, 15(04):144–154, 1835.

[51] Greenspan H. P. *The Theory of Rotating Fluids.* Cambridge University Press. New York, 1968.

[52] J. M. Lopez and F. Marques. Centrifugal effects in rotating convection:nonlinear dynamics. *J. Fluid Mech.*, 628:269–297, 2009.

[53] Ramos E. and Vargas M. The boussinesq approximation in a rotating frame of reference. *Intnl J. NonEquilibrium Thermodynamics*, 30:21–37, 2005.

[54] Vargas M. Ramos E. and Ascanio G. A centrifuge for studies of fluid dynamics phenomena in a rotating frame of references. *Revista Mexicana de fisica*, 48:255–266, 2002.

[55] S. C. Kakarantzas and A. P. Grecos. Direct numerical simulation of a heat removal configuration for fusion blankets. *Energy Conversion and Management*, 48:2775–2783, 2007.

[56] Hof B. and Mullin T. et al. On the onset of oscillatory convection in molten gallium. *J. Fluid Mech.*, 515:391 – 413, 2004.

[57] P. A. Davison. *An Introduction to Magnetohydrodynamics.* Cambridge, 2001.

[58] J. D. Jackson. *Classical Electrodynamics.* John Wiley Sons, 1975.

[59] Smolentsev S. Mahtematical models for magnetohydrodynamic flows in a fusion reactor blanket. *Plasma Dev. Opert.*, 7:231–241, 1999.